UNIVERSIDAD DE INVESTIGACIÓN DE TECNOLOGÍA EXPERIMENTAL YACHAY

Escuela de Ciencias Químicas e Ingeniería

TÍTULO: SPECTROSCOPIC AND REDOX PROPERTIES OF BIOMIMETICS OF COPPER METALLOPROTEINS: A PRACTICAL AND THEORETICAL APPROACH

Trabajo de integración curricular presentado como requisito para la obtención del título de Química

Autor:

Maria Emilia Iglesias Moncayo

Tutor:

Juan Pablo Saucedo, PhD.

Co-tutor:

Thibault Terencio, PhD.

Urcuquí, June 28, 2021

Urcuquí, 24 de junio de 2021

SECRETARÍA GENERAL
(Vicerrectorado Académico/Cancillería)
ESCUELA DE CIENCIAS QUÍMICAS E INGENIERÍA
CARRERA DE QUÍMICA
ACTA DE DEFENSA No. UITEY-CHE-2021-00015-AD

A los 24 días del mes de junio de 2021, a las 14:30 horas, de manera virtual mediante videoconferencia, y ante el Tribunal Calificador, integrado por los docentes:

Presidente Tribunal de Defensa	Dr. CAETANO SOUSA MANUEL , Ph.D.
Miembro No Tutor	Dra. LOPEZ GONZALEZ, FLORALBA AGGENY , Ph.D.
Tutor	Dr. SAUCEDO VAZQUEZ, JUAN PABLO , Ph.D.

El(la) señor(ita) estudiante **IGLESIAS MONCAYO, MARIA EMILIA**, con cédula de identidad No. **0104852157**, de la **ESCUELA DE CIENCIAS QUÍMICAS E INGENIERÍA**, de la Carrera de **QUÍMICA**, aprobada por el Consejo de Educación Superior (CES), mediante Resolución **RPC-SO-39-No.456-2014**, realiza a través de videoconferencia, la sustentación de su trabajo de titulación denominado: **SPECTROSCOPIC AND REDOX PROPERTIES OF BIOMIMETICS OF COPPER METALLOPROTEINS: A PRACTICAL AND THEORETICAL APPROACH**, previa a la obtención del título de **QUÍMICO/A**.

El citado trabajo de titulación, fue debidamente aprobado por el(los) docente(s):

Tutor	Dr. SAUCEDO VAZQUEZ, JUAN PABLO , Ph.D.
Co - Tutor	Dr. TERENCIO THIBAULT , Ph.D.

Y recibió las observaciones de los otros miembros del Tribunal Calificador, las mismas que han sido incorporadas por el(la) estudiante.

Previamente cumplidos los requisitos legales y reglamentarios, el trabajo de titulación fue sustentado por el(la) estudiante y examinado por los miembros del Tribunal Calificador. Escuchada la sustentación del trabajo de titulación a través de videoconferencia, que integró la exposición de el(la) estudiante sobre el contenido de la misma y las preguntas formuladas por los miembros del Tribunal, se califica la sustentación del trabajo de titulación con las siguientes calificaciones:

Tipo	Docente	Calificación
Tutor	Dr. SAUCEDO VAZQUEZ, JUAN PABLO , Ph.D.	10,0
Miembro Tribunal De Defensa	Dra. LOPEZ GONZALEZ, FLORALBA AGGENY , Ph.D.	10,0
Presidente Tribunal De Defensa	Dr. CAETANO SOUSA MANUEL , Ph.D.	10,0

Lo que da un promedio de: **10 (Diez punto Cero)**, sobre 10 (diez), equivalente a: **APROBADO**

Para constancia de lo actuado, firman los miembros del Tribunal Calificador, el/la estudiante y el/la secretario ad-hoc.

Certifico que *en cumplimiento del Decreto Ejecutivo 1017 de 16 de marzo de 2020, la defensa de trabajo de titulación (o examen de grado modalidad teórico práctica) se realizó vía virtual, por lo que las firmas de los miembros del Tribunal de Defensa de Grado, constan en forma digital.*

IGLESIAS MONCAYO, MARIA EMILIA
Estudiante

MANUEL CAETANO SOUSA
Digitally signed by MANUEL CAETANO SOUSA
Date: 2021.06.28 12:33:05 -05'00'

Dr. CAETANO SOUSA MANUEL , Ph.D.
Presidente Tribunal de Defensa

JUAN PABLO SAUCEDO VAZQUEZ

Firmado digitalmente por JUAN PABLO SAUCEDO VAZQUEZ
Fecha: 2021.06.28 19:21:47 -05'00'

Dr. SAUCEDO VAZQUEZ, JUAN PABLO , Ph.D.
Tutor

FLORALBA AGGENY LOPEZ GONZALEZ

Digitally signed by FLORALBA AGGENY LOPEZ GONZALEZ
Date: 2021.06.24 17:12:53 -05'00'

Dra. LOPEZ GONZALEZ, FLORALBA AGGENY , Ph.D.
Miembro No Tutor

CARLA SOFIA YASELGA NARANJO

Digitally signed by CARLA SOFIA YASELGA NARANJO
Date: 2021.06.24 16:46:14 -05'00'

YASELGA NARANJO, CARLA
Secretario Ad-hoc

AUTORÍA

Yo, **MARIA EMILIA IGLESIAS MONCAYO**, con cédula de identidad 0104852157, declaro que las ideas, juicios, valoraciones, interpretaciones, consultas bibliográficas, definiciones y conceptualizaciones expuestas en el presente trabajo; así cómo, los procedimientos y herramientas utilizadas en la investigación, son de absoluta responsabilidad de el/la autora (a) del trabajo de integración curricular, ensayo o artículo científico. Así mismo, me acojo a los reglamentos internos de la Universidad de Investigación de Tecnología Experimental Yachay.

Urcuquí, Abril 2021.

Maria Emilia Iglesias Moncayo

CI: 0104852157

AUTORIZACIÓN DE PUBLICACIÓN

Yo, **MARIA EMILIA IGLESIAS MONCAYO**, con cédula de identidad 0104852157, cedo a la Universidad de Tecnología Experimental Yachay, los derechos de publicación de la presente obra, sin que deba haber un reconocimiento económico por este concepto. Declaro además que el texto del presente trabajo de titulación no podrá ser cedido a ninguna empresa editorial para su publicación u otros fines, sin contar previamente con la autorización escrita de la Universidad.

Asimismo, autorizo a la Universidad que realice la digitalización y publicación de este trabajo de integración curricular, en el repositorio virtual, de conformidad a lo dispuesto en el Art. 144 de la Ley Orgánica de Educación Superior.

Urcuquí, Abril 2021.

MEmelda Moncayo

Maria Emilia Iglesias Moncayo

CI: 0104852157

DEDICATORIA

To my mom Maritza

The world is a better place with you in it

To my best friends Romina, Dalena, Gaby and Anthony.

For being the siblings, I could have just dream of

To my professors

For always believing

To the unavoidable changes in life

For existing

Thank you for never giving up on me

This is for you

Maria Emilia Iglesias Moncayo

ACKNOWLEDGMENT

- To my mom, for being the center of all the things and for all her sacrifice. Thank you for loving me every step of the way and for believing in me even in the darkest and hardest moments. Your support has made me the person I am today and will continue to guide me along the road ahead. Thank you very much for always believe in the impossible and your huge patience. It will always be you and me against the world. I love you mom every day.
- To my dearest friends Romina, Dalena, Kimberly, Kathy, Gaby, Sisa, Micky, Alex, David and Jho for their unconditional support through university. University is more than study, thank you for all the time we spent together, laughing, crying, cooking, gossiping and in general just living. That our friendship stays strong and overcome distance, time, and any future unforeseeable problem. May all your futures be as bright an amazing as you are.
- To all my professors, thank you for guiding us during our time at university. Thank you for all the effort and love put in every class and for always being open to talk about life.
- I am especially thankful with Professor Juan Pablo Saucedo; he has been present since way back in leveling course until the very last day of my career. He has been not only been an excellent professor and mentor but more like a father. Thank you very much for all the things you have taught me, for your patience, guidance, for saying the hard truth whenever required, and for all your advice. Keep being that person for many more students.
- I am extremely grateful to Professor Tibo, he is without any doubt one of the kindest persons that I have met in my life. This thesis truly would not have been possible without his help. I am extremely thankful for all the time you invested in this project. Thank you for never making me feel small whenever I did not understand something. I am grateful for your advice in any technical or personal problem I consulted with you. Your unique way of being deeply inspires me at a personal and academic level. I hope I become a charismatic and wise professor like you at some point in my future.
- Finally, to Professor Hortensia Rodriguez, you have been an inspiration as a scientist as well as a woman throughout my career. Thank you for being in the laboratory during the experimental part of this project, and for supporting my internship in 2019.
- For the access to the Imbabura Cluster to the PhD. Duncan Mowbray

Maria Emilia Iglesias Moncayo

Resumen

De forma natural, en el metabolismo humano se forman especies reactivas de oxígeno como el anión peróxido y el anión radical superóxido ($O_2^{\bullet -}$), siendo estas de gran interés ya que el desequilibrio de los niveles de especies reactivas de oxígeno se ha asociado a múltiples enfermedades. Uno de los mecanismos de defensa del organismo para contrarrestar el aumento excesivo de especies reactivas de oxígeno son las metaloproteínas como la superóxido dismutasa. Esta enzima es capaz de catalizar la dismutación del anión superóxido a peróxido de hidrógeno y oxígeno, sin embargo, a pesar de su potencial biológico el uso directo de la superóxido dismutasa nativa en terapia se ha visto limitado debido a múltiples inconvenientes. Por ello, se ha realizado un importante esfuerzo científico para desarrollar biomiméticos de bajo peso molecular basados en compuestos de coordinación.

Por esta razón, en este trabajo se pretende sintetizar y caracterizar nuevos complejos de cobre y manganeso. La caracterización se realizará tanto de forma experimental como computacionalmente para entender su reactividad como un primer paso para obtener nuevos complejos biomiméticos de la superóxido dismutasa. Como parte del trabajo experimental, presentaremos resultados de la síntesis y purificación de los ligantes y los correspondientes complejos de cobre y manganeso. Entre los ligantes, se evaluó el efecto de pequeñas diferencias estructurales en sus propiedades fisicoquímicas. En este sentido, cuatro de los ligantes comparten la misma estructura general, excepto por los sustituyentes en la posición *para* (-H, -OH, -Cl, -CH_3). Un aspecto importante que se evaluó en la síntesis de los complejos fue la influencia de la estequiometría de las reacciones, así, para el mismo ligante, se utilizaron diferentes proporciones de la relación metal:ligante como 1:1 y 1:2. La segunda parte de este proyecto se centró en la caracterización fisicoquímica de los compuestos obtenidos mediante espectroscopía infrarroja con transformada de Fourier, espectroscopía UV-Vis (sólido y líquido) y susceptibilidad magnética. En la siguiente etapa del proyecto, los resultados experimentales obtenidos se compararon con simulaciones computacionales mediante teoría del funcional de la densidad y teoría del funcional de la densidad tiempo-dependiente. Finalmente, las geometrías optimizadas de los ligantes y complejos se utilizaron para calcular múltiples parámetros que permitieron determinar el mejor candidato como mimético de la superóxido dismutasa.

Palabras claves: Complejos de cobre, complejos de manganeso, DFT, SOD, biomiméticos.

Abstract

Naturally, reactive oxygen species such as peroxide anion and superoxide radical anion ($O_2^{\bullet -}$) are formed in human metabolism, these being of great interest since the imbalance of reactive oxygen species' levels has been associated with multiple diseases. One of the body's defense mechanisms to mitigate the excessive increase in reactive oxygen species are metalloproteins such as superoxide dismutase. This enzyme is capable of catalyzing the dismutation of the superoxide anion to hydrogen peroxide and oxygen, however, despite its biological potential against reactive oxygen species, the direct use of native superoxide dismutase in therapy has been limited due to multiple drawbacks. Therefore, an important scientific effort has been made to develop low molecular weight biomimetics based on coordination compounds.

For this reason, this work aims to synthesize and characterize new complexes of copper and manganese. The characterization will be carried out both experimentally and computationally to understand its reactivity as a first step to obtain new biomimetic complexes of superoxide dismutase. As part of the experimental work, we will present results of the synthesis and purification of the ligands and the corresponding complexes of copper and manganese. Among the ligands, the effect of small structural differences in their physicochemical properties was evaluated. In this sense, four of the ligands share the same general structure, except for the substituents at the *para* position (-H, -OH, -Cl, -CH_3). An important aspect that was evaluated in the synthesis of the complexes was the influence of the stoichiometry of the reactions, thus, for the same ligand, different proportions of the metal:ligand ratio were used, for example 1: 1 and 1: 2. The second part of this project focused on the physicochemical characterization of the compounds obtained by Fourier-transform infrared spectroscopy, UV-Vis spectroscopy (solid and liquid) and magnetic susceptibility. In the next stage of the project, the experimental results obtained were compared with computational simulations using density functional theory and time dependent functional theory. Finally, the optimized geometries of the ligands and complexes were used to calculate multiple parameters that made it possible to determine the best candidate as a superoxide dismutase mimetic.

Keywords: Copper Complexes, Manganese complexes, DFT, SOD, biomimetic.

CONTENT

Chapter 1. Background 1
1.1 Copper 1
1.1.1 General considerations 1
1.1.2 Coordination chemistry of copper 1
1.1.3 Copper in biology 1
1.1.4 Copper in proteins 2
1.2 Manganese 3
1.2.1 General manganese chemistry 3
1.2.2 Coordination chemistry of manganese 3
1.2.3 Manganese in biology 4
1.3 Reactive oxygen species 5
1.4 Superoxide dismutase 6
1.4.1 CuZn superoxide dismutase (SOD1) 7
1.4.2 Mn superoxide dismutase 8
1.5 Uses of natural SOD 9
1.5.1 Disadvantages of using native SOD 9
1.6 SOD biomimetics 9
1.6.1 Measurements of SOD activity 10
1.6.2 Examples of SOD mimetics 11
1.7 Computational principles 15
1.7.1 Important programs for computational analysis 15
1.7.2 Density functional theory 16
1.7.3 Time dependent density functional theory 16

1.7.4 Computational approach 17
1.7.5 Computational prediction of biological activity 18
Chapter 2. Problem statement 20
2.1 General problem statement 20
2.2 Objectives 20
2.2.1 General objectives 20
2.2.2 Specific objectives 21
Chapter 3. Methodology 21
3.1 Laboratory section 22
3.1.1 Reagents and equipment 22
3.1.2 Synthesis of ligands and complexes 23
3.2 Computational approach 26
3.2.1 Geometry optimization 26
3.2.2 Infrared spectroscopy calculation 26
3.2.3 Time dependent density functional theory calculations 27
Chapter 4. Experimental and theoretical results and discussion 28
4.1 L1 and its complexes 28
4.1.1 Analysis for L1 28
4.1.2 IR of L1 31
4.1.3 UV-Vis of L1 32
4.1.4 Biological activity of L1 35
4.2 Complexes with L1 37
4.2.1 General description of the complexes 37
4.2.2 Geometry optimization of complexes with L1 38
4.2.3 IR analysis for complexes with L1 40

4.2.4 UV-Vis for copper complexes with L1 43
4.2.5 Diffuse reflectance for complexes with L1 46
4.2.6 Biological Activity of complexes with L1 47
4.3 Set of ligands derivate from vanillin with aniline and its derivatives (L2X) 52
4.3.1 Geometry optimization L2X 52
4.3.2 IR results for L2X 54
4.4 UV-Vis for set of Ligands L2X 56
4.4.1 Biological analysis of L2X 58
4.5 Complexes with ligands L2X 61
4.5.1 General characteristics of complexes of Cu2X 61
4.5.2 General characteristic of complexes of Mn2X 61
4.5.3 Geometry optimization 62
4.5.4 FTIR analysis for complexes Cu2X and Mn2X 64
4.5.5 UV-Vis Complexes with ligands L2X 67
4.5.6 Diffuse reflectance of complexes with ligands L2X 72
4.5.7 Biological activity of complexes with L2X 74
4.6 Final discussion of SOD activity for complexes 81
4.6.1 Final discussion of SOD activity for copper complexes 81
4.6.2 Final discussion SOD activity for manganese complexes 81
Chapter 5. Conclusions 82
Chapter 6. Recommendations and future work 84
Chapter 7. References 85
Chapter 8. Annexes 96

LIST OF FIGURES

Figure 1 Common coordination geometries for Cu^{2+} and Cu^{1+} 1
Figure 2 Copper sites from left to right: type I, type II, type III and Cu_A adapted from Solomon et al. 2014..... 3
Figure 3 a) Common geometry for Mn^{2+} and Cristal field for d^5 octahedral high spin. b) Common geometries for Mn^{3+} 3
Figure 4 Diverse redox reaction that generate ROS adapted from Bowler, Barnes, and Crapo (2004)..... 5
Figure 5 ROS production and effect on biomolecules, taken from Schieber and Chandel (2014). 6
Figure 6 General mechanism of SOD metalloproteins adapted from Abreu and Cabelli (2010) . . 7
Figure 7 General simplify mechanism for CuZn SOD addapted from Quist et al. 7
Figure 8 a) Active site SOD1 b) General structure SOD 1 (adapted from PDB 1HI5) c) Catalytic Mechanism of copper SOD addapted from Quist et al 8
Figure 9 a) Active site MnSOD without solvent (water) b) General structure (Adapted from PDB 5VF9) c) Mechanism MnSOD adapted from Azadmanesh et al. 8
Figure 10 Best complexes from the papers of Puchoňová et al. , Savithri et al. and Patel et al. .. 11
Figure 11 Proposed complexes by Siqueira et al. in 2019..... 12
Figure 12 complexes proposed by González-Baró et al. 2010, Tabassum et al. 2013 and Tabassum et al. 2015..... 13
Figure 13 Complexes proposed Afsan et al. 2019 and Dong et al. 2020..... 13
Figure 14 Discussed SOD mimetic with salen ligands Rouco et al. 14
Figure 15 Joseph and Rani in 2014, Pereira et al. in 2018, Sangeeta 2018 and Mohan et al. 2018 15
Figure 16 General Methodology carried out during the research project. 21
Figure 17 Experimental set up for the synthesis of ligands and complexes 24
Figure 18 Input for Geometry optimization..... 26
Figure 19 Input for IR calculation using ORCA..... 27
Figure 20 Input for TDDFT calculations..... 27
Figure 21 Reaction scheme for Ligand 1..... 29

Figure 22 Conformers analyzed for the geometry optimization of L1 29
Figure 23 Conformers of L1: a) L12A b) L12B c) L14A d) L14B e) L11A f) L11B g) L13A h) L13B 30
Figure 24 IR for L1, red for simulation and black for experimental result 32
Figure 25 UV-Vis results for L1 33
Figure 26 Geometry changes upon reduction of L1 35
Figure 27 Orbitals involve in the reduction of L1 36
Figure 28 Obtained Complex C1A 37
Figure 29 Complex C1B 37
Figure 30 Initial conformers analyzed to determine geometry of Cu1A a) CL1N1 b) CL1O1 c) CL1N2 d) CL1O2 e) CL1N3 f) CL1O3 g) CL1N4 h) CL1O4 38
Figure 31 Conformers of Cu1A, from left to right: Cu1A1, Cu1A2 and Cu1A3. 39
Figure 32 Different tested geometries for complex a) Cu1B1w b) Cu1B1 c) Cu1B2w d) Cu1B2 e) Cu1BCu1B3w f) Cu1B3 40
Figure 33 IR for Cu1A in red DFT simulation and in black experimental result. 41
Figure 34 Experimental IR result for Cu1B 42
Figure 35 UV-Vis measurement for Cu1A a) whole spectrum b) zoom in the d-d transfer area. 43
Figure 36 UV-Vis results for complex Cu1B left side complete spectrum and right zoom for d-d transitions of lower energy 45
Figure 37 Diffuse Reflectance for Cu1A 46
Figure 38 Diffuse Reflectance for Cu1B 47
Figure 39 Geometry changes upon redox process in Cu1A 48
Figure 40 Orbitals involve in the reduction of Cu1A 49
Figure 41 Geometry changes in reduction of Cu1B 50
Figure 42 Orbitals involve in the reduction of Cu1B 52
Figure 43 Reaction scheme for set of Ligand 2 and experimental pictures of the L2X 52
Figure 44 Final geometry optimization for a) L21 b) L21-H c) L23 d) L23-H e) L22 f) L22-H g) L24 and h) L24-H 53
Figure 45 FTIR results for L21. a) Theoretical simulations for protonated and non-protonated ligand b) Experimental result. 54
Figure 46 Different TDDFT calculations for L22 from left to right: methods a, b and c. 56

Figure 47 Geometry changes upon redox cycle from L21 to $L21^{-}$. 59
Figure 48 Orbitals involve in redox process from L21 to $L21^{-}$. 60
Figure 49 Copper complexes with L2X from left to right: Cu21, Cu24 and Cu23. 61
Figure 50 Manganese complexes from left to right Mn21, Mn23 and Mn24. 62
Figure 51 Optimized structure Cu21, C23 and C24 62
Figure 52 Optimized geometries for Mn2X: a) Mn21 b) Mn22 c) Mn23 and d) Mn24 63
Figure 53 FTIR results for Cu23, red for simulation and black experimental result. 64
Figure 54 IR for Mn22, red for simulation and black for laboratory results 66
Figure 55 Electronic structure of Cu2X complexes 68
Figure 56 Result of the UV-Vis for Cu21. 69
Figure 57 Electronic configuration for Mn2X complexes 69
Figure 58 UV-Vis results for Mn24 71
Figure 59 Comparison between L24 and Mn24 71
Figure 60 Diffuse reflectance: a) Cu24 b) Cu23 and c) C421 72
Figure 61 Diffuse reflectance Mn21, Mn23, Mn24 and Mn22 73
Figure 62 Geometry changes upon redox of Cu21 74
Figure 63 Geometry changes upon redox process of Mn21 to $Mn21^{+}$ 75
Figure 64 Resonance of L22 ligand 77
Figure 65 Orbitals involve redox process Cu21 78
Figure 66 Molecular Orbitals changes in redox process in Mn21 80
Figure 67 Molecular Orbitals changes in redox process in Mn23 80
Figure 68 IR result for ligands L2X: a) L22 b)L23 c)L24 96
Figure 69 UV-Vis L23 and UV-Vis L24 97
Figure 70 UV-Vis for Cu24 98
Figure 71 UV-Vis results for Cu23 98
Figure 72 UV-Vis for Mn21 99
Figure 73 UV-Vis for Mn23 99
Figure 74 IR for Cu24 (red simulation, black experimental) 100
Figure 75 IR for Cu21 (red simulation, black experimental) 101
Figure 76 IR result for: a) Mn24 and b) Mn23 101
Figure 77 UV-Vis Cu24 101

LIST OF TABLES

Table 1 Reagents used for the synthesis of compounds 22
Table 2 Energy of the conformers for L1 31
Table 3 Summary results for FTIR of L1 31
Table 4 UV-Vis data for L1 34
Table 5 Electron Affinity for L1 35
Table 6 Reactivity parameters for L1 36
Table 7 Energy of conformers of complex Cu1A 38
Table 8 Energy of conformers for CuB1 40
Table 9 IR results for Cu1A 41
Table 10 UV-Vis analysis for Cu1A 44
Table 11 UV-Vis data for Cu1B 44
Table 12 Electronic Affinity for complex Cu1A 48
Table 13 Reactivity parameters for Cu1A 49
Table 14 Electron affinity for Cu1B 50
Table 15 Reactivity parameters for Cu1B 51
Table 16 IR results for L2X. The theoretical values were taken from the non-protonated L2X calculation 56
Table 17 UV-Vis experimental and theoretical results for L22 58
Table 18 Electron affinity for set of ligands 2 60
Table 19 Reactivity parameters for L2X 60
Table 20 Energy for complexes with ligands 2 with copper 63
Table 21 FTIR summarized results for complexes with Cu and Mn 65
Table 22 IR results for Mn2X complexes 67
Table 23 Summary results UV-Vis complexes for C21 68
Table 24 Experimental and simulation UV-Vis results for Mn24 70
Table 25 Diffuse Reflectance for Cu2X complexes 72
Table 26 Diffuse reflectance of complexes Mn2X 73

Table 27 Electronic affinity for Cu2X 76
Table 28 Electronic affinity for Mn2X 77
Table 29 Reactivity parameters for Cu2X 78
Table 30 Reactivity parameters for Mn2X 79
Table 30 UV-Vis results for L2X 97
Table 32 UV-Vis results for Mn2X complexes 100

Chapter 1. Background

1.1 Copper

1.1.1 General considerations

Copper is a transition metal of group IB with atomic number 29 present in four main oxidation states 1^+, 2^+,3^+, 4^+ the first two being the most common. Copper has broad and diverse chemical properties since it can form multiple compounds such as hydride, halides, hydroxides, oxides, sulfides, selenides, sulfates, nitrates, phosphates among many others[1].

1.1.2 Coordination chemistry of copper

Many Cu^{2+} complexes have been studied over the years, being its versatility in geometry an outstanding feature. Copper usually adopts octahedral geometry with distortion in the axial positions, moreover, Jahn-Teller effect is usually observed in octahedral d^9 complexes[2]. Other standard geometries for copper complexes are shown in the Figure 1[3]. In general, Cu^{2+} is defined as a borderline Lewis acid that interacts strongly with nitrogen and oxygen[2]. On the other hand, Cu^{1+} is usually observed in tetrahedral geometry[1] coordinating with phosphorus and sulfur[4].

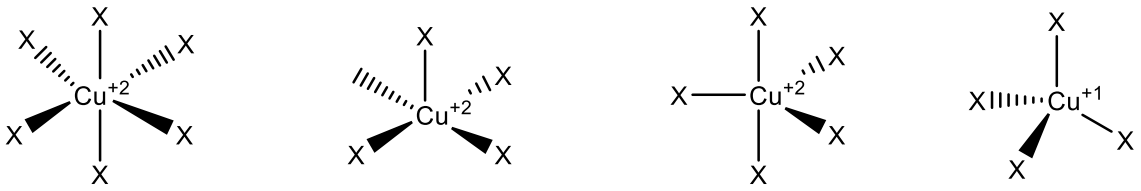

Figure 1 Common coordination geometries for Cu^{2+} and Cu^{1+}.

The redox potential of the metallic center would be tune depending on the nature of the ligands and the geometry around the metal center. The reduction of Cu^{2+} to Cu^{1+} would be preferred when the coordination environment of the complex in the oxidized state is similar or adapts without major changes to a coordination mode preferred by the reduced state. Furthermore, regarding the ligands, the easiness for redox processes follow these coordination modes 2N2S>2N2O>4N[5].

1.1.3 Copper in biology

In the past, the ancient atmosphere had a more reducing character favoring Fe^{2+} and Mn^{2+} rather than Cu^{2+} in biological systems. Nevertheless, the chemistry of the atmosphere drastically changed when oxygen became part of it, which favor its availability for biological systems[6]. Since then,

copper is an essential trace element for living organism present as cofactor in multiple proteins that are usually involved in redox process[7]. Common biological ligands for copper are oxygens from carboxylates, nitrogen of imidazole and thiolate of cysteine or methionine[8]. On the other hand, copper has a dual behavior in nature as it also takes part in Fenton reactions that produce free radicals that provoke oxidative damage to the cell. As wise as nature is, organisms have evolved to have numerous mechanism for the correct homeostasis with copper, this topic will be further discussed in following sections[6].

Now, regarding humans, an adult requires about 2 mg of copper per day and possess in his/her body ~100-150 mg[9]. Copper is initially absorbed in the intestine and then transported to the liver. Next, it moves around the organism through transport/storage proteins and metallochaperones until it is correctly delivered to proteins that require/use it for functioning[6,10]. These processes are essential and highly monitor to contribute in the prevention of copper toxicity because many diseases have been associated with copper homeostasis alteration such as aceruloplasminemia, Wilson's disease, Menkes disease, Alzheimer's disease among others[11].

1.1.4 Copper in proteins

In general, copper proteins divide in two main groups, in the first copper is a cofactor and the second groups are joined copper transport proteins, the first category being the focus of this section. The common coordination numbers in this proteins are four and five, this relatively high coordination number prevents the loss of copper during biological processes[12]. Copper metalloproteins are classified depending on copper structural features in its active site. The classic copper sites are the known blue/type I, type II and the binuclear type III among others[13].

Type I copper proteins are involved in electron transfer processes (plastocyanin in photosynthesis), its characteristic spectroscopic feature is a strong absorption around 600 nm in ultraviolet-visible (UV-Vis) spectroscopy. In the active site, copper possess a special geometry called pseudo-tetrahedral that allows rapid electron transfer[14,15]. The type II copper site can be found in nitrite reductase, this geometry is characteristic for having one copper in square planar geometry or in other cases in relatively distorted tetrahedral geometry[16], it presents a weak absorption at about 700 nm in UV-Vis and electron paramagnetic resonance (EPR) signal with an hyperfine splitting[15]. In the binuclear type III center, each copper is coordinated with three histidines. This center does not possess EPR signal due to an antiferromagnetic coupling between the copper atoms[15] but

possess a strong absorption at 330 nm in UV-Vis[17]. Some samples of proteins containing this site are related to oxygen chemistry such as hemocyanin or tyrosinase[18].

Some proteins require more than one copper type site to perform its catalytic activity. For example, nitrite reductase possess type I and II sites[19], meanwhile, the reduction of dioxygen to water is catalyzed by multicopper oxidases that uses type I, II and III sites[20]. Other common encounter site is the binuclear Cu_A one that has delocalized mixed valence[21]. This type of site can be found in copper containing nitrous oxide reductase , Cu_A site accepts an electron and transfers it to the catalytic site[22]. The geometries of the copper sites are shown in Figure 2 [23].

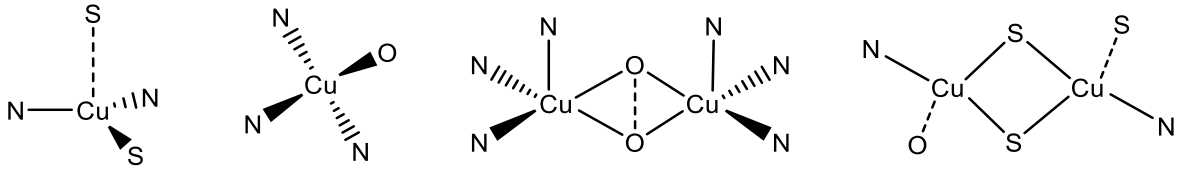

Figure 2 Copper sites from left to right: type I, type II, type III and Cu_A adapted from Solomon et al. 2014 [23]

1.2 Manganese

1.2.1 General manganese chemistry

Manganese is a transition metal found in the group VIIIB. Usually, it can be found in a wide range of oxidation state as 2+,3+,4+,6+, 7+ usually the former found in aqueous solutions. Manganese is used in diverse industries, for example in the steel industry for making alloys. It possess diverse chemistry forming compounds such as oxides, carbonates, silicates, among many others [24,25].

1.2.2 Coordination chemistry of manganese

Manganese is mainly found as Mn^{2+}, a $3d^5$ hard acid, that has a half full configuration in high spin lacking ligand field stabilization energy[26].

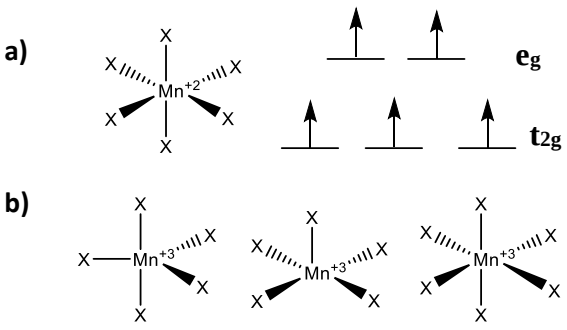

Figure 3 a) Common geometry for Mn^{2+} and Cristal field for d^5 octahedral high spin. b) Common geometries for Mn^{3+}

Mn^{2+} stabilizes a variety of geometries depending upon ligand nature, commonly six as shown in Figure 3 but also higher numbers can be encounter due to its relatively big radii[27]. Octahedral compounds of high spin do not follow the rules of UV-Vis having no allow d-d transitions, therefore, pale colors [28]. Nevertheless, there are multiple mechanism that allow electronic d-d transition despite UV-Vis rules. However, these transitions are of low intensity. To begin with, the spin selection rule is relaxed through spin-orbit coupling. On the other hand, the Laporte rule can vanish upon vibrations, vibronic coupling. For example, in octahedral complexes, some vibration can provoke loss of symmetry allowing a transition[29]. In the case that peaks are observed, most likely the reason is the relaxation of a spin forbidden transition $^4T_1 \rightarrow {}^6A_1$ [30].

Mn^{3+} is consider as a strong oxidant[31] that possess an interesting coordination chemistry, capable of forming polynuclear complexes with oxygen bridges, as well as mononuclear complexes with ligands and Schiff bases. The general coordination number is either five or six as shown in Figure 3. These complexes tend to present Jahn-Teller distortion and are much more colorful since their transitions are allowed by spin selection rule[28].

1.2.3 Manganese in biology

Throughout the history of the earth, manganese has played an essential role in biology as it can change between multiple oxidation states, which allows it to perform hard tasks as multiple electron transfer reactions to reduce water to oxygen[32]. Interestingly, one important area of study is manganese's toxicity due to overexposure in some groups as miners or steel makers which has catastrophic consequences[33].

Mn^{2+} in biological systems tends to coordinate with aspartate, glutamate, tyrosinase and in some cases histidine[34], under given circumstance, it is replaced by other metals that fulfill similar characteristics (manganese is lost from the complex)[35]. Manganese is found in multiple enzymes with diverse roles such as regulation of oxidative stress, functioning of mitochondria, autophagy, and others. The levels of manganese must be precisely controlled because changes affect cognition, antioxidant capacity and metabolic pathway[36]. Moreover, manganese has shown to be important for oxygen metabolism. For example, catalase that has two manganese in its active site, helping to protect the body from toxic hydrogen peroxide converting it into oxygen and water [37].

1.3 Reactive oxygen species

Reactive oxygen species (ROS) are radical and non-radical chemical species derivate from oxygen, some of the reactions that produce ROS can be seen in Figure 4 [38], some examples of the radical species are superoxide anion $O_2^{\bullet-}$, hydroperoxyl radical $HO_2^{\bullet}$, hydroxyl radical $^{\bullet}OH$ and nonradical species as hydrogen peroxide[39]. ROS have short half-life due to theirs unpaired electrons which make them highly reactive[40], and they can be generated in the cell by diverse route such as enzymatic or metabolic (in aerobic conditions)[41]. Interestingly, 1-2% of oxygen is converted to superoxide anion mainly in the electron transport chain. Moreover, peroxide is relatively stable when no metal is present, but in the presence of a metal, superoxide and peroxide can form hydroxyl radical[42]. Some of the usual reactions that form ROS are shown in Figure 4 .

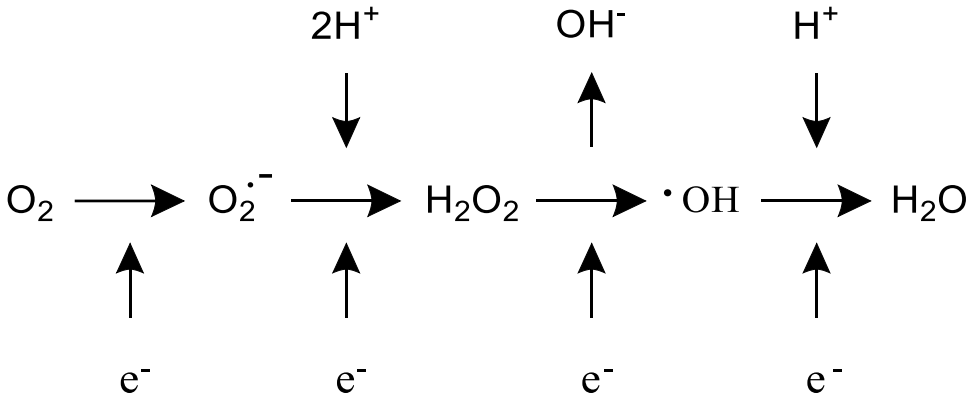

Figure 4 Diverse redox reaction that generate ROS adapted from Bowler, Barnes, and Crapo (2004) [38].

ROS play multiple roles in homeostasis and signaling in the cell as its levels can rise during diverse stress processes. Oxidative stress is produced due to a disrupted balance between production and removal of ROS[42]. Upon evolution, cells have developed diverse mechanism to maintain an equilibrium between ROS generation and defense responses (enzymatic and non-enzymatic)[43]. Some non-enzymatic regulators are vitamin A/C and flavonoids[40], and some enzymatic responses are superoxide dismutase, catalase, ascorbate peroxidase, among others[44]. A rise in ROS causes damage in proteins, nucleic acids, and other biomolecules, and it has been associated with diverse diseases such as cancer, neurodegenerative disease, and diabetes not only due to molecular damage but for its signaling role[45]. For example, in cancer cells, ROS play an interesting role as signaling agents for processes such as abnormal growth or metastasis[40].

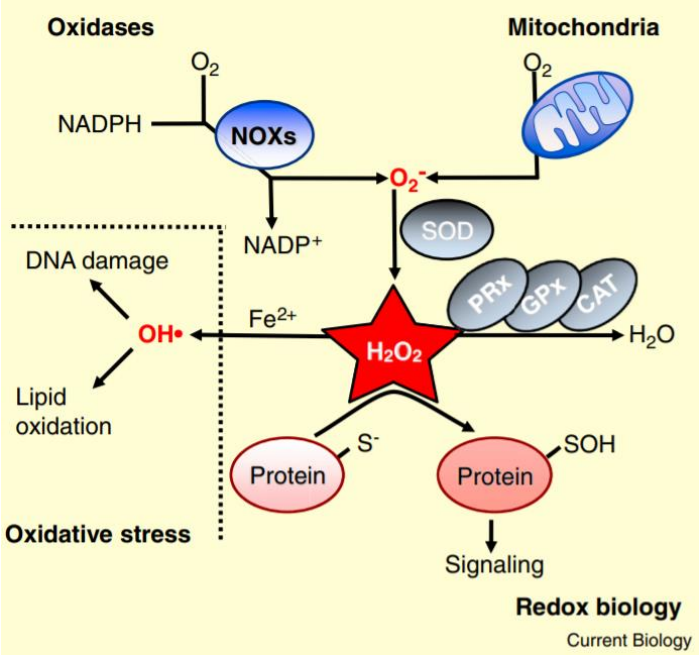

Figure 5 ROS production and effect on biomolecules, taken from Schieber and Chandel (2014) [46].

Some of the signaling processes in which ROS are involved are growth factor, immune responses, differentiation, among others. An interesting feature during signaling process is that despite being very reactive, ROS tends to be very specific to the given target compounds during signaling processes[47]. The most important ROS for signaling are peroxide and superoxide[48]. For example, peroxide is used for signaling because it can easily move through the membrane, it has shown to be involved in epigenetic processes and in autophagy[49]. A general diagram that shows the points discussed through this section can be observed in Figure 5 [46].

1.4 Superoxide dismutase

Superoxide dismutase (SOD) metalloproteins are a family of enzymes present in prokaryotic and eukaryotic organisms, useful for preventing the rise of oxidative stress which is related to diverse diseases as well as aging[50]. The catalytic function of SOD is the dismutation of superoxide free radical anions ($O_2^{\bullet -}$) to oxygen and hydrogen peroxide catalyzed by transition metals[51,52] as observed in Figure 6[53]. SOD produces peroxide during its mechanism, so it must work along with other enzymes such as H_2O_2 consumers (catalase and glutathione peroxidase) to further transform peroxide. This conjoint effort is important because otherwise it would end up involving in reactions with metals to produce hydroxyl radical[50].

$$2O_2^{\cdot -} + 2H^+ \rightarrow O_2 + H_2O_2$$

$$M^{(n+1)} + O_2^{\cdot -} \rightarrow M^{n+} + O_2$$

$$M^{(n+)} + O_2^{\cdot -} + 2H^+ \rightarrow M^{n+1} + H_2O_2$$

Figure 6 General mechanism of SOD metalloproteins adapted from Abreu and Cabelli (2010) .

There are in general three types of SOD, the first one is the cytosolic SOD1 (CuZn) which is a dimer present in all mammals. The second is SOD2 with manganese as a cofactor and found in the mitochondria as a tetramer, and finally the extracellular SOD3 (Cu,Zn) in tetrameric form[54]. Meanwhile, other isoforms may be found in bacteria and plant such as iron containing one[55]. Also, nickel as a cofactor of SOD has been discussed. However, this type of metalloprotein has not been as deeply studied as the other kinds of SOD previously discussed. SOD1 tends to be the most abundant one and works at diffusion-controlled rates. It is very intriguing that despite their differences in the type of cofactors and unrelated structure, they fulfill the same catalytic activity which shows the natural strong necessity for protection against ROS [53,56].

1.4.1 CuZn superoxide dismutase (SOD1)

SOD1 was the first SOD ever identify[57], it is a highly conserved homodimer being one of the most stable known proteins. As its name states, there are two metal ions per monomer, the copper ion fulfills a catalytic purpose and zinc a structural one[51]. General scheme of reaction of CuZn SOD is presented in Figure 7, a more detailed reaction scheme, the active site and the protein structure is shown in Figure 8 .

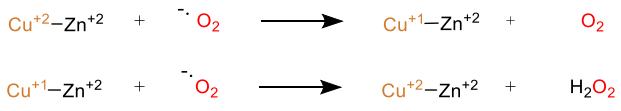

Figure 7 General simplify mechanism for CuZn SOD addapted from Quist et al. [58]

Regarding geometry, zinc is in an almost tetrahedral geometry coordinated by an aspartate and three histidine, one of them serves as a bridge ligand with the copper ion[57]. During the redox process, when copper is reduced, its geometry changes to almost trigonal planar which generates instability overcame by the protonation of the bridging Histidine which is important for the subsequent step of reduction of $O_2^{\cdot -}$ since these protons would be used for the formation of hydrogen peroxide[57,59,60].

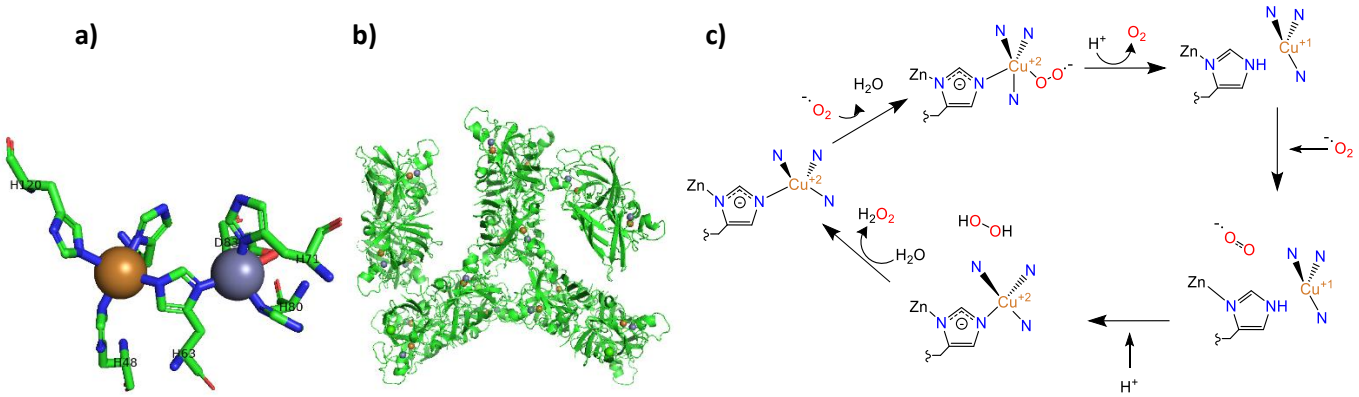

Figure 8 a) Active site SOD1 b) General structure SOD 1 (adapted from PDB 1HI5) c) Catalytic Mechanism of copper SOD addapted from Quist et al [58]

1.4.2 Mn superoxide dismutase

Similarly to CuZn SOD, MnSOD metalloprotein participates in the disproportionation of superoxide by shifting in cycles between Mn^{2+} and Mn^{3+} as observed in Figure 9. Regarding its electrochemistry, it shows a midpoint potential for human MnSOD at +0.39 V[61]. MnSOD is very important to control superoxide anion that is normally produced in the mitochondrial matrix due to metabolism of ATP production[62]. Some residues near the active sites, in the outer sphere, help to guide and carry the anion to the catalytic center due to their positively charge that attracts negative charged anion[63].

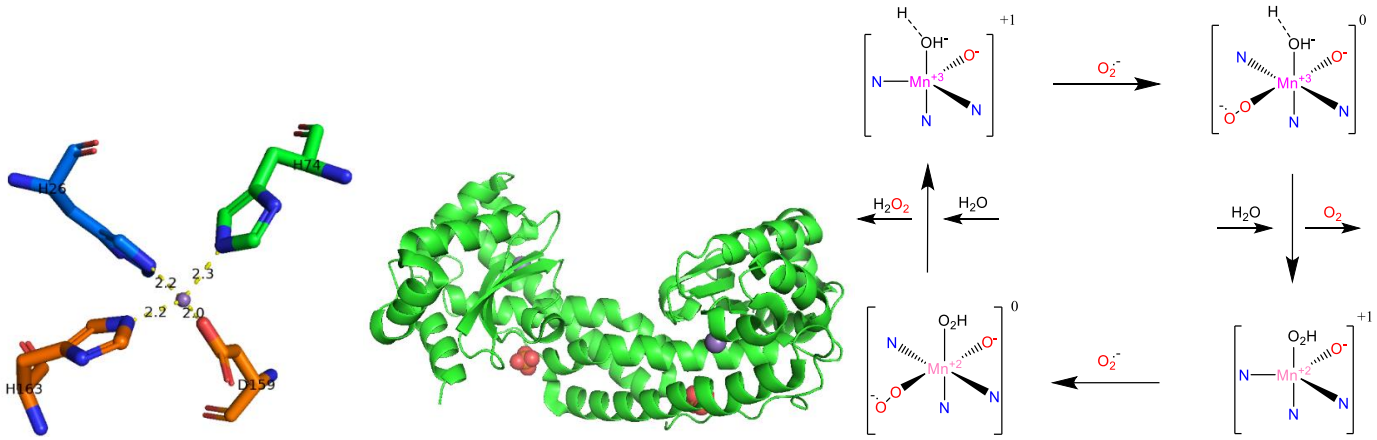

Figure 9 a) Active site MnSOD without solvent (water) b) General structure (Adapted from PDB 5VF9) c) Mechanism MnSOD adapted from Azadmanesh et al. [63]

1.5 Uses of natural SOD

Diverse studies regarding the use of SOD have been performed through the years and continue until now showing that SOD has a wide range of applications. In the review by Carillon *et al*. in 2013, over 30 years of studies using natural SOD are discussed and some of the benefits obtained will be discussed in this section[64].

Diverse *in vivo* studies have shown that animals exposed to ionization irradiation and upon SOD administration present less side effects rising surviving rates. Moreover, regarding inflammatory diseases, analysis in mice to which Cu/Zn SOD was applied in some joints showed significant treatment improvements, similarly, attenuation of symptoms was observed for ischemia reperfusion models[64].

Continuing, SOD has shown potential regarding the prevention of the progression of tumors in mice. Regarding acquired immunodeficiency syndrome, the use of Cu/Zn-SOD inhibit the process of replication of HIV and did not allow viral transmission. Finally, regarding brain function, oral administration of SOD showed to benefit memory and learning in models of mice[64].

1.5.1 Disadvantages of using native SOD

Despite of the multiple advantages, SOD is not so easy to administrate due to its size and weight that affects its permeability through the cell. Furthermore, the enzymes requires special conditions of conservation and can quickly decomposes in the system[65]. Currently, scientist are working on generating compounds of low molecular weight that mimic SOD activity, and one successful alternative has been metal complexes that resemble the active site of the original enzyme[66].

1.6 SOD biomimetics

Significant part of the research regarding SOD mimetics have been focused on complexes because metals are good to be involve in redox cycling processes. Nevertheless, one disadvantage is that the metal could be liberate from its coordination sphere and participate in Fenton reactions[67]. In general, the SOD mimetic behavior depends on the nature of the ligands, geometry and how these complexes interact in live organisms. A wide variety of complexes have been studied with different types of ligands. As in nature, a very common approach is the development of binuclear complexes usually with bridges through nitrogen base ligands [65].

Manganese is a common metal used in SOD mimetics because it has the advantage that if the ion liberates from the complex, Mn^{2+} can catalyze the reaction of superoxide anion to peroxide and oxygen. The most common type of ligand used for manganese biomimetics are porphyrins, which are common ligands in biology. Another common kind of ligand for manganese are cyclic polyamines. Furthermore, manganese-*salen* like complexes have been studied not only *in vitro* but also *in vivo*, already reaching the step of clinical trials[67]. In this manner, some of the initial work in the area of SOD biomimetics started back on late 1970 with the development and testing of metalloporphyrin by Pasternack *et al.*[67]. Later on, the focused of studies shift to manganese-*salen* complexes being the simpler ones reported by Malfroy *et al.* back on 1993 and ever since, modifications to salen complexes have been study[68].

Beside the coordination complexes alternative, other compounds also have been proposed. One of the explored options has been fullerenes' specially the water-soluble ones. Another, is the use of nitroxides[67]. Other development has been metal and metal oxides nanoparticles (NPs) promising for its ability to cross diverse barriers as the ones in the brain[69].

The usual requirements for efficient SOD mimetics have been established through the years of testing. First, the metal must be able to participate in redox cycles of one electron. Second, regarding thermodynamic factors, the redox potential of the metal is required to be in an adequate range. The range is usually between the two catalyzed reactions E ($O_2/O_2^{\cdot-}$) = -0.16 V and E($O_2^{\cdot-}$ /H_2O_2) = 0.94 V (vs NHE) at pH 7. The best potential is usually about 0.36 V that relates with the ones of natural enzymes[69]. Although this is an important factor commonly observed in many biomimetics, it is not essential in all the cases as some SOD mimetics do not fulfill this requirement[69].

1.6.1 Measurements of SOD activity

There are different ways to determine SOD capacity, the most common one is by indirect method. In this analysis, superoxide radicals are generated and there is an indicator capable of interacting with superoxide radical to produce a specific spectroscopic response. Then, upon addition of the SOD mimetic, the level of the radical would be reduce affecting the spectroscopic response which can be quantified. There are many ways to set up the experiment, however, the most common method is the one in which the radical is produced by xanthine/xanthine oxidase and nitro blue tetrazolium used as indicator. The specific value obtained is IC_{50} that represents the concentration

of biomimetic that produces half the inhibition of the indicator. This is the most common reported value. However, for this to be useful for comparison in literature, the setup of the experiment must be equal, which is not always the case. Therefore, in the following section, the IC_{50} are reported but these should not be used for comparison between different research[70].

1.6.2 Examples of SOD mimetics

A small review regarding some previous work of SOD biomimetics with ligands similar to ours, the ones present in this work, would be discussed. The complexes studied in different published research will be analyzed in the following subsections. For each research work analyzed, the structure of the complexes studied will be shown (if just one compound is shown, it is the one with best SOD activity).

1.6.2.1 *SOD mimetics with salicylic acid and its derivatives*

In 2016 Puchoňová *et al.* [66] developed copper complexes with ligands derivate from salicylic acid and nitrogen donor ligands. At the end, mononuclear and binuclear complexes were obtained. The best SOD activity was found for the dimeric complexes, the best one with IC_{50} = 2.24 µM[66] show in Figure 10 **(1)**. In 2018 Savithri *et al.* [71] proposed new cobalt and copper complexes with ligands derivative from chlorophenol and fluorobenzothiazole condensation using or not 1,10-phenanthroline as a coligand. The SOD activity test for the copper complexes showed IC_{50} values between 0.13–1.02 µM.[71], the most promising SOD mimetic compounds of these research papers can be found in Figure 10 **(2).**

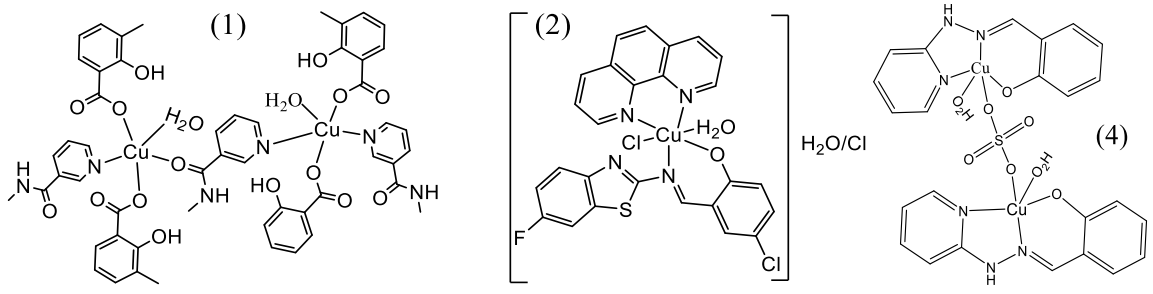

Figure 10 Best complexes from the papers of Puchoňová et al. , Savithri et al. and Patel et al. [66,71,72]

Later, in 2020, Siqueira *et al.* [73] reported six new copper complexes (mononuclear and binuclear) that use ligands derivate from salicylic acid or pyridoxal and hydrazides. Interestingly, some of the ligands have different substituents in the *para* position. The SOD activity was tested with NBT,

in vivo with nematode and *in silico*. The electrochemical analysis show that the reduction potentials greatly depend upon the *para* substituent. The complexes that gave the best results possess *para* substituents -NH_2 and -OH. The NBT analysis show IC_{50} for these complexes between 0,11-1.51µM, which is very promising.

In the *in vivo* analysis, worms were exposed to the different SOD biomimetics, in different concentrations, before being exposed to a generator of superoxide. It was observed that the worms protected by SOD biomimetics showed higher survival rate than control group. While in silico, the analysis was through docking of the complexes with superoxide ion, showing relation between SOD activity and the distance between the metal center and superoxide anion. The different tested compounds in this research are observed in Figure 11[73] **(3).** Finally, in 2020 Patel *et al.* [72] developed complexes with ligand derivate from 2-hydrazinopyridine and salicylaldehyde. The resulting complexes were binuclear with IC_{50}= 3.9 and 8.6 µM, being the best compound the one shown in Figure 10 [72] **(4)**.

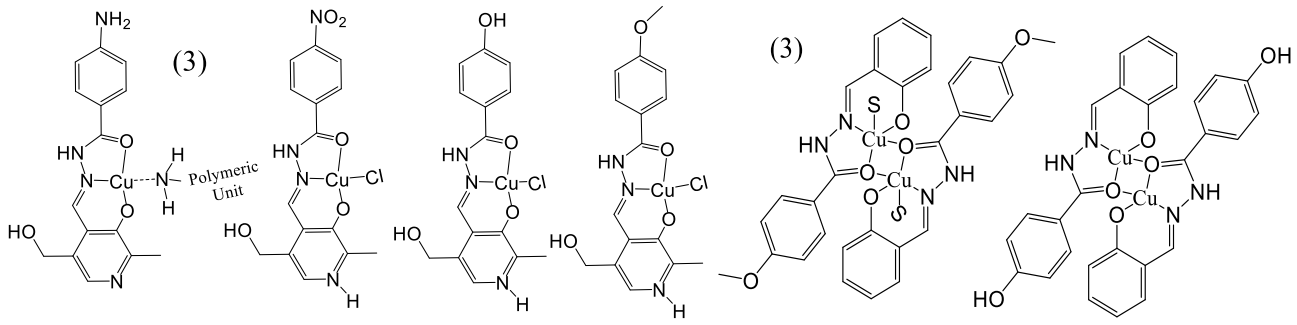

Figure 11 Proposed complexes by Siqueira et al. in 2019 [73]

1.6.2.2 *SOD mimetics with vanillin and o-vanillin*

As early as 2010, González-Baró *et al.*[74] synthetized copper complexes with o-vanillin and vanillin. It was observed that redox potential of vanillin was slightly more positive than for o-vanillin 1,05V and 0,99V which relates with more antioxidant activity of o-vanillin. Regarding SOD activity, it was very similar with IC_{50} of 11 µM and 12 µM for complexes with o-vanillin and vanillin, respectively. The good activity is related with the axial ligands and the easiness to reach the metal due to the plane geometry of the ligands[74], the studied complexes are shown in Figure 12 **(5)**.

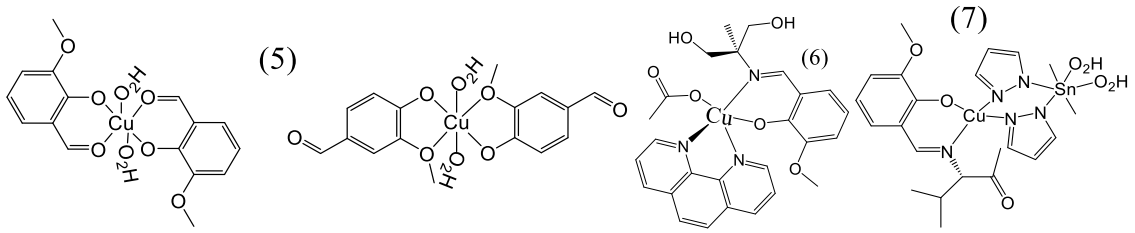

Figure 12 complexes proposed by González-Baró et al. 2010, Tabassum et al. 2013 and Tabassum et al. 2015[74–76].

In 2013, Tabassum *et al.* [75] developed copper complexes with ligands derivate from o-vanillin and 2-amino-2-methylpropane-1,3-diol. In general, the complexes present IC_{50} values ranging between 0.58 and 11.40 µM. The best result was for the complex with 1-10phenanthroline, demonstrating that there is a significant effect of coligands, the best SOD biomimetic compound is shown in Figure 12[75] **(6).** Continuing with the research, Tabassum *et al.* in 2015[76] proposed mononuclear copper and zinc complexes and hetero-binuclear compound of copper/zinc and tin with ligands from L-valine and o-vanillin. The SOD activity was only measured for the binuclear complexes, the one with copper was the best having an IC_{50} = 0.082 µM [76] as observed in Figure 12 **(7)**.

Similarly, in 2019 Afsan *et al.* [77] worked developing copper complexes. The ligands used are enantiomeric allowing to discuss this special parameter formed by the condensation of o-vanillin and L or D phenylalanine. Regarding SOD activity, it is interesting that the enantiomeric nature of the ligand has some effect on the results being for IC_{50} 0.160 and 0.198 µM (L and D) respectively[77] being the L conformer shown Figure 13 **(8)**. Finally, in 2020, Dong *et al.*[78] proposed homobinuclear nickel complexes with one ligand derivate from L-alanine and o-vanillin and the other being 1,10-phenanthroline, the best complex presented a IC_{50} of 31.1 µM[78] **(9)**. The best compounds of these research papers are shown in Figure 13.

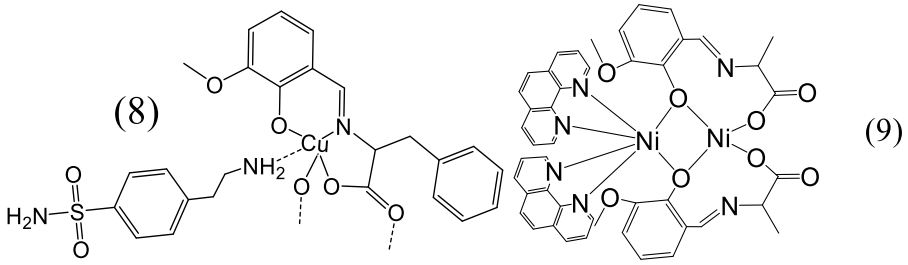

Figure 13 Complexes proposed Afsan et al. 2019 and Dong et al. 2020 [77,78]

1.6.2.3 *SOD with salen like ligands*

Salen ligands are formed through the condensation between salicylaldehyde and diamines. These show diverse chemistry as there are many derivatives from salicylaldehyde as well as multiple kinds of diamines[79]. These types of ligands have been widely studied, the behavior of these ligands is highly affected by the nature of the amine because it influences the geometry and characteristics of the bridge[68]. Salen complexes coordinated with manganese have been study for a long time as antioxidants agents, some of them have proven to be interesting SOD biomimetics. As early as 2000 these shown interesting properties, as main examples are EUK-8, EUK-134, and the alkoxy substituent EUK-189 which structures are shown in Figure 14. These tend to be planar but slightly affected by axial substituent such as solvent molecules or chlorides that can be easily exchanged to allow the biomimetic behavior[79].

For example, EUK-8, EUK-189 and specially EUK-134 were promising in mice with deficient SOD2 in oxidative neurodegenerative process, their lifespan was increased, and the usual indicators of neuropathy were eliminated. Furthermore, EUK-189 showed easiness for entering the brain barrier. Moreover, other study shown that SOD can help to prevent phenotypes of neurodegenerative diseases in mouse used as models for Alzheimer's disease. In further studies, EUK-189 and EUK-207 seemed promising in approaching the treatment for memory deficit and learning in mouse models.

Many other studies have been made for animals' models with multiple inflammatory diseases such as myopathies, acute pulmonary inflammation, radiation induce lung effect, and lung damage showing promising results for treatment. Some special attention has been put in skin, for example, for skin transplant in mice, EUK-8, EUK-143 and EUK-189 increased the days before rejection and increase skin graft survival. Moreover, EUK-134 is currently sold commercially. At the end, there is not a prefer salen candidate because each present benefits but all differ in their properties, especially in biological ones[79].

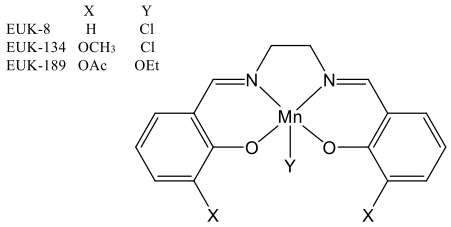

Figure 14 Discussed SOD mimetic with salen ligands Rouco et al. [79]

1.6.2.4 *SOD mimetics with aniline and its derivatives as ligands*

In 2014, Joseph and Rani [80] developed complexes of iron, cobalt, nickel, copper and zinc, where copper complexes showed the better results. Also, a significant solvatochromic effect was observed for the d-d transitions in organic solvents [80] **(10)**. Further studies of Pereira *et al.* in 2018[81] proposed copper complexes with ligands obtained from the reaction of pyridoxal with five different halogenated anilines derivatives in ortho position. The IC_{50} values obtained range from 0.4 to 48.3 µM being the best substitution iodine and the lowest fluor[81] **(11)**. In this same year, Sangeeta *et al.*[82] worked in developing nickel complexes with Schiff bases made from 4-bromo-2-chlorobenzenamine. The SOD activity was tested for ligands and complexes, the best complex showed an IC_{50} of 7.15 µM [82] **(12).** The compounds that showed best SOD mimetic activity from each of the discussed research in this paragraph are shown in Figure 15.

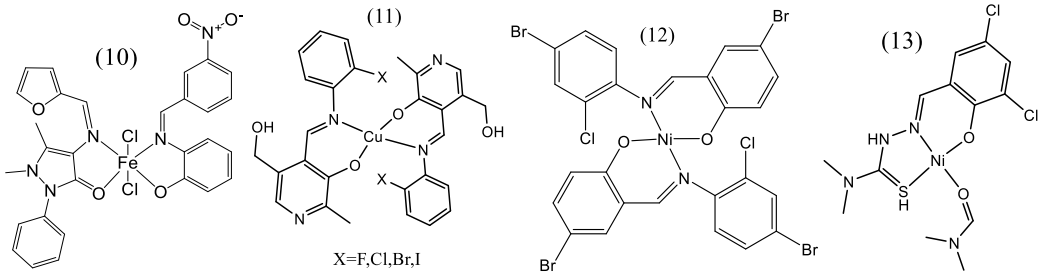

Figure 15 Joseph and Rani in 2014, Pereira et al. in 2018, Sangeeta2018 and Mohan et al. 2018 [80–83]

In 2018, Mohan *et al.*[83] developed mononuclear copper and nickel complexes using ligands like 3-bromo-2-hydroxy-5-nitrobenzaldehyde and 4-bromo-2-chlorobenzenamine. The copper complex showed in Figure 15 **(13)** presented the best SOD performed with 68 µM[83] .

1.7 Computational principles

1.7.1 Important programs for computational analysis

Nowadays, it is becoming very common to use computer programs to complement laboratory studies in diverse fields such as in chemistry. One of them is Avogadro used for a broad range of applications, one of them computational chemistry. Avogadro is a free software that allows to construct molecules, visualize (molecules and orbitals), measure parameters among many other operations. Also, it supports the creation of inputs for further theoretical calculations and the analysis of the obtained results[84].

On the other hand, Orca is also a free software that has become one of the most widely used quantum chemistry program around the world. It allows the use of diverse method such as Hartree-Fock, semi-empirical, force field, density functional theory and many others. Orca performs calculation regarding optimization of geometry, energy analysis, solvation, excited states among others. The analysis to encounter the energy minima is the first and truly necessary step for any further calculations[85]. Moreover, ORCA was designed thinking on the analysis of transition metals. One of Orca's strength is the spectroscopic analysis allowing calculations for UV-Vis, magnetic circular dichroism, electron paramagnetic resonance, infrared, Raman, fluorescence and others[86,87].

1.7.2 Density functional theory

There are different methods available to make computational analysis, one of them density functional theory (DFT) used to determine information relative to the structure and energy of diverse molecules[88]. The biggest problem is that the ground state can be calculated with some level of precision, but it is not completely accurately. Something similar is observed for the electron density since the exchange-correlation function is unknown, but many different options has been used to represent the functional each yielding different results. As the development of theory improves, many more alternatives are propose as DFT hybrid methods[89].

DFT improves the calculation time required referent to Hartree-Fock for many electron system due to its concept of defining the potential as a functional of electron density[90]. Indeed, over the past decades, DFT has grown to be one of the preferred methods for computational calculations. Beside the reduce calculation time, DFT has become popular because it has a significant precision compare with other methods. The improved precision is related with the exchange-correlation term for the energy, the advantage of DFT over other methods is the correct inclusion of the correlation energy from the beginning of the calculations [91].

1.7.3 Time dependent density functional theory

DFT is very useful for diverse analysis but in the ground state of molecules, however, molecules can experiment diverse processes in excited states[92]. Time dependent density functional theory (TDDFT) can be used for the simulation of processes of electron excitation[93]. TDDFT has been found to be useful specially for spectroscopic simulation for its accuracy[94] allowing to obtain information of transition intensities and energies as well as the strength of the oscillator even for

large number of transitions in a UV-Vis analysis. It has been observed that for the study of UV-Vis from metal complexes is more favorable using hybrid exchange-correlation functionals[95] .

1.7.4 Computational approach

For accurate results in quantum calculation, many parameters must be considered such as dispersion, suitable density functional, a correct basis set, and so on[96]. Regarding the latter, for computational calculations, a basis set is a mathematical way that allows to describe the molecular orbitals of the system that is going to be studied. As can be imagined, depending on the specific of the mathematical analysis and equations, different kinds (families) of basis sets have been developed such as: minimal, Pople, correlation consistent, plane wave, split valence among many others basis sets. An extensive discussion of each type of basis set can be find in the book *Computational Chemistry and Molecular Modeling* by Ramachandran *et al.*[97]. For this work, special attention is given for the def2 family of basis sets created by Ahlrichs, its name stands for second-generation default basis set. This family has become important in computational chemistry due to its accuracy to represent the elements throughout the periodic table [98]. The def2 prefix is used to not confused it with earlier versions, these basis sets are recommended to be used instead of the previous *def* for the improvements made, the most common basis sets of this family are: def2-SV, def2-TZV and def2-QZV[99].

Regarding the basis set def2-SVP, SV stands for split valence characterized for using a mathematical function for internal orbitals (orbitals not located in the valence shell) and two functions for the orbitals in the valence shell. Meanwhile, def2-TZVP is a triple-zeta (TZ) basis set that has three mathematical functions for the valence orbitals. Finally, for both of them, the P indicates that a polarization function is used[97] . In general, a better result is expected for larger basis sets, but it also implies higher computational resources. For computational experiment, it is common to use def2-SVP, but it may overestimate some non-covalent interactions. Therefore, it is recommended to use a triple-zeta basis set such def2-TZVP[96]. Moreover, def2-TZVP has been widely recommended for calculation that contain 3d transitions metals due to its accuracy[100].

One of the most common functional used in theoretical chemistry is B3LYP[101]. B3LYP is a hybrid exchange functional. B3 stands for the combination of three Becke's exchange-parameter functional and LYP stands for the nonlocal correlation functional considered due to Lee, Yang, and Parr[102]. Although this functional is widely used, it may not fully represent long chain system,

and is inaccurate for calculation using TDDFT and charge transfer processes. Meanwhile, CAM-B3LYP is an exchange-correlation functional which takes into account long-range corrections that improves the performance compare to B3LYP but at higher computational cost[101].

Indeed, one of the clear advantages of CAM-B3LYP is that it combines the hybrid qualities of B3LYP previously discussed and it includes correlation at long ranges. The latter is included with CAM that states for Coulomb-attenuated functional[103] which has an α and β parameter which allow the introduction of Hartree Fock exchange contribution and DFT of the same parameter respectively[101]. This correlation is important and representative in many systems. In general, the functional behaves differently depending in whether it is used for short or long ranges. In the case of short ranges, it presents 0.19 Hartree Fock and 0.81 Becke 1988 exchange interaction. Meanwhile, at long distances, it presents 0.65 and 0.35 respectively[101]. It has been reported that CAM-B3LYP has shown to performed better for electronic spectra simulation[103]. Indeed, UV-Vis simulation quality is better when compared with other functionals such as B3LYP or PBE[104]. Moreover, besides its great performance, it has shown to be accurate specially when the excited states shows to be deslocalized[105].

In general, DFT is not capable of correctly representing dispersion interactions which worsen at larger distances. To improve the results, a correction of the unrepresented interaction can be made using an additional term of attractive energy for the system such as the Becke-Johnson damping (D3BJ) [106]. Finally, conductor-like polarizable continuum model (CPCM) helps to take into consideration the diverse effects of the solvent by representing it as a dielectric polarizable continuum[107].

1.7.5 Computational prediction of biological activity

It has been widely discussed that highest occupied molecular orbital (HOMO) and lowest unoccupied molecular orbital (LUMO) orbitals are important for many properties of compounds, as its capacity to receive or donate electrons. Moreover, the energy difference between them is related to its reactivity, and their values are used to calculate multiple reactivity parameters[108]. Molecules with small energy gap are considered as soft molecules, easy to polarize and offer electrons. One of the biological activities to which frontier orbital theory has been related is SOD mimetics, the selected parameter is electronic affinity that correlates to how easy a compound would donate electrons which relates with one step of the SOD mechanism[109].

Suksrichavalit et al. in 2009[110] , found that HOMO and LUMO energies could be correlated with the logarithm of IC_{50} obtaining a regression coefficient of r = 0.97 and r = 0.99 respectively. The reason for this correlation to exist, is the fact that SOD capacity is strongly correlated with electron transfer processes which would be simpler depending on the frontier orbitals energy. Another important parameter, is that SOD biomimetics are better when their axial bonds are longer[110], therefore, metals that allow effects as Jahn Teller as copper are good candidates for SOD biomimetics. In 2008, Suksrichavalit et al.[111] relate that high HOMO values have been correlated with low SOD activities[111] .

The most recent research in this area has been in this year 2021, to the best of our knowledge, by Silva *et al*.[112] A detailed analysis of the structures helped to put light onto the SOD mimetic activity based on computational calculations. For example, geometry parameters are used to characterize the coordination environment around the metal upon gain of one electron in the reduction step. Moreover, electron affinity was calculated for compounds showing that the more negative the better SOD activity. All this information in the future could be used to create and predict best candidates for SOD mimetics. Finally, analysis of the orbitals helps to understand which part of the compounds is truly involve in the redox processes, and the electrophilicity helps to determine the attraction of the compound to electron rich species [112].

Additionally, computational calculations are important to understand the mechanism of catalysis for the SOD biomimetics. For example, Lu *et al.*[113] analyzed computationally the plausible mechanism for some copper SOD biomimetics. The redox process includes two half reactions, oxidation and reduction. The geometries are calculated in these two oxidation states for the complexes, complexes including the superoxide anion and the corresponding transition states. In this sense, the analysis of changes on bond length, angles and energy values is essential. One crucial part in the mechanism is to determine which atom would protonate and then give the proton up for the formation of peroxide which is determine upon values of energy of the different possibilities of protonation[113] .

Although the analysis of mechanism is important, another common approach for SOD mimetics is to initially just analyze the structural changes of the complexes in the two redox states involve in the SOD activity without addition of any extra atom. For example, for copper, the geometries for Cu^{2+} and Cu^{1+}. This allows to determine whether a bond is broken during the redox process, as

well as possible changes in the angles and geometry [112,114]. This can initially give some insight to begin to figure out the plausible mechanism of the biomimetics.

Chapter 2. Problem statement

2.1 General problem statement

Oxidative stress has shown to be involved in multiple diseases such as inflammatory diseases, Alzheimer's diseases, diabetes and so on. Although the body tends to manage the unbalance of ROS, in many of the cases, external agents are required to reduce harmful effects. For that reason, there is a need to continue searching for better proposal of SOD biomimetics as these can be beneficial for a wide range of clinical affections. As discussed in the previous chapter, there has been a significant amount of research about coordination complexes that could serve as SOD biomimetics. Coordination complexes are preferred for this purpose due to the metal's redox capability for electron transfer. The main metals used in SOD biomimetics are copper, manganese, iron, and cobalt. Most of them are the cofactors found in nature in SOD metalloproteins. Many SOD biomimetics have showed to be promising *in vivo, in vitro,* at clinical trials and some even are currently sold solving some of the problems faced in the use of native SOD.

Nevertheless, in many cases, the SOD mimetic capacity is not as promising as initially expected and the reason for its failure is not always clearly understood. Moreover, most of the research does not count with computational approach even thought, it has become a common tool for research. In the recent years, computational approach has entered the research area of SOD mimetics in which parameters from orbital energies, docking and reactivity have been used. It is imperative to start using computational approaches to propose rational synthesis of the best candidates for SOD mimetics, to understand the effects of small changes in structure and to get an insight of their mechanism.

2.2 Objectives

2.2.1 General objectives

- Synthesize copper and manganese complexes with Schiff base ligands and perform a theoretical study on the spectroscopic and structural properties of the complexes as an initial step towards the development of a new set of SOD biomimetics.

2.2.2 Specific objectives

- Synthesize copper and manganese complexes with Schiff base ligands derivate from vanillin and amines (ethylenediamine, aniline and its derivatives)
- Characterize the complexes using Fourier transformed infrared spectroscopy, UV-Vis and Magnetic balance
- Use DFT for geometry optimization and Fourier transformed infrared spectroscopy simulation
- Use TDDFT for UV-Vis simulation
- Predict the best SOD biomimetic based on computational parameters

Chapter 3. Methodology

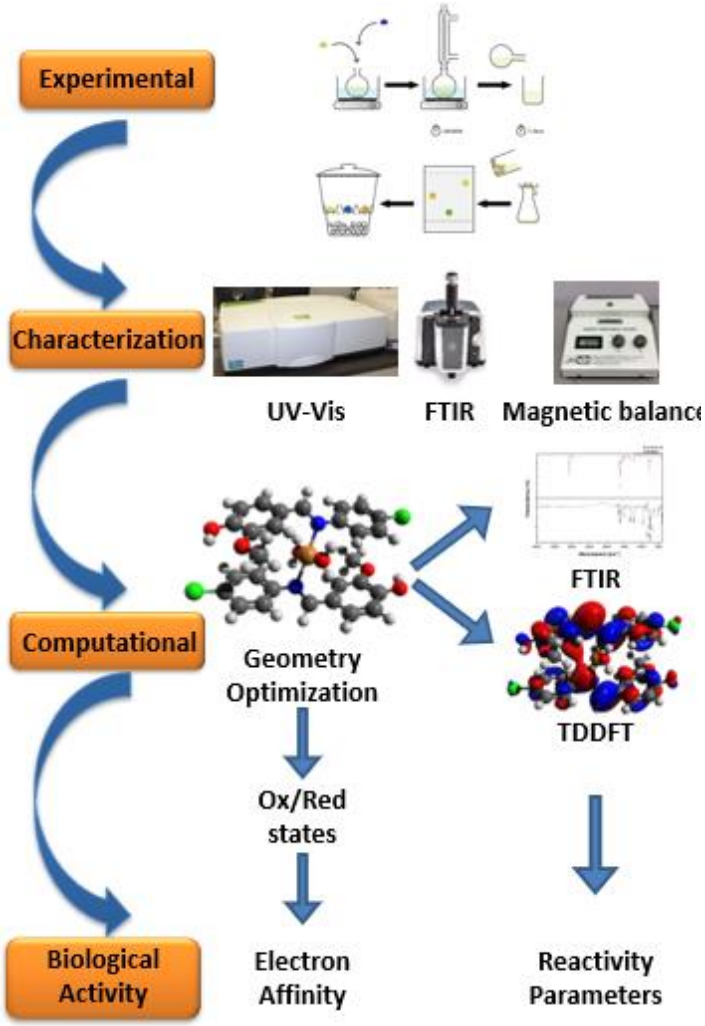

Figure 16 General Methodology carried out during the research project.

In this section, the general methodology for the project would be described. This chapter is divided in two subsections in which one focuses on laboratory part and the other in the computational analysis. The general methodology is shown in Figure 16.

Initially, the ligands and complexes are synthetized and characterized. Then, a geometry optimization is proposed for the neutral compound from which IR and UV-Vis simulation are obtained. This step is repeated until the theoretical and experimental results are consistent. Next, using the coordinates from the optimized structure, the geometry of the ligands/complexes in it oxidize or reduced state is determined. Finally, using the UV-Vis results, the energies of HOMO and LUMO are used to determine reactivity parameters.

3.1 Laboratory section

3.1.1 Reagents and equipment

3.1.1.1 *Reagents*

All the reagents used for this project are summarized in Table 1.

Table 1 Reagents used for the synthesis of compounds

Reagents	
Aniline (ACS reagent ≥ 99.5%, SIGMA-ALDRICH)	4-aminophenol (for synthesis, Merck KGaA)
Ethylenediamine (puriss. p.a. absolute, ≥ 99.5% (GC), SIGMA-ALDRICH)	p-Toluidine (99%, ALDRICH)
Vanillin (Laboratory School of Chemical Science and Engineering, not specify)	Copper sulfate (Laboratory School of Chemical Science and Engineering, not specify)
4-Chloroaniline (98%, ALDRICH)	Manganese chloride (Laboratory School of Chemical Science and Engineering, not specify)
Ethanol (99%, Distribuidora M&M-Ibarra)	Acetonitrile (HPLC grade, SIGMA-ALDRICH)

3.1.1.2 *Equipment*

- Melting point

Melting point was measured using melting point apparatus of Electrothermal from Fisher scientific from the School of Chemical Science and Engineering of Yachay Tech. Initially, melting point capillaries needed to be sealed, and then fill a height about 2 mm with the compound. The range of temperature used was from 50 °C to a maximum of 300 °C using a changing of 10 °C/min.

- Fourier transformed infrared spectroscopy

All Fourier transformed infrared spectroscopy (FTIR) measurements were made in solid state by attenuated total reflectance (ATR) using spectrophotometer Agilent Cary 630 FTIR in a range of 4000-400 cm^{-1} with 32 sample scans and 32 background scans. The equipment belongs to the School of Biological Science and Engineering of Yachay Tech University.

- UV-Vis Spectroscopy

The measurements were made using Perkin Elmer LAMBDA 950 UV/Vis/NIR in the laboratory of the School of Chemical Science and Engineering at Yachay Tech University. The measurements were obtained in solid and liquid state. For the solid measurement, the praying mantis accessory was used. Meanwhile for liquid measurements, a solution of $1x10^{-3}M$ in ethanol for most of the compounds, but some of them in acetonitrile in case of solubility problems (would be specified on the results). In case that the signal is saturated, the solution was diluted (500 µL of the mother solution were diluted in 2 mL of pure solvent either ethanol or acetonitrile). This process was repeated until the measurement of charge transfer part was not saturated. The wavelength range of the measurement was 175 to 800 nm, but on some occasions up to 1200 nm.

- Magnetic balance

Initially, the compounds were pulverized using an agate mortar. Then, the empty test tubes of the machine were weighted. Following, these were filled 2 cm of height with the compounds, it must be tightly packed to avoid any bubbles of oxygen. Later, the tube was placed on the magnetic balance to obtain the magnetic measurement. In this sense, the balance measures the magnetic response of the material to an external fixed magnetic field (whether it is diamagnetic or paramagnetic). Using this measurement, it is possible to calculate magnetic susceptibility of the compound. Finally, the filled tube is weight once again. The measurements were made using Sherwood Scientific magnetic susceptibility balance in the laboratory of the School of Chemical Science and Engineering at Yachay Tech University.

3.1.2 Synthesis of ligands and complexes

In this section, the synthetic routes for the different ligands and complexes are described. The general laboratory set up for the synthesis can be observed in Figure 17.

Figure 17 Experimental set up for the synthesis of ligands and complexes

3.1.2.1 *Synthesis of 4,4'-((1E,1'E)-(ethane-1,2-diylbis(azanylylidene))bis(methanylylidene))bis(2-methoxyphenol) [L1]*

The synthesis of **L1** was carried out according to the procedure previously reported by Dineshkumar, Muthusamy and Chandrasekaran in 2016 [115] with slight change in solvent. First, 4 mmol of vanillin were dissolved in 30 mL of ethanol. Then, 2 mmol ethylenediamine were added to the solution dropwise while vigorously stirring. The reaction was kept for 1 hour under stirring and reflux. Then, the yellow solid was vacuum filtered. Once completely dry, the resulting product is dissolved in acetonitrile while slowly increasing the heat but avoiding boiling. Then, as it starts to deposit, it was filtered while still hot and allowed to dry at room temperature.

3.1.2.2 *Synthesis of ligands derivate from vanillin with aniline and its derivatives.*

In total, four ligands were synthetized. The IUPAC names of the ligands are 2-methoxy-4-((phenylimino)methyl)phenol [**L21**], 4-(((4-hydroxyphenyl)imino)methyl)-2-methoxyphenol [**L22**], 4-(((4-chlorophenyl)imino)methyl)-2-methoxyphenol [**L23**] and 2-methoxy-4-((p-tolylimino)methyl)phenol [**L24**]. The synthesis of the series of the ligands **L21** to **L24** is similar since their general structure is almost the same. The synthesis of **L21** was previously reported [116] and used with small changes for all the ligands.

The general procedure was to completely dissolve 0.02 mol of vanillin on 30 mL of ethanol. Then, 0.02 mol of the amine (aniline, 4-chloroaniline, 4-aminophenol or toluidine) were added slowly to the previous solution while stirring a change of color to yellow was observed. Finally, few drops of glacial acetic acid were added. This mixture was stirred and refluxed for about 4-7 hours depending on the amine. The reaction was followed using thin layer chromatography (TLC) (35% acetate: 65% hexane) to monitor the consumption of the amine reagent. Later, the solution was transferred to a beaker to allow solvent evaporation for about three days, time in which crystal were formed. Finally, the obtained crystals were vacuum filtered and recrystallized in ethanol and acetonitrile. It is recommended to maintain the compounds in a desiccator.

3.1.2.3 *Synthesis of complex di(aqua)4,4'-((1E,1'E)-(ethane-1,2-diylbis(azanylylidene)) bis(methanylylidene))bis(2-methoxyphenol)-κ-N,N-copper(II) sulfate [Cu1A]*

In a round flask, 2 mmol of **L1** were completely dissolved in 30 mL ethanol. Then, 2 mmol of copper sulfate were added. The reaction was maintained under refluxed for seven hours. Initially, the color of the complex was dark blue, but as time passes by it change to light blue. No recrystallization was made.

3.1.2.4 *Synthesis of complex trans-di(aqua)bis(4,4'-((1E,1'E)-(ethane-1,2-diylbis(azanylylidene))bis(methanylylidene))bis(2-methoxyphenol))-κ-N,N-copper(II) sulfate [Cu1B]*

Similar to the previous one, but 4 mmol of **L1** were used instead, the obtained complex was purple.

3.1.2.5 *Synthesis copper complexes with ligands L2X*

In total, three complexes were synthetized with copper. The complexes are: Trans-di(aqua)di(2-methoxy-4-((phenylimino)methyl)phenol)-κ-N-copper(II) sulfate **[Cu21]**, Trans-di(aqua)di(4-(((4-chlorophenyl)imino)methyl)-2-methoxyphenol)-κ-N-copper(II) sulfate **[Cu23]** and Trans-di(aqua)di(2-methoxy-4-((p-tolylimino)methyl)phenol)-2-methoxyphenol)-κ-N-copper(II) sulfate **[Cu24]**. The synthesis for **Cu21** was previously reported by Tufa et al., in 2018 [117]. The synthesis was similar for all these complexes, 2.5 mmol of copper sulfate were dilute in ethanol while stirring until completely dissolved. Then, 5 mmol of the specific **L2X** ligand was added to the round flask. The reaction was maintained under reflux with continuous stirring for 3 hours. Then, the resulting solid was filter in vacuum. Finally, it was recrystallized from ethanol.

3.1.2.6 *Synthesis of manganese complexes with L2X*

In total four complexes were synthetized using L2X. The complexes are: Trans-di(aqua)-di(2-methoxy-4-((phenylimino)methyl)phenolato)-κ-O,O-manganese(II) **[Mn21]**, Trans-di(aqua)-di(4-(((4-hydroxyphenyl)imino)methyl)-2-methoxyphenolato)-κ-O,O-manganese(II) **[Mn22]**, Trans-di(aqua)-di(4-(((4-chlorophenyl)imino)methyl)-2-methoxyphenolato)-κ-O,O-manganese(II) **[Mn23]**, and Trans-di(aqua)-di(2-methoxy-4-((p-tolylimino)methyl)phenolato)-κ-O,O-manganese(II) **[Mn24]**. Similar procedure as explained in 3.1.2.5 but instead of copper sulfate, manganese chloride was used.

3.2 Computational approach

3.2.1 Geometry optimization

Initially, Avogadro was used to draw the initial structures of ligands and complexes. Then the tool from Avogadro to generate Orca inputs was used. All the compounds were optimized with the method CAM-B3LYP, basis set Def2-TZVP and including D3BJ. In all the cases, ethanol was used for CPCM model since all compounds were synthetized in this solvent. Initially, the ligand was optimized in its singlet state and the optimized structure was used to calculate the doublet state. Something similar was done for the complexes, in the case of copper initially was calculated for Cu^{2+} then for Cu^{1+}, and for manganese initially Mn^{2+} then Mn^{3+}. The input used for the geometry optimization for this work is specify in Figure 18.

```
# avogadro generated ORCA input file
# Basic Mode
#
! CAM-B3LYP OPT D3BJ def2-TZVP CPCM(ethanol) PAL4
```

Figure 18 Input for Geometry optimization

3.2.2 Infrared spectroscopy calculation

The coordinates from the previous geometry optimization were used to calculate infrared (IR) frequencies using ORCA. The results showed no imaginary transitions, indicating that minima were obtained and the scaling factor of 0.951 was used[118]. The method and basis used were the same as for geometry optimization, however, CPCM was not used as it is not supported for frequency calculations in Orca. The input used for the calculation of IR spectrum is shown in Figure 19.

```
# avogadro generated ORCA input file
# Basic Mode
#
!CAM-B3LYP FREQ D3BJ def2-TZVP PAL4

* xyz 0 6
```

Figure 19 Input for IR calculation using ORCA

3.2.3 Time dependent density functional theory calculations

The coordinates of the optimized structures of section 3.2.1 were used as input for the UV-Vis calculation. The solvent in CPCM would be ethanol unless specify otherwise in the results. Initially, nroots (number of calculated transition states) is set to 50. In cases that these transitions do not cover the whole spectrum experimentally measured, the number was increased. For this part of the analysis, new parameters for calculation are added. The input was made based on RIJCOSX TDDFT calculation input as suggested by ORCA input library. The input for ORCA used for this work in shown in Figure 20.

```
# avogadro generated ORCA input file
# Basic Mode
#
! CAM-B3LYP D3BJ def2-TZVP def2/J RIJCOSX Grid5 FinalGrid6 TightSCF CPCM(ethanol) PAL4
%maxcore 1000
%tddft
  maxdim 5
  nroots 50
end
%output
Print[ P_Basis ] 2
Print[ P_MOs ] 1
end
```

Figure 20 Input for TDDFT calculations

3.2.3.1 *Reactivity Parameters*

With the values obtained for HOMO and LUMO from the TDDFT analysis, different parameters are calculated to discuss about the reactivity of the ligands and the complexes. The definition of each equation is shown in below [112] .

$$\text{Chemical Hardness } (\eta) = \frac{-E_{HOMO}-(-E_{LUMO})}{2} \quad \textbf{(1)}$$

$$\text{Chemical Potential } (\mu) = -\frac{-E_{HOMO}-E_{LUMO}}{2} \quad \textbf{(2)}$$

$$\text{Electrophilicity } (\omega) = \frac{\mu^2}{2\eta} \quad \textbf{(3)}$$

Furthermore, for the prediction of SOD activity, electron affinity is calculated using the energy of the optimized structures from 3.2.1 with the equation **(4)** show below [112].

$$EA = Total\ Energy_{reduced} - Total\ Energy_{neutral} \quad \textbf{(4)}$$

3.2.3.2 *Geometry parameters*

Most of the complexes that would be encountered on this project possess tetrahedral or square planar geometry. Therefore, the geometry index for complexes coordinated with four ligands would be used (τ), which is given in equation **(5).** The values of τ ranges from 1-0, a value of 1 is a perfect tetrahedral and a value of 0 a perfect square plane. The angles α and β represent the biggest angles found in the structure formed between the ligands and the metal[112], the general formula is shown in equation **(5)**.

$$\tau = \frac{360° - (\alpha + \beta)}{141°} \quad \textbf{(5)}$$

Chapter 4. Experimental and theoretical results and discussion

This section will focus on the discussion of the results obtained in the laboratory and how these relate with the computational simulations. Moreover, how using the theoretical results, the biological SOD activity can be predicted. This chapter has six sections, five sections would present the different ligand (**L1** and **L2X**) and the coordination complexes synthetized with them. In each section, the geometry optimization, FTIR, UV-Vis (liquid and solid), magnetic balance and biological activity would be discussed. The final section focused on a summary of the obtained results.

4.1 L1 and its complexes

4.1.1 Analysis for L1

The reaction scheme for **L1** is shown in Figure 21, this ligand is inspired on salen like ones which have been widely used for biomimetic complexes of SOD. The color of the compound is light yellow with a yield of 83.15 %. This ligand is soluble in many organic solvents such as ethanol, acetonitrile, and methanol.

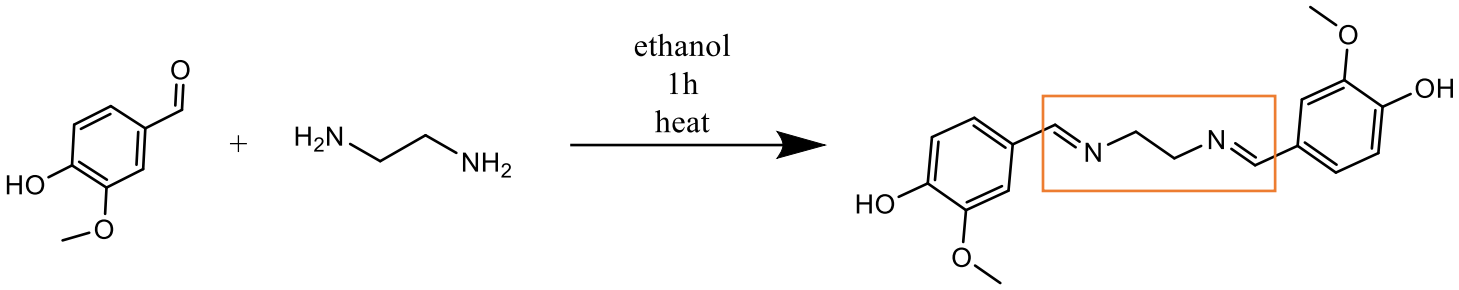

Figure 21 Reaction scheme for Ligand 1

4.1.1.1 *Geometry optimization*

The main focused for the geometry optimization part would be on the different conformers that can arise upon orientation changes of the bonds C=N-CH_2-CH_2-N=C observed in the orange box of the previous picture. This can be better visualized in a Newman projection in which the conformation of the carbons (-CH_2-CH_2-) is maintained, and the two carbons are the main axis for the visualization as seen in Figure 22.

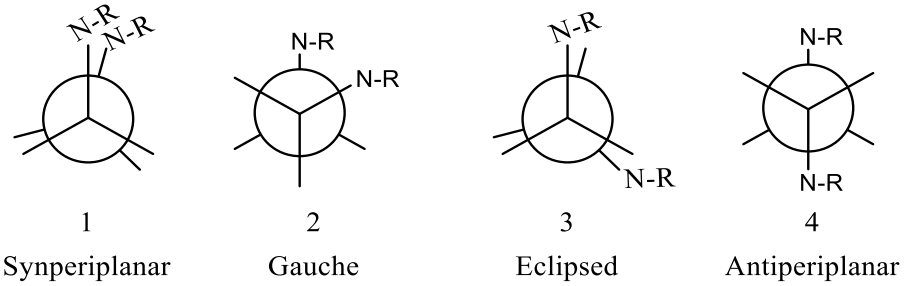

Figure 22 Conformers analyzed for the geometry optimization of L1

Furthermore, another important aspect is whether both aromatic rings have the same orientation, in other words, whether -OCH_3 of both rings point in the same direction since this can facilitate/complicate the possibility of π interaction. Other conformations were assessed but all end up converging to one of the previously described ones. The compounds are name for its starting geometry. Conformers were named using a letter (A or B), A when the substituents of the aromatic rings are in opposite direction and B if they are in the same direction. Also, a number was used to describe the Newman conformation, as seen in Figure 22, (for example conformer **L11A**'s starting conformation was synperiplanar with rings in same orientation). The result of the optimization for the proposed eight different conformers can be observed in Figure 23 .

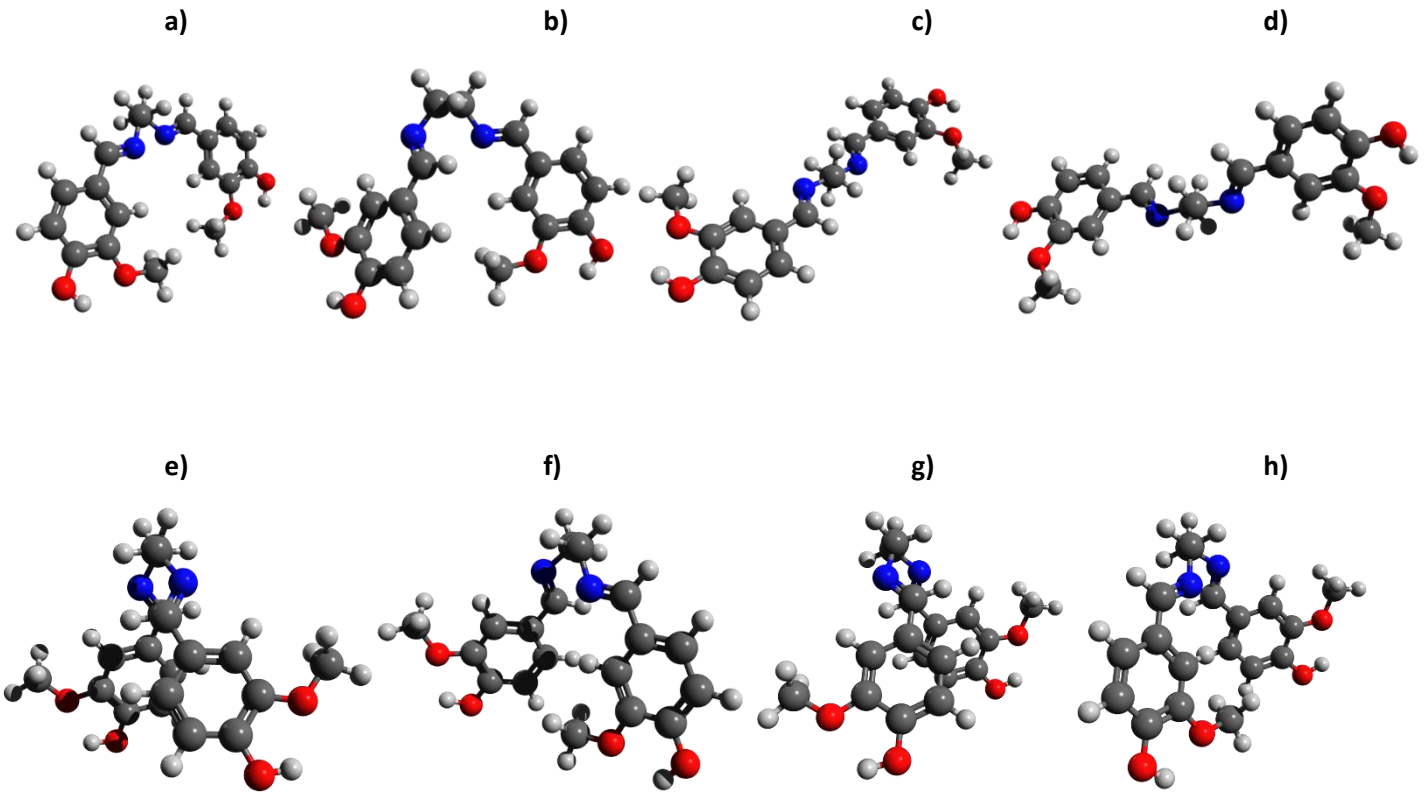

Figure 23 Conformers of L1: a) L12A b) L12B c) L14A d) L14B e) L11A f) L11B g) L13A h) L13B

In general, two conformers are found at the end of convergence in all the cases, gauche and antiperiplanar. It is important to analyze that the only ones that are in antiperiplanar conformation are the ones that started in it. Meanwhile, synplanar and eclipsed shift to gauche conformation although eclipse was equally distant to shift to gauche or antiperiplanar. Usually, it is expected that the antiperiplanar conformation is the most stable one, nevertheless, that is not the case for this ligand. The reason must be related with π…π interaction between aromatic rings. The final energy of the different conformations can be observed in Table 2. In general, the energy difference between the conformers is not so significant, being in most cases around 5 kJ/mol from the most stable one. The most stable conformation would be used for the further calculations.

Table 2 Energy of the conformers for L1

	Energy (E_h)	Energy (kJ/mol)	Difference (kJ/mol)		Energy (E_h)	Energy (kJ/mol)	Difference (kJ/mol)
L11A	-1108.267	-2909755.860	0.000	L12B	-1108.265	-2909750.624	5.237
L13A	-1108.267	-2909755.815	0.045	L13B	-1108.265	-2909750.572	5.289
L11B	-1108.265	-2909750.959	4.902	L14A	-1108.265	-2909749.889	5.971
L14B	-1108.265	-2909750.644	5.216	L12A	-1108.263	-2909745.369	10.491

4.1.2 IR of L1

As a general description for, in all this work, the assignation of the bands was made in two ways. First, the result from theoretical calculation was observed using the program *Gabedit*, based on the movement of the molecule for a specific corresponding computational predicted band, the assignation was made. Second, the assignation was check regarding bibliography when available to assure that the assignation was correct, in other words, that the band is between the expected range for the given assignation.

The experimental IR spectrum and computational signals for **L1** are indicated in Table 3. In the experimental IR is observed a defined peak for -OH stretching at 3449.6 cm^{-1} , the range of this band is between 3800 and 3000 cm^{-1} [119]. Furthermore, many peaks are observed in the range of 3000-2800 cm^{-1} due to C-H stretching of aliphatic carbons as expected [120]. A peak is observed at 1653 cm^{-1} assigned to the stretching of C=N which confirms the condensation of the Schiff Base. The usual range of 1690-1640 cm^{-1} [120]. Then, the C=C stretching peaks that usual present as a pair of bands one near 1600 cm^{-1} and the other 1475 cm^{-1} [120], in our case these bands were observed at 1589.7 and 1507.7 cm^{-1}.

Table 3 Summary results for FTIR of L1

IR bands for L1		
Assignation	**Experimental wavenumber [cm^{-1}]**	**Theoretical wavenumber [cm^{-1}]**
-OH	3449.6	-
-C=N	1653	1637.09
-C=C	1589.7, 1507.7	1589.65, 1582.30, 1491.45,1490.46
-CH_3 bending	1459.2	1455.48, 1455.05
C-C stretching of bridge	864.74	852.92
Bending CH_2	1194.6	1199.12
Bending C-H of the bridge	959.78, 916.92	953.60, 892.3
C-N	1019.4	1028.99
C-O bending	1421.9	1414.52
Out of plane	864.74, 828.65, 823.74	865.82
-OH of H out of plane	495.73	487.89

The peak at 1326.9 cm^{-1} was computationally confirmed to be the bending of the hydrogens of -CH_2-CH_2- bridge between the aromatic rings. The bending of C-O for -OCH_3 and -OH is observed at 1421.9 cm^{-1}. However, a peak cannot be assigned to C-N, computational calculations show a peak for this stretching, but its intensity is very low which confirms why it is not easily observed experimentally. Finally, the out of plane bending of aromatic hydrogens are observed around ~800 cm^{-1} consisted with literature [120]. There is significant agreement between the experimental and simulated spectra as can be observed in Figure 24.

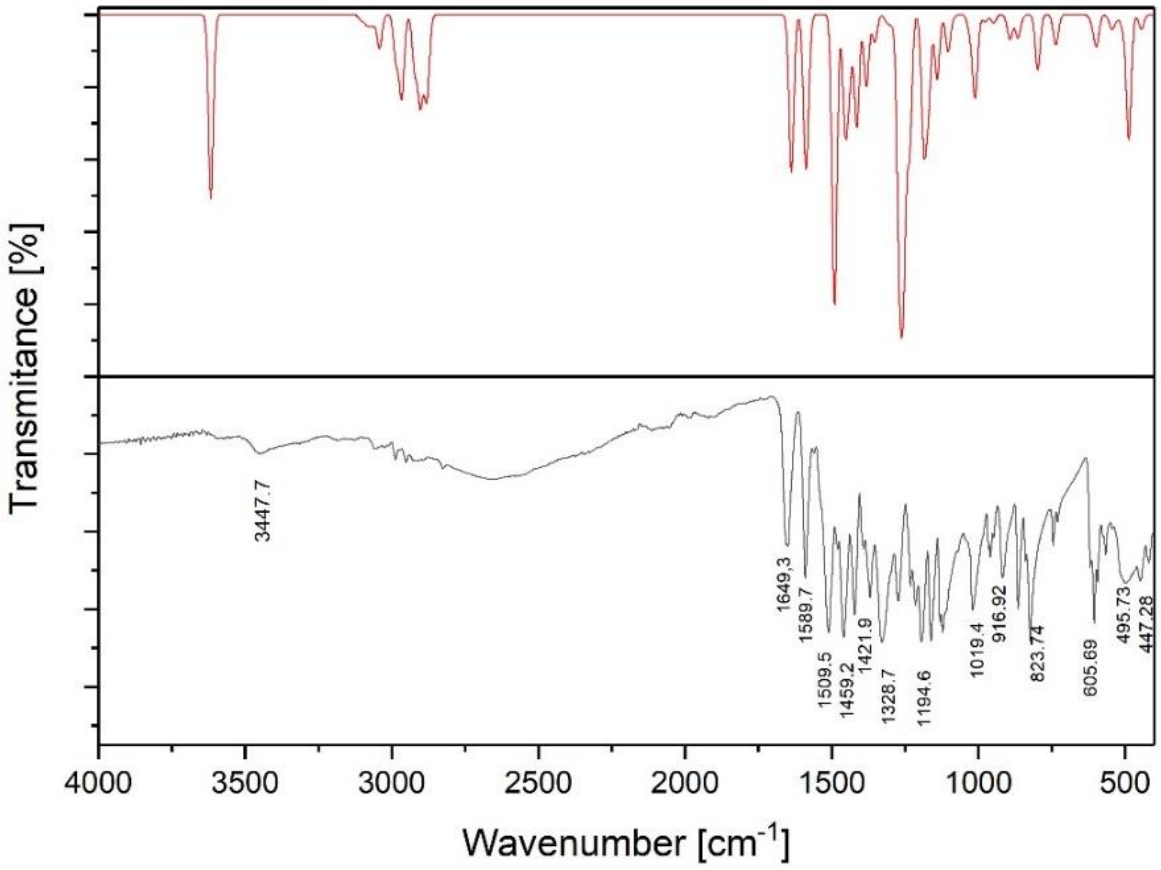

Figure 24 IR for L1, red for simulation and black for experimental result

4.1.3 UV-Vis of L1

The UV-Vis of this ligand was measured in acetonitrile solvent; therefore, acetonitrile was used for the CPCM parameter for calculations with TDDFT. The experimental and computational results can be observed in Figure 25 and Table 4. The obtained experimental spectrum is consistent

with the previously reported one with small shift due to the difference in solvent used for the measurements confirming correct synthesis[115]. For this ligand, four main peaks are observed with transitions $\pi \rightarrow \pi^*$ and $n \rightarrow \pi^*$ as observed in Figure 25.

To begin with, two peaks very close in energy are observed near ~ 400 nm, these have been related with transitions involving azomethine (-CH=N-) group as has been previously reported for many other different Schiff Bases[121,122], each peak relate to one of the azomethine group in the ligand. Indeed, based on the study of Gonciarz *et al.* with Salicylaldimines, these peaks should be related to a $n \rightarrow \pi^*$ transition of the free electron of nitrogen in the C=N bond to an excited state [123]. Moreover, in this work it is discussed that the $n \rightarrow \pi^*$ transition shows hypochromic effect depending on the polarity of the solvent, showing the highest molar extinction in ethanol and a much lower one for acetonitrile[123].

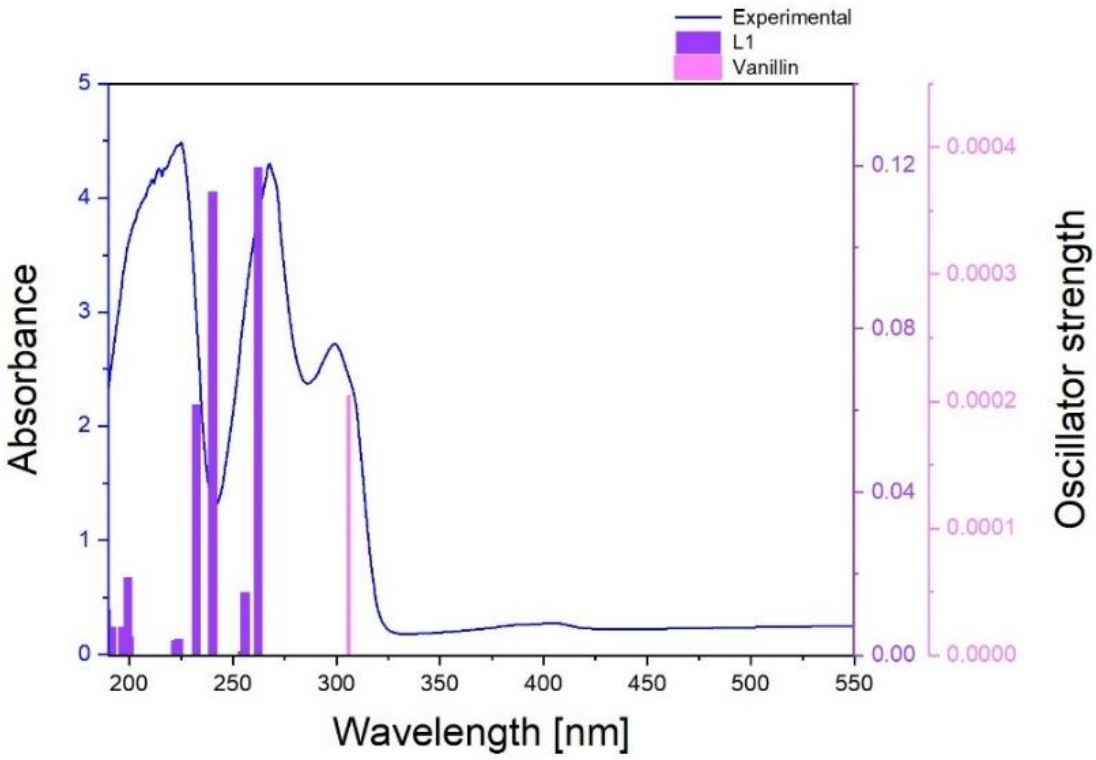

Figure 25 UV-Vis results for L1

In this sense, although CPCM was used to account for solvent effect, it is possible that it has not been enough to emulate the experimental conditions for this transition. An explicit approach may be required to truly represent this transition but implies much more computational time. Moreover, based on the same work discussed previously, the peak at 299 nm is most likely to be due to the π

→ π^* transition that involves azomethine group of **L1** [123]. Other possible contribution to this observed peak is due to the presence of residual vanillin, that present a transition at 306 nm, being a n → π^* transition involving orbital HOMO that is found around the aldehyde group to LUMO that is distribute in the whole vanillin.

Actually, it has been discussed that CAM-B3LYP tends to give results with shorter wavelengths for Schiff bases compare with other methods and experimental results. Moreover, when observe, these transitions tend to have small oscillator strength[124]. For example, as study by Vitnik *et al.*, the calculated (CAM-B3LYP) and experimental λ_{max} of aryl dyes differ by about 50 nm [125] which could affect our obtained result and explain the no occurrence of a peak at 299 nm in the calculated spectrum.

Table 4 UV-Vis data for L1

Experimental [nm]	Theoretical [nm]	Contribution	Assignment
404	-	Azomethine (-CH=N-)	n→ π^*
389			
299	306 (vanillin)	HOMO-2 → LUMO 90.87%	n→ π^*
268	262.2 (1)	HOMO → LUMO 51.77%	π → π^*
		HOMO-1→LUMO+1 24.22%	π → π^*
	255.9(2)	HOMO-4 → LUMO 21.44 %	n → π^*
		HOMO-1→LUMO 25.82%	n→ π^*
225	240.3 (5)	HOMO-3 → LUMO+1 19.40%	π → π^*
		HOMO-2→LUMO 31.22%	π → π^*
	232.2 (6)	HOMO-3 → LUMO 22.12%	π → π^*
		HOMO-1→LUMO 22.30%	π → π^*
214	199.5 (10)	HOMO-2 → LUMO 38.28%	π → π^*
		HOMO → LUMO+2 26.42%	π → π^*

The rest of the peaks are well represented by theoretical simulations. The peak at 268 nm has two theoretical contribution. The contribution of 262.2 nm due to transition between orbitals located on the rings and C=N to orbitals distributed over the whole molecule. Meanwhile, the transition at 255.9 nm corresponds to the transfer of lonely pair electron from the nitrogen of C=N to orbitals distributed in the whole ligand. The rest of transitions are π → π^* in which the transition involves HOMOs orbital mainly located in vanillin ring and azomethine C=N that transfer to π^* orbitals.

4.1.4 Biological activity of L1

4.1.4.1 *Geometry changes upon reduction of L1*

There are some important expected changes upon the reduction of the ligand during the SOD redox process that are exemplify in Figure 26. To begin with, the dihedral angles of N-CH_2-CH_2-N in the singlet state is 68.3 ° and upon reduction it decreases to 51.4 ° making the rings face each other closer and in an almost perfect parallel manner. In fact, the rings are as close to each other as possible based on van der Waals radius of the carbons, the distance between centroids is 3.91 Å which join with the angle between the rings being ~ 16 Å can be consider as a π-π interaction[126]. The C_1=N_1 bond increases in size upon reduction (shown with red arrow) from 1.26 Å to 1.33 Å, meanwhile, the other C=N bond is mostly unchanged.

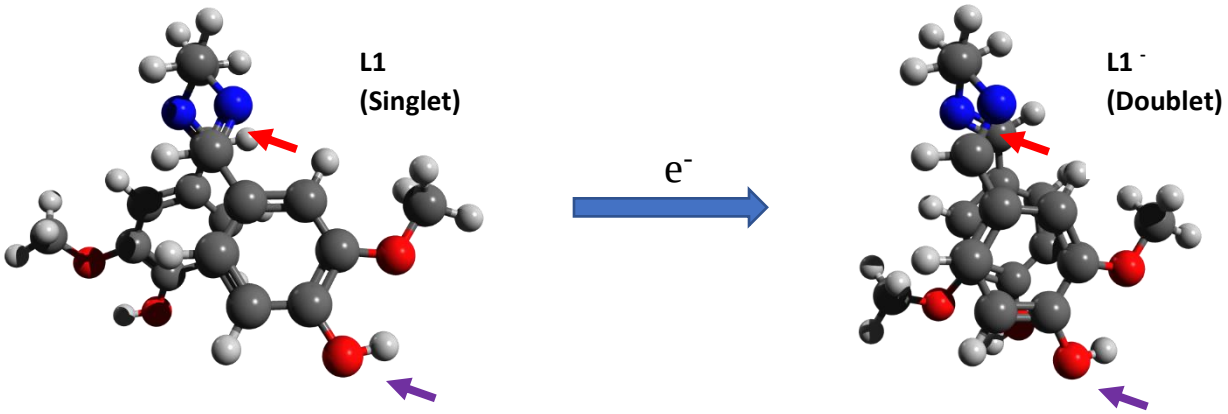

Figure 26 Geometry changes upon reduction of L1

Moreover, the bond distance between the groups -CH_2 in the bridge increases upon reduction from 1.529 Å to 1.552 Å. Finally, upon reduction, the orientation of -OH shifts slightly no longer in plane with -OCH_3. The rest of bonds and angles are maintained almost unchanged.

4.1.4.2 *Electron Affinity for L1*

Using the energy of the neutral and reduced ligand, the electron affinity was calculated, and its results can be observed in Table 5. The comparison with the rest of ligands would be done at the end of the chapter.

Table 5 Electron Affinity for L1

	Energy Singlet L1 [E_h]	**Energy Doublet L1 [E_h]**	**EA [E_h]**	**EA [kJ/mol]**
L1	-1108.267	-1108.328	-0.061	-159.345

4.1.4.3 *Orbitals analysis for L1*

Analysis of frontier molecular orbitals is important to understand the reactivity of the molecule, the respective obtained values for the frontier orbitals' energies and reactive parameters are shown in Table 6. As expected from the significant changes in geometry upon reduction observed mainly in one side of the ligand, the SOMO of the doublet state, where the extra electron is located upon reduction, is more distributed in just one of the rings (the one connected to the C=N group that changed bond size). As well, the only oxygen that contributes to the electronic density corresponds to the -OH in this same ring. On the other hand, the LUMO of the singlet is located over the whole molecule excluding the $-OCH_3$. The calculated orbitals and its changes upon reduction are observed in Figure 27.

Table 6 Reactivity parameters for L1

Doublet $L1^-$						**Singlet L1**					
SOMO [eV]	**LUMO [eV]**	**Band gap [eV]**	**η [eV]**	**μ [eV]**	**ω [eV]**	**HOMO [eV]**	**LUMO [eV]**	**Band gap [eV]**	**η [eV]**	**μ [eV]**	**ω [eV]**
-7.344	-0.143	7.201	3.601	-3.744	1.946	-3.322	0.342	3.664	1.832	-1.490	0.606

Looking at these facts, it can be concluded that although initially the LUMO of singlet ligand indicates that the whole molecule is likely to distribute the extra charge density, upon the addition of the electron one side of the molecule is preferred for the redistribution of this extra electronic density as observed in Figure 27. Maybe, this is caused due to there is not complete resonance among the rings due to $-CH_2-CH_2-$ bridge. Moreover, it is probable that the molecule changes the orientation of the rings to allow the transfer of a small portion of this density through π stacking to the other ring.

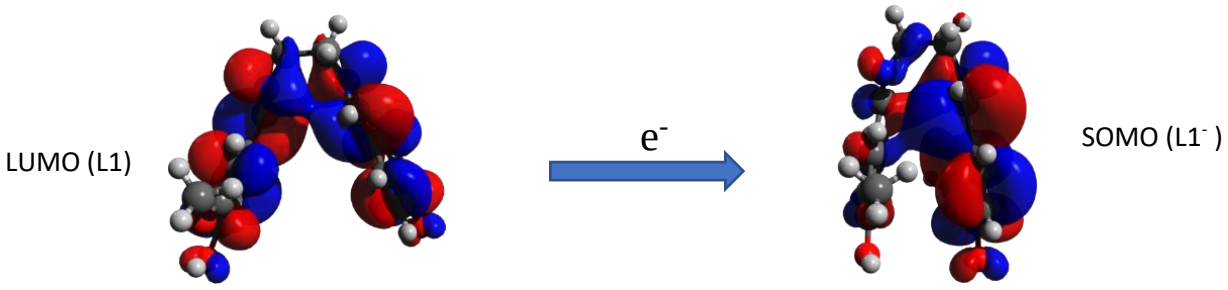

Figure 27 Orbitals involve in the reduction of L1

4.2 Complexes with L1

Two different complexes of copper were obtained using **L1**, which just differ in their ratio of metal:ligand used during the synthesis for **Cu1A**, the ratio was 1:1 and for **Cu1B** 1:2.

4.2.1 General description of the complexes

4.2.1.1 *General description for Complex Cu1A*

The resulting complex obtained experimentally is observed in Figure 28 which had a yield of 66.97 % being insoluble in ethanol and slightly soluble in acetonitrile. Regarding the magnetic properties, it has a μ_{eff} =1.92 BM which suggest that copper is in a 2+ state.

Figure 28 Obtained Complex C1A

4.2.1.2 *General description Complex Cu1B*

The complex obtained experimentally showed purple color as seen in Figure 29 which had a yield of 67.71%. This complex is soluble in ethanol and methanol, and slightly soluble in acetonitrile. The magnetic measurements showed that this compound has μ_{eff} = 1.94 BM indicating that copper is found in a 2+ state.

Figure 29 Complex C1B

4.2.2 Geometry optimization of complexes with L1

4.2.2.1 *Geometry optimization Cu1A*

Based on the previous studies of **L1**, it seems clear that the orientation of -OH and -OCH_3 is important, so different orientations were tested. Each conformer was tested for coordination through the nitrogen and through oxygens. The optimized different conformers are shown in Figure 30 and their corresponding energies are summarized in Table 7.

As seen in Table 7, in all the cases, the coordination is preferred through nitrogen, this result is expected based on hard-soft acid-base theory (HSAB). In general, there would be a preferential interaction between acids-bases with the same character[127], some cannot be strictly classified as neither but rather as borderlines between both behavior and characteristic[128].

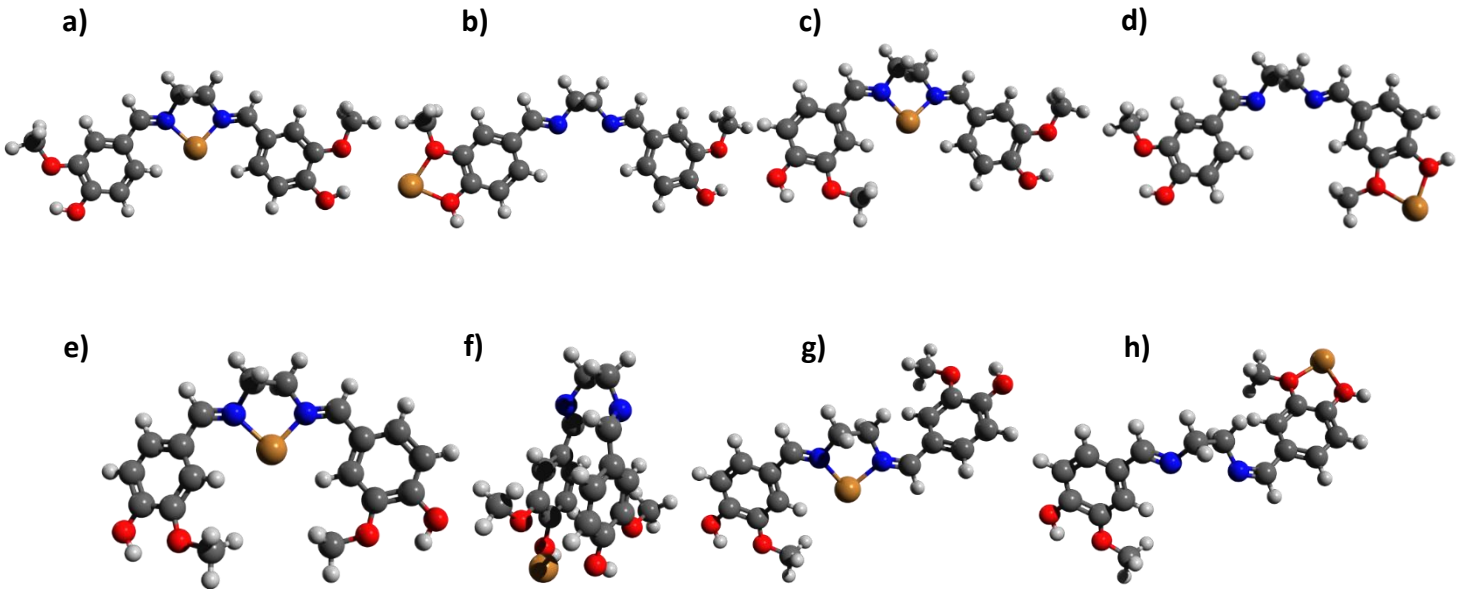

Figure 30 Initial conformers analyzed to determine geometry of Cu1A a) CL1N1 b) CL1O1 c) CL1N2 d) CL1O2 e) CL1N3 f) CL1O3 g) CL1N4 h) CL1O4

Table 7 Energy of conformers of complex Cu1A

Conformer	Energy (E_h)	Energy (kJ/mol)	Difference (kJ/mol)	Conformer	Energy (E_h)	Energy (kJ/mol)	Difference (kJ/mol)
CL1N1	-2748.567	-7216362.107	0.000	CL1O2	-2748.525	-7216251.263	110.844
CL1N3	-2748.565	-7216356.777	5.330	CL1O3	-2748.524	-7216250.412	111.695
CL1N4	-2748.559	-7216341.498	20.609	CL1O1	-2748.524	-7216249.721	112.386
CL1N2	-2748.556	-7216334.452	27.654	CL1O4	-2748.514	-7216224.106	138.000

It is known that Cu^{2+} is a borderline acid, ROH/R-O-R are hard base, and R=N-R an intermediate base[129,130]. Therefore, a coordination through oxygens (R-O-R and R-OH) is not as favored for copper. In general, the orientation/geometry of the ligand is maintained whether the copper coordinates through nitrogen or oxygen. Among the conformer coordinated through nitrogen, the orientation of -OH and $-OCH_3$ significantly affects the energy probably because the orientation of this substituents influences the geometry aspects of the bridge directly affecting the coordination sphere and metal geometry. The most stable conformer would be used for the further calculations.

Finally, the coordination sphere was completed with water molecules, different approaches were taken. For the first proposal (**Cu1A1**), the copper coordinates with two waters generating a distorted tetrahedral geometry. Later, the optimization was tried with four water, but one of them was pushed away from the coordination sphere due to not enough available space (**Cu1A2**). Finally, the optimization was made with just three waters (**Cu1A3**). The optimized structures of these three conformations are shown in Figure 31. For both cases, a geometry of square base pyramid for the copper was obtained, the square base is formed by the three waters and one of the nitrogens. No energy comparation can be made in this case since the number of atoms is not equal. For the rest of calculations, **Cu1A1** would be used as it showed a better result for the theoretical UV-Vis which would be discussed later.

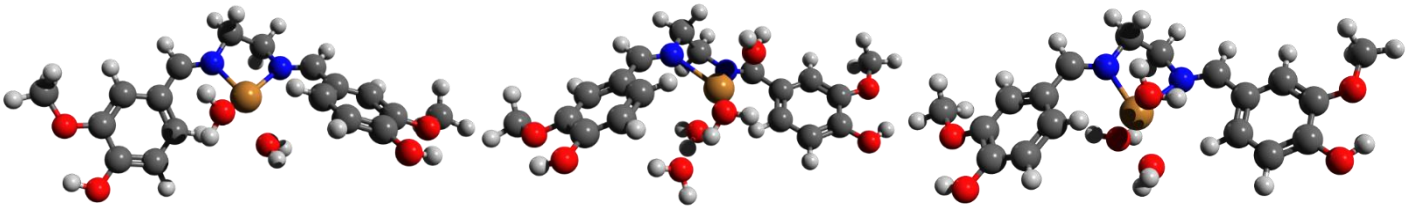

Figure 31 Conformers of Cu1A, from left to right: Cu1A1, Cu1A2 and Cu1A3.

4.2.2.2 *Geometry optimization for Cu1B*

For the optimization of this complex, there are not many possible conformers, in total six conformers were proposed as can be observed in Figure 32. Moreover, water molecules were added for each of the possible conformer but in most of the cases there was not enough space ending up out of the coordination sphere. The energies for the different conformers are shown in Table 8. The difference in energy observed can be caused by many factors such as π…π interaction between the aromatic rings, different levels of torsion on the bridge, and orientation of the rings and its

substituents within the aromatic ring important effect as observed in ligand the (especially for **Cu1B3w** and **Cu1B3**).

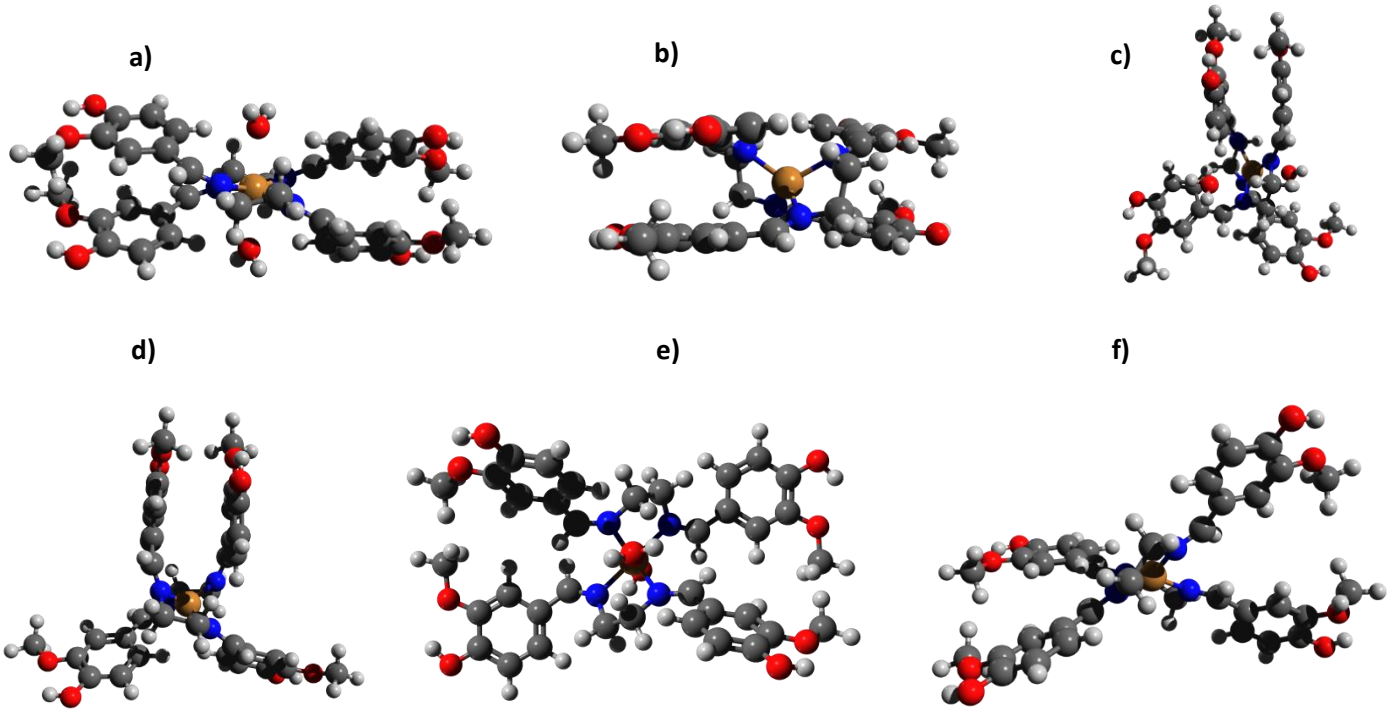

Figure 32 Different tested geometries for complex a) Cu1B1w b) Cu1B1 c) Cu1B2w d) Cu1B2 e) Cu1BCu1B3w f) Cu1B3

Table 8 Energy of conformers for CuB1

Conformer	Energy [E_h]	Energy [kJ/mol]	Difference [kJ/mol]	Conformer	Energy [E_h]	Energy [kJ/mol]	Difference [kJ/mol]
Cu1B1w	-4006.987	-10520343.851	0.000	Cu1B1	-3854.260	-10119359.028	0.000
Cu1B2w	-4006.972	-10520305.127	38.724	Cu1B2	-3854.255	-10119345.544	13.484
Cu1B3w	-4006.949	-10520244.168	99.684	Cu1B3	-3854.230	-10119279.771	79.256

4.2.3 IR analysis for complexes with L1

4.2.3.1 *IR Cu1A*

To continue with the characterization of the complex, the IR analysis was performed, the experimental and computational results and assignation are shown in Table 9 and its spectrum is depicted in Figure 33. A broad band is observed expanded around 3000 cm^{-1} related with -OH stretching in the aromatic ring. The peaks observed above 3000 cm^{-1} are related with stretching of aromatic C-H or C-O, the possibility of being N-H peaks is unlikely since the position (wavenumber) are not consistent with the ones obtained IR for the reactive ethylenediamine. The

peaks for stretching of C-H from -CH_2 are overlapping by the -OH band. The small peak observed at 1664.2 cm^{-1} could be assigned to the C=N which usually presents in the range 1690-1640 cm^{-1} [120], more likely antisymmetric, stretching which intensity was affected by the coordination through nitrogen. As can be seen, this band possesses a small shoulder suggested than each C=N bond has a stretching slightly different. Meanwhile, the symmetric stretching C=N seem to have been greatly shifted to lower wavenumber and is fused with the stretching of C=C bond, so the peak at 1582.2 cm^{-1} has been assigned to both stretching. The loss of intensity of C=N bands upon coordination or that the peak is covered by others is not uncommon result an have been appreciated in other studies[131]. Multiple peaks are assigned to bending and stretching of C-O from -OH and -OCH_3 summarize in Table 9. Finally, the coordination is confirmed with the appearance of new peaks at 594.51 cm^{-1} and 421.18 cm^{-1} for Cu-O bonds, and for Cu-N bond at 437.96 cm^{-1} consistent with expected IR values [119].

Table 9 IR results for Cu1A

IR bands for Cu1A			
Assignation	**Experimental wavenumbers [cm^{-1}]**	**Assignation**	**Experimental wavenumbers [cm^{-1}]**
C=N	1664.2	C-N stretching	1058.5
C=C	1582.2, 1507.7	Bending of H of HC=N	957.92
C-O stretching	1278.4	M-O	594.51, 421.18
Bending C-H of bridge HC=N-CH2-CH2-N=CH	1321.3	Bending H of -OH out of plane	534.87
C-O bending	1387.4 , 1179.7	M-N	437.96

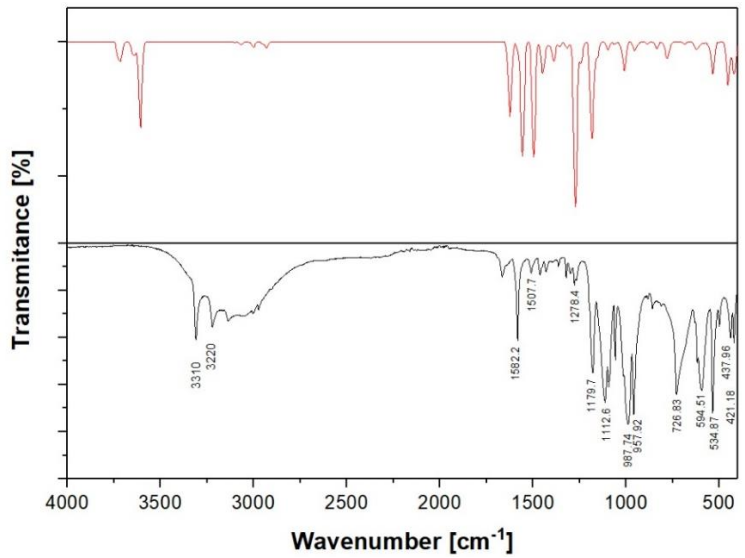

Figure 33 IR for Cu1A in red DFT simulation and in black experimental result.

The simulated spectrum shows a strong band ~1250 cm^{-1} that is shifted in respect to experimental results. The relative orientation of -OCH_3 and -OH plays an essential role in stability as discussed previously, it is plausible the shift in the peak observed is due to some different orientation of the aromatic substituents different from the ones proposed here. Nevertheless, in general the structure should be similar as the one proposed here because the rest of the experimental peaks can be relate with experimental results, and the UV-Vis is consistent.

4.2.3.2 *IR for Cu1B*

First, the IR spectrum of **Cu1B** is very different with respect to the previous one although the ligand and metal used are equal just the ratio changes as can be clearly observed in Figure 34. These changes are related with significant change in orientation of the ligands and coordination mode.

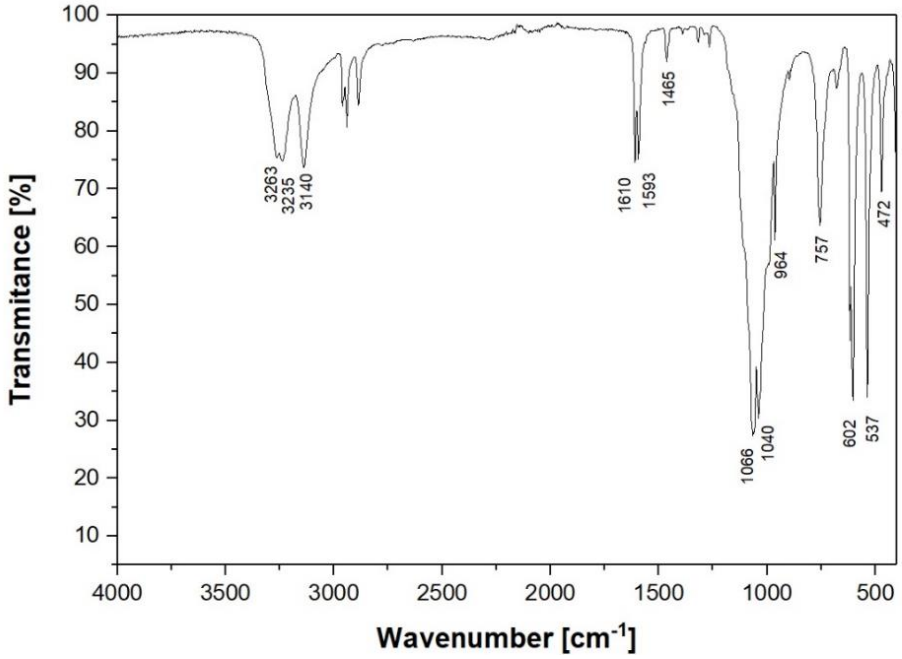

Figure 34 Experimental IR result for Cu1B

The peaks between 3200 cm^{-1} and 3000 cm^{-1} are due to stretching of aromatic C-H and C-O, and the ones between 3000 and 2800 cm^{-1} are due to the stretching -CH of -CH_2. Here, the peaks of C=N and C=C are very close to each other with just 17 cm^{-1} of shift, which suggest that our previous assumption of fused peaks is plausible. Moreover, the more prominent peaks are observed around ~1000 cm^{-1} due to C-N stretching mode, probably one peak for each ligand, this further

suggests a coordination through nitrogen. Finally, the coordination is confirmed by the appearance of strong peaks at 602 and 537 cm^{-1} for Cu-N and 472 cm^{-1} for Cu-O.

4.2.4 UV-Vis for copper complexes with L1

4.2.4.1 *UV-Vis for Cu1A*

The measurement of this UV-Vis was made using acetonitrile, this was used as solvent parameter for CPCM. The comparison between experimental and computational simulations are shown in Figure 35. The theoretical assignation was made based in the transitions calculated and using Avogadro which is summarized in Table 10. The three computational peaks of lower energy are related with d-d transitions. Experimentally, these are not easily observed as the solution was very diluted. These d-d transitions are from copper orbitals d_z^2 and d_{yz} orbitals to d_{xz} orbital of the metal. Regarding the peak at 500 nm, the best transition computationally observed is slightly far from the experimental observed peak. However, a transition at 502 nm exhibits a weak oscillator strength. Both peaks have similar transition (orbitals involves and energies), the oscillator strength is very sensible even to small changes which may have cause a decrease in strength for the peak at 502 nm. Finally, the rest of the peaks are assigned as charge transfer in which α and β orbitals are involved. The orbitals involved are mainly located in the rings, bridge connecting the rings and ligand waters.

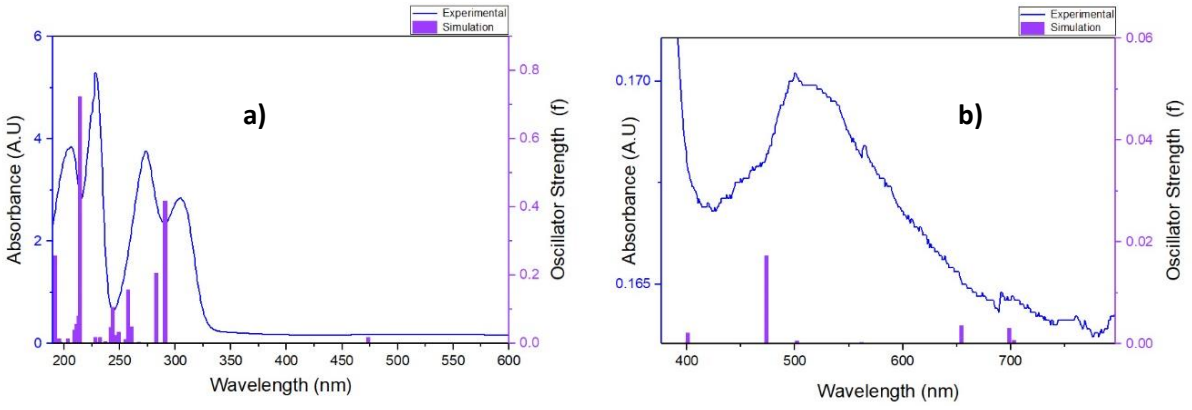

Figure 35 UV-Vis measurement for Cu1A a) whole spectrum b) zoom in the d-d transfer area

Table 10 UV-Vis analysis for Cu1A

Experimental λ [nm]	Theoretical λ [nm]	Contribution	Assignation
692	698.7	HOMO-20 (β) → HOMO (β) 19.96%	d-d
		HOMO-1 (β) → HOMO (β) 21.02%	d-d
	654.2	HOMO-7 (β) → HOMO (β) 26.33%	d-d
		HOMO-22 (β) → HOMO (β) 28.76%	d-d
500	502	HOMO-26 (β) → HOMO (β) 27.42%	d-d
		HOMO-22 (β) → HOMO (β) 17.24%	d-d
	473.5	HOMO-1 (β) → HOMO (β) 68.23%	d-d
304	290.8	HOMO-1 (β) → LUMO (β) 29.25%	LMCT
		HOMO (α) → LUMO (α) 27.64%	LMCT
273	282.2	HOMO-2 (β) → LUMO (β) 25.74%	LMCT
		HOMO-1 (α) → LUMO (α) 25.25%	LMCT
229	214.1	HOMO-1 (β) → LUMO +3 (β) 12.51%	ILCT
		HOMO (α) → LUMO+3 (α) 12.18%	ILCT
206	192	HOMO-1 (β) → LUMO +5 (β) 10.71%	ILCT
		HOMO (α) → LUMO+5 (α) 10.68%	ILCT

4.2.4.2 *UV-Vis Cu1B*

The experimental procedure allowed in this case to measure the UV-Vis in the range 175 - 1200 nm and the obtained experimental and theoretical result is observed in Figure 36, the peak maximums and its corresponding assignation is observed in Table 11. The transitions observed between 500 and 1200 nm are assigned to d-d transitions from different HOMO-X (β) to HOMO (β) orbitals. The HOMO orbital is just located in the $d_{x^2-y^2}$ and the lone pairs of electrons in nitrogen. Meanwhile, the HOMO-X (β) orbitals include different d orbitals of metals, specified in Table 11. The transitions observed below 500 are assigned to LMCT/MLCT/ILCT in which α and β orbitals participate.

Table 11 UV-Vis data for Cu1B

Experimental λ [nm]	Theoretical λ [nm]	Contribution	Assignation
1068	1071.7 (1)	HOMO-11 (β) → HOMO (β) 56.43%	d_{z^2} → $d_{x^2-y^2}$
		HOMO-9 (β) → HOMO (β) 19.12%	d_{z^2} → $d_{x^2-y^2}$
	725.9 (2)	HOMO-36 (β) → HOMO (β) 51.91%	d_{yz} → $d_{x^2-y^2}$
		HOMO-12 (β) → HOMO (β) 18.93%	d_{yz} → $d_{x^2-y^2}$
692			
	708.6 (3)	HOMO-35 (β) → HOMO (β) 51.35%	d_{xz} → $d_{x^2-y^2}$
		HOMO-10 (β) → HOMO (β) 22.11%	d_{xz} → $d_{x^2-y^2}$
558	588.4	HOMO-42 (β) → HOMO (β) 22.55%	d_{xy} → $d_{x^2-y^2}$
		HOMO-39 (β) → HOMO (β) 59.52%	d_{z^2} → $d_{x^2-y^2}$
371	409.7 (7)	HOMO-1 (β) → HOMO (β) 19.57%	LMCT
	391.9 (11)	HOMO-1 (β) → HOMO (β) 62.41%	LMCT
309	290.2 (23)	HOMO-1 (β) → LUMO (β) 20.77%	ILCT
		HOMO (α) → LUMO (α) 18.03%	ILCT
279	273.5 (28)	HOMO-12 (β) → HOMO (β) 27.52%	LMCT
		HOMO-14 (β) → HOMO (β) 14.01%	LMCT
230	242.2 (53)	HOMO-13 (β) → HOMO (β) 16.50%	LMCT
	224 (66)	HOMO-7 (α) → LUMO+2 (α) 15.74%	ILCT
		HOMO-4 (α) → LUMO (α) 18.59%	ILCT

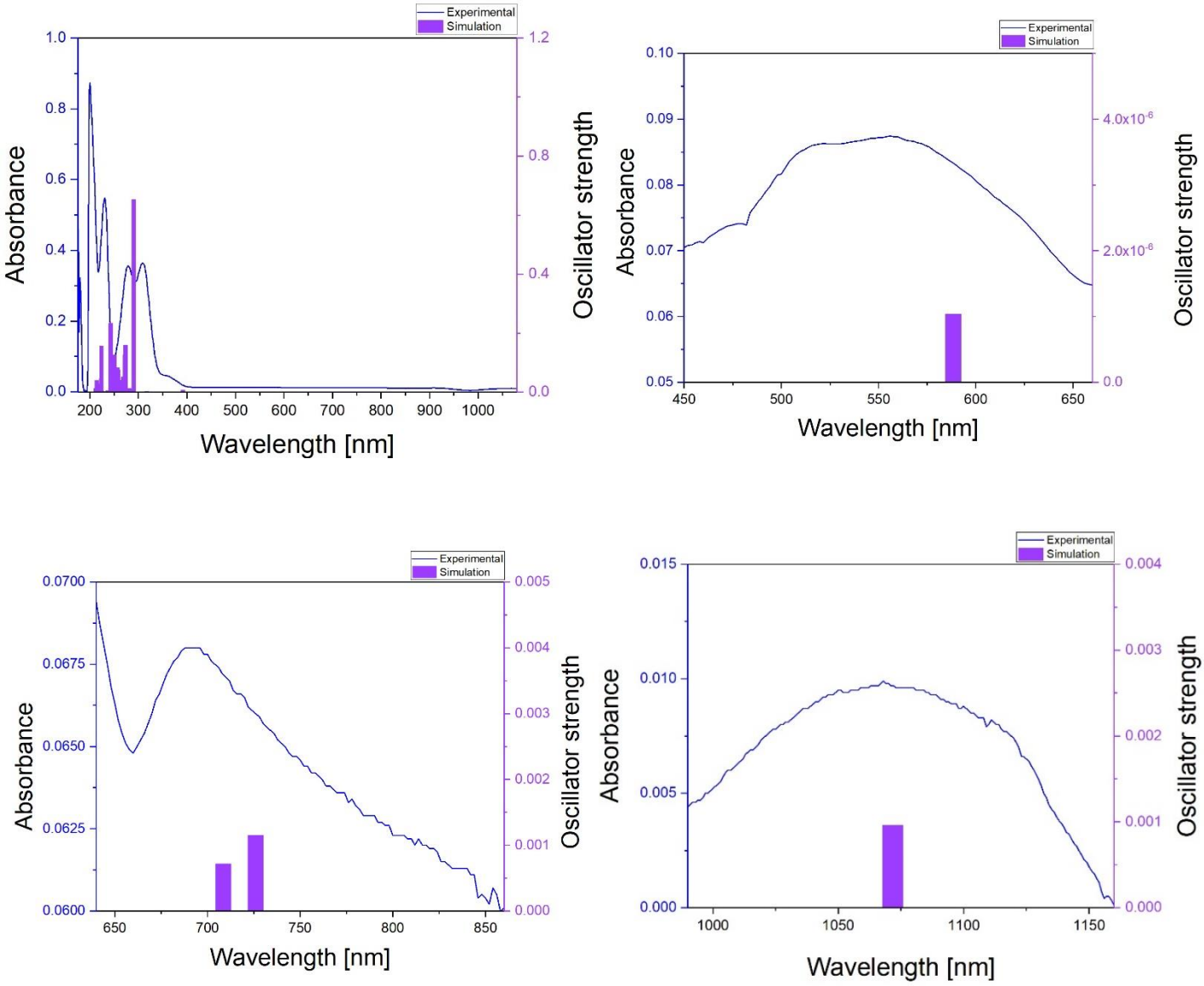

Figure 36 UV-Vis results for complex Cu1B left side complete spectrum and right zoom for d-d transitions of lower energy

Relative to the complex **Cu1A**, the d-d transitions are red shifted to higher wavelengths. As can be observed in this geometry, there is the addition of two new nitrogen donors in the coordination sphere, which provokes a change in geometry similar to an octahedral one. Although octahedral, the equatorial bonds form a tetrahedral perturbated square planar geometry as the oxygen in axial positions are further away causing Jahn Teller effect. The position of d-d transitions is consisted with UV-Vis analysis for previous discussions for copper complexes for this geometry[132].

4.2.5 Diffuse reflectance for complexes with L1

4.2.5.1 *Diffuse reflectance for Cu1A*

As can be seen in Figure 37, there is almost no shift between the peaks observed in the solid and liquid state, so there is no exchange of water/ethanol by acetonitrile. However, it is important to point out that in a same band, two peaks are observed. One at 498 nm and another at 469 nm, the second being like a shoulder that can be distinguished in solid state but not in the liquid one. It is interesting to notice that there are 29 nm of distance between the two peaks of this band as observed with purple arrows in Figure 37. Interesting, almost the same difference (28.5 nm) is observed between the two calculated transitions assigned to this band at about 500 nm in liquid state (502 and 473.5 nm). This suggest that the calculations are valid, but the oscillator strength is very sensible to slight changes in geometry. The shift observed between solid and liquid state are due to some slight changes on the geometry of the complex upon dissolution.

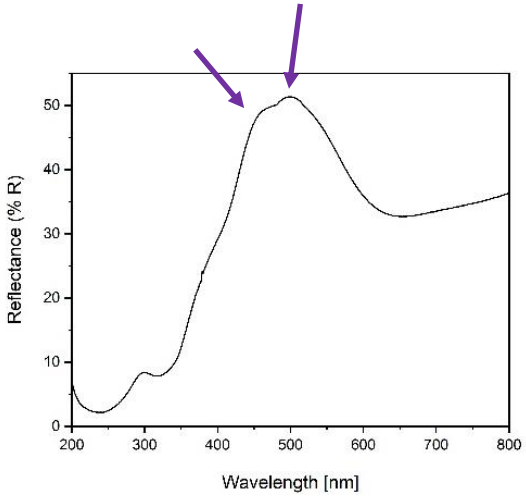

Figure 37 Diffuse Reflectance for Cu1A

4.2.5.2 *Diffuse reflectance for Cu1B*

The effect of solvent is more important for this complex, showing significant shift between the peaks in UV-Vis spectra in solid (Figure 38) and liquid state. The first peak is observed at 708 nm in liquid state whereas in solid state it is shifted to smaller wavelength, blue shifted, by ~16 nm. This transition involving orbitals with a z-component (d_z^2). The other d-d transitions are not easily identified in solid state. The peak at 447 nm has a red shifted of ~70 nm, and the peak at 318 nm is red shifted by ~28 nm. In general, d-d transitions have associated a blue shift, meanwhile, the charge transfers involve a red shifted. Moreover, the shift is higher in transitions involving the

lonely pairs of electrons as its stabilization is highly dependent on solvent polarity (transition at 447 nm involves nitrogen and oxygen lonely pairs).

It is possible that in solution, the solvent molecules disrupt the π..π interaction system affecting the orientation of the ligands, therefore changing the geometry around the copper atom. Moreover, the orientation of the waters/solvent in the axial position in solid state could be different than in the liquid one causing changes in Jahn Teller effect. In this sense, Roy, Mitra & Patra in 2011 [133] reported solid and liquid UV-Vis results for the copper complexes studied, upon the result obtained, it is stated that a reduction in the strength of bond in the axial position, the d-d bands cause by transitions involving orbital with a z-component will tend to shift to greatest energies[133].

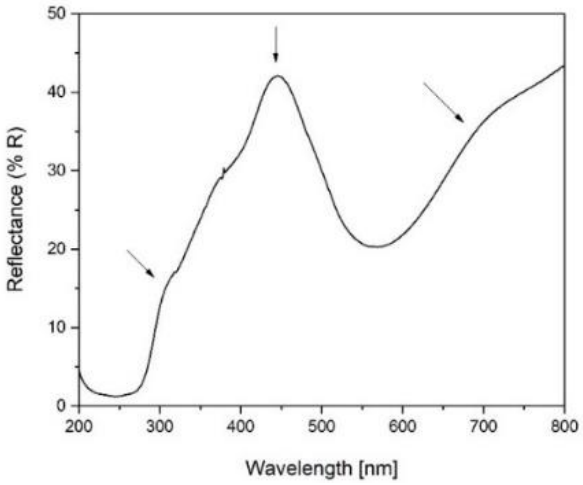

Figure 38 Diffuse Reflectance for Cu1B

4.2.6 Biological Activity of complexes with L1

4.2.6.1 *Biological analysis Cu1A*

4.2.6.1.1 Geometry changes upon redox process for Cu1A

The geometrical changes observed upon reduction of Cu1A are observed in Figure 39. As described in the introduction chapter, the τ parameter would be used to better describe the optimized geometry obtained in Orca for copper complexes. Due to the nature of the ligand, the two nitrogens have low freedom to move due to the bridge that joins them, therefore, the geometry of the complex would be mainly determined by the orientation of the water molecules. For the doublet state (Cu^{2+}), the parameter τ = 0.44 suggests a tetrahedral distorted square planar geometry in which the ligands donor atoms form a dihedral angle of 38.6°. It is complicated to determine the nature as the value τ is almost in between the values of the two coordination types. Moreover, the angles N-Cu-N and

O-Cu-O are equal to ~87 °, and the N-Cu-O/O-Cu-N angles are of two different kinds, ones ~100° and others ~148°. These values were obtained regarding the calculated optimized geometry of the complex.

After the reduction, there are some significant changes in the geometry of the complexes with Cu^{1+}. To begin with, the rings become more parallel to each other which makes the waters move to perpendicular positions in respect to the nitrogens. This provokes that the τ parameter changes to 0.79, suggesting a tetrahedral geometry. There are no major changes in the N-Cu-N and O-Cu-O angles, but the O-Cu-N ones all become ~ 120°. Furthermore, the N-Cu and O-Cu bonds slightly increase by ~0.1 Å and ~0.15 Å respectively, but C=N reduced by ~0.06 Å. It does not seem as neither of the bond would break upon reduction just slight elongation suggesting a weaker coordination.

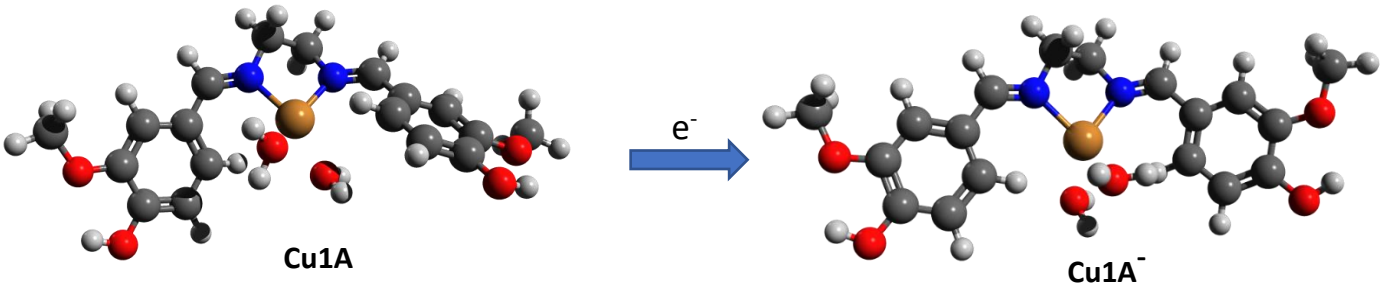

Figure 39 Geometry changes upon redox process in Cu1A

4.2.6.1.2 Electron affinity for Cu1A

The electron affinity for the complex as shown in Table 12 is about three times more negative that one for the ligand which suggest an improvement in SOD capacity upon coordination with the metal.

Table 12 Electronic Affinity for complex Cu1A

	Energy Singlet [eV]	Energy Doublet [eV]	EA [eV]	EA [kJ/mol]
Cu1A	-2901.73	-2901.54	-0.188	-494.32

4.2.6.1.3 Molecular Orbital involve in redox process of Cu1A

The results obtained using TDDFT were used to calculate reactivity parameters summarized in Table 13.Comparing with the ligands, the band gap in neutral state for **Cu1A** is smaller, meaning a

higher reactivity than the ligands. Moreover, ω is higher which implies that the complex is more attracted to electron rich entities such as superoxide anion.

Table 13 Reactivity parameters for Cu1A

HOMO [eV]	LUMO [eV]	Band gap [eV]	η [eV]	μ [eV]	ω [eV]	HOMO [eV]	LUMO [eV]	Band gap [eV]	η [eV]	μ [eV]	ω [eV]
Doublet						**Singlet**					
-7.965	-1.318	6.647	3.324	-4.642	3.241	-7.184	-0.634	6.550	3.275	-3.909	2.333

The representation of the molecular orbitals SOMO **Cu1A** and HOMO **Cu1A**$^{-}$ are represent in Figure 40. Regarding the orbitals, the SOMO of Cu^{2+} would be the electron accepting orbital upon reduction and HOMO is the orbital in which the accepted electron would be place in the Cu^{1+} molecule. As observed in Figure 40, both are similar in electron distribution involving mainly C=N and Cu orbitals, the main difference is whether the water molecules are involved or not. In the doublet state, there is a contribution to the electronic density from the water molecules probably because their orbitals are aligned with the d_{xz} orbitals of copper, but in the singlet state the orientation of water molecules is not as favorable to interact with the d_{xz} orbital of copper.

SOMO (Cu^{2+}) **Cu1A** HOMO (Cu^{1+}) **Cu1A**$^{-}$

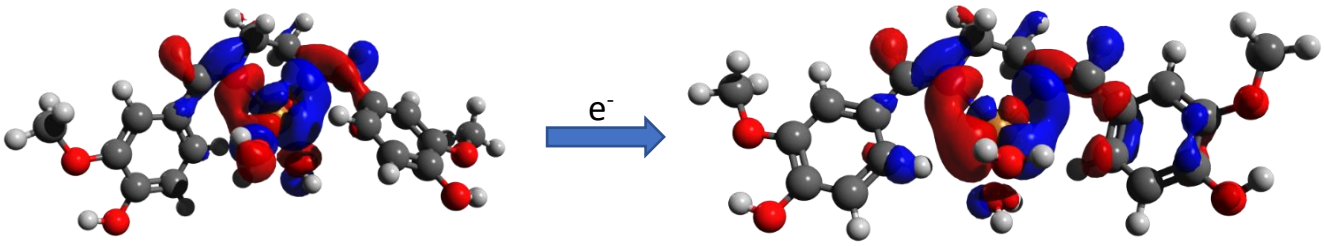

Figure 40 Orbitals involve in the reduction of Cu1A

4.2.6.2 *Biological analysis for Cu1B*

4.2.6.2.1 Geometry changes upon redox process of Cu1B

There are some significant changes between the geometry of the complex in its neutral and reduced state. To begin with, in its Cu^{2+} state, copper is in a distorted octahedral geometry. The bonds in axial position O-Cu are ~ 2.3 Å long, and the Cu-N bonds in the equatorial position are of ~2.1 Å. Based on these results, the complex shows Jahn-Teller effect. Regarding the angles, between ligands in the equatorial positions, two of them are 98.7° and the others 83.6°. Meanwhile, the

angles O-Cu-N, between axial and equatorial ligands, show values of ~ 98° or ~82°. Finally, the angle between the axial oxygens is 179.6°.

Upon reduction, two bonds separate considerably from the copper which suggest that they broke (dotted lines in Figure 41). For example, the Cu-O bond passes from 2.38 Å to 4.7 Å, and the C-N changes from 2.09 Å to 3.16 Å clearly indicating that there is a break in these bonds. Therefore, the geometry passes from distorted octahedral to distorted tetrahedral (τ=0.645). Also, there is a significant change in the orientation of the rings (purple arrow). All these changes imply significant amount of energy required for the reduction.

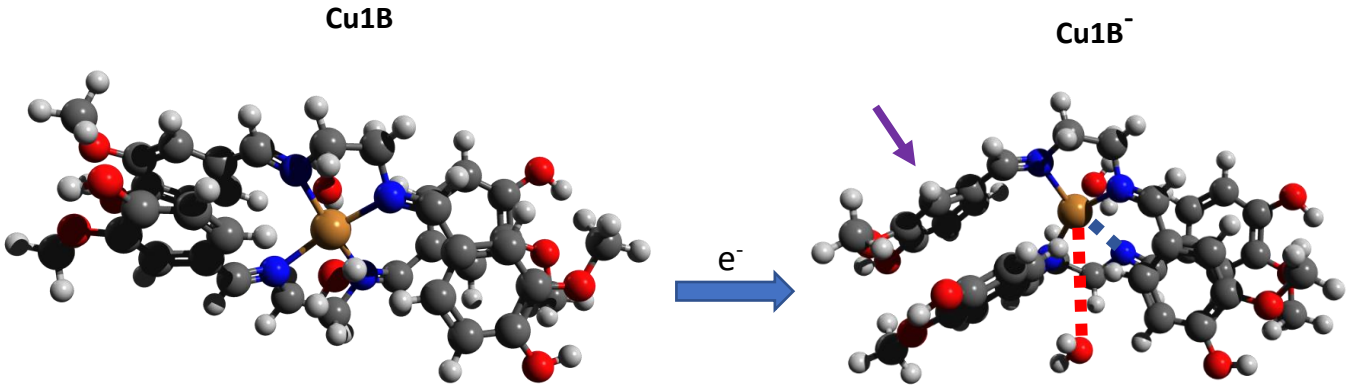

Figure 41 Geometry changes in reduction of Cu1B

4.2.6.2.2 Electron affinity Cu1B

The electron affinity of the **Cu1B** is much more negative than the one of the ligands as can be observed in Table 14. Nevertheless, it is not as negative as that by **Cu1A**, which suggest that **Cu1A** would be a better SOD mimetic than **Cu1B**. This can be related with the many changes that **Cu1B** must undergo during its redox cycling which requires significant amount of energy. Moreover, while looking at the structure with van der Waals spheres, we can observe that there is no available space for the superoxide anion to coordinate for doing the electron transfer, even after two bonds break.

Table 14 Electron affinity for Cu1B

Complex	Energy Singlet [E_h]	Energy Doublet [E_h]	EA [E_h]	EA [kJ/mol]
Cu1B	-4007.16	-4006.99	-0.17619	-462.587

4.2.6.2.3 Molecular Orbitals of Cu1B

The reactivity parameters for **Cu1B** are summarize in Table 15. The band gap is the smallest relative to ligands and **Cu1A** suggesting that is a more reactive specie. However, the electrophilicity, in singlet and doublet state, parameters are smaller compare with the ones obtained for **Cu1A**. This suggest that this complex is less attracted to electron rich compounds as superoxide anion in accordance with the less SOD activity predicted previously. Also, according to da Silva *et al.*[112], the lower the HOMO energy of the reduced species, the better the stabilization of the extra electron which also suggest that **Cu1A** would have better SOD mimetic effect [112].

Table 15 Reactivity parameters for Cu1B

HOMO [eV]	**LUMO [eV]**	**Band gap [eV]**	**η [eV]**	**μ [eV]**	**ω [eV]**	**HOMO [eV]**	**LUMO [eV]**	**Band gap [eV]**	**η [eV]**	**μ [eV]**	**ω [eV]**
Doublet						**Singlet**					
-7.565	-0.993	6.572	3.286	-4.279	2.786	-6.818	-0.546	6.272	3.136	-3.682	2.162

Besides these parameters, the orbitals involved in the redox process are shown in Figure 42. As can be seen, the SOMO in the neutral state is mainly located in the $d_{x^2-y^2}$ of the metal and the p_x and p_y orbitals (two of each) of nitrogens. Upon reduction, the HOMO orbital of the reduced specie no longer has just the contribution of the metal and nitrogens but also from part of the ligands and water. Moreover, the metal's orbital involved in HOMO orbital of Cu^+ is d_z^2 that strongly fusses with the electron density from nitrogen. This indicated that there is a change in the order of the orbitals, HOMO is fill with electrons and in tetrahedral geometry d_z^2 is expected to be filled which confirms the geometry shift (inversion of orbitals in octahedral and tetrahedral crystal fields diagrams). All these significant electronic changes may reduce the efficiency of redox cycle.

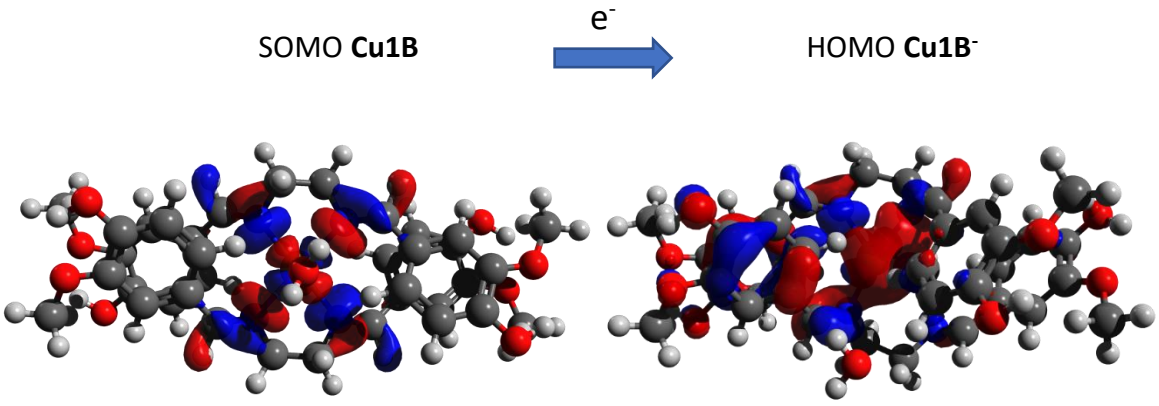

Figure 42 Orbitals involve in the reduction of Cu1B

4.3 Set of ligands derivate from vanillin with aniline and its derivatives (L2X)

In total, four ligands were obtained, the difference between them rely on the *para* position. In this sense, as observed in Figure 43, the name regarding the *para* position would be for -H (**L21**), -OH (**L22**), -Cl (**L23**) and -CH_3 (**L24**). Regarding physical aspect, all of them present yellow color and tend to be crystalized. The yield of the reactions were: **L21** 80.94%, **L22** 95.87%, **L23** 91,08% and **L24** 84.83%. All of them were highly soluble in ethanol, acetonitrile, chloroform, hexane, but insoluble in water.

The melting point slightly differ between each other due to the substituents in *para* position, the order from lowest to highest was for L24 (117 - 119 °C), L23 (129 - 131 °C), L21 (147 – 155 °C) and L22 (203 - 206 °C). These results are consistent with the type of interactions observed for the ligands, for example, -OH *para* substitution facilitate hydrogen bond interactions which further stabilized the compound. The range of melting is very narrow which suggest the purity of the ligands. The reaction scheme and experimental pictures are shown in Figure 43, the nomenclature of the ligands for further discussion would be **L2X**.

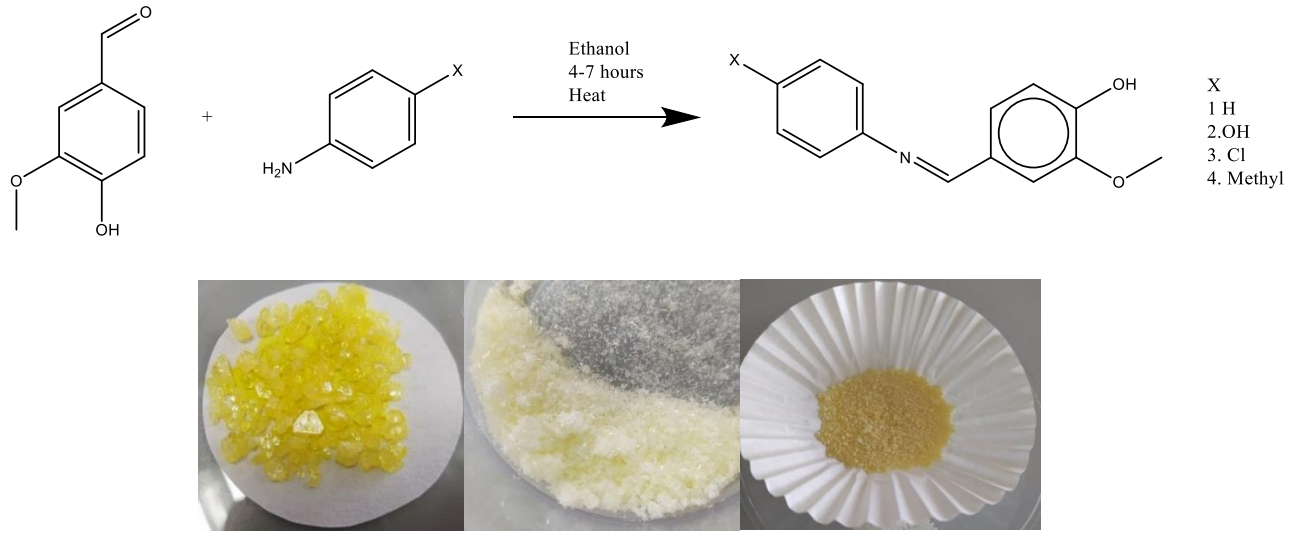

Figure 43 Reaction scheme for set of Ligand 2 and experimental pictures of the L2X

4.3.1 Geometry optimization L2X

Regarding geometry optimization, different starting orientation of the aromatic rings respective to each other were tried, but all end up converging to a non-planar structure regardless of the *para* substituent, but with slightly different dihedral angle of C_7-N-C_9-C_{10} (as seen in Figure 44 a). In

this sense, the dihedral angles obtained are respectively -41.3° for **L21**, -35.6° **L22**, -41.7° **L23** and -39.5° **L24**. A clear tendency is observed, ligands with *para* electron donor substituents have a smaller dihedral angle (C_7-N-C_9-C_{10}) compare with **L21** specially if the donation effect is due to resonance rather than induction effect. Meanwhile, when the substitution is an electron withdrawing group, the angle is bigger. This indicates that there is more delocalization of the electronic density around the ligand when there are electron donating groups. Moreover, previously in 2018 Hijas *et al.*[116] made a computational analysis for **L21**, and although the basis set and method used are different, the geometric parameters are almost equal which confirm the success of our analysis. The final structures for the ligand and its protonated version **(L2XH)** can be seen in Figure 44 .

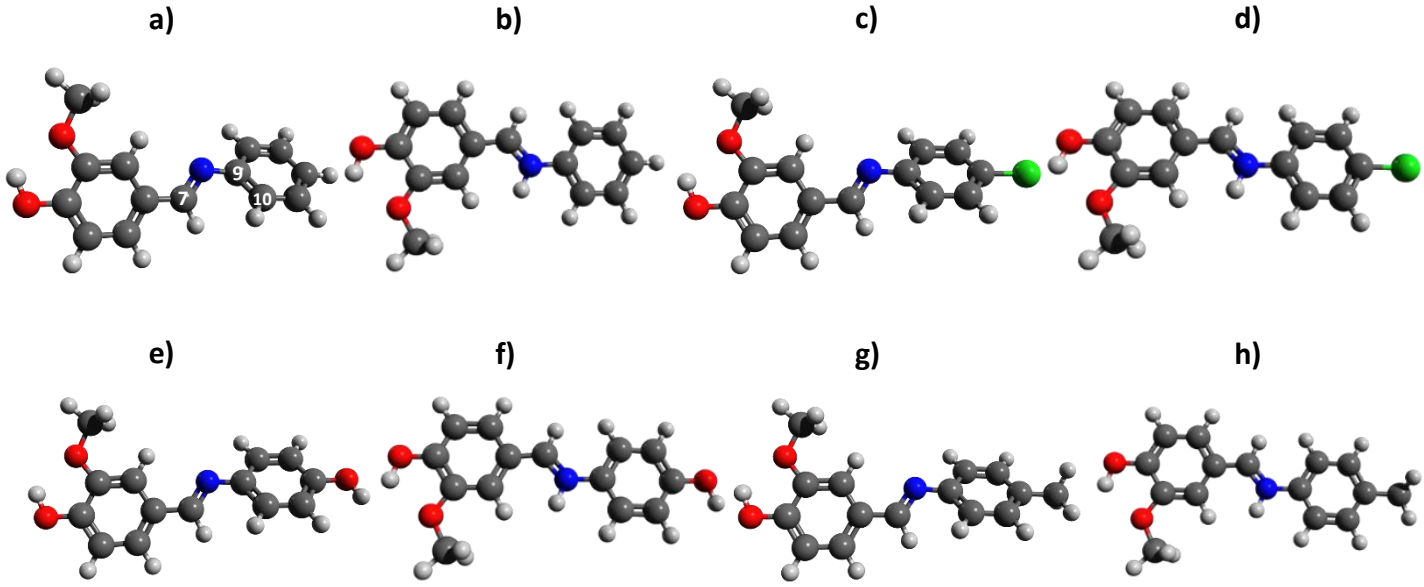

Figure 44 Final geometry optimization for a) L21 b) L21-H c) L23 d) L23-H e) L22 f) L22-H g) L24 and h) L24-H

Due to results regarding UV-Vis and FTIR, for all the ligands, the protonated form of the ligand was as well optimized. These structures provide information which would help to better explained experimental results discussed in the following sections. The main difference between the ligand and its protonated counterpart is regarding the planarity, in the protonated ligand the dihedral angle between the rings is of about ~1°, so the electrons are more delocalized.

4.3.2 IR results for L2X

IR spectra as measured for each of the ligands. As can be expected the results are similar due to the nature of the general structure. Nevertheless, in general, depending on the chemical entity in the *para* position the peaks are slightly shifted. The spectrum of **L21** would be initially discussed in detailed then, the difference observed between **L21** and the others **L2X** ligands would be indicated specially regarding bands for the substituents in para position: C-O (-OCH_3), C-Cl and -CH_3 bending that confirmed the uniqueness of each ligand.

The IR results for ligand **L21** are shown in Figure 45. The broad signal around 3000 cm^{-1} has been associated with stretching of the aromatic -OH. This peak hides the peaks of stretching of -CH for aromatic and non-aromatic carbons. A new peak is observed al 1621.3 cm^{-1} which does not have the characteristic shape (width and strong intensity) for a C=N stretching, but it was computationally confirmed. The condensation is confirmed as the shape and intensity of this band is consistent with the results obtained in previous analysis[116]. For C=C stretching, two peaks are observed since each ring vibrates at different wavenumbers. The peak for the stretching of C-N is at ~1203.9 cm^{-1} that are within the expected range [120]. However, for computational calculation indicate that this is not just purely C-N but also stretching of O-C from -OCH_3. The bending of C-O is observed at 1280.3 cm^{-1} for aromatic -OH and at 1157.3 cm^{-1} for a joined bending of -OH and -OCH_3. Another very sharp peak is due to bending of -CH_3 at 1426 cm^{-1}. As would be expected, many out of plane (oop) bending of aromatics H are observed at 969.1, 768, and 693 cm^{-1}.

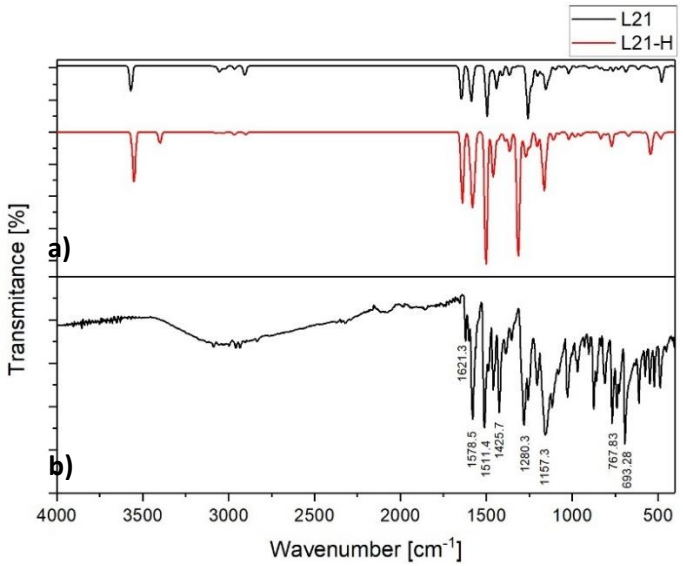

Figure 45 FTIR results for L21. a) Theoretical simulations for protonated and non-protonated ligand b) Experimental result.

Regarding computational results, in general, the comparison with the experimental results is acceptable, although bigger shifts are observed at higher wavenumber. This is not an uncommon result and other approaches such as dual scaling are used to improve the results. Dual scaling consists on using two different scaling factors depending upon the region of the spectrum (one between 4000-1000 cm^{-1} another <1000 cm^{-1})[134] . However, this approach was not taken because IR peak scaling values were not found for our specific set up of method and basis set. Moreover, it seems like the spectrum is much more alike to the result for the ligand without protonation. Nevertheless, in the area around ~1200 cm^{-1} is better expressed by the protonated species, so it is likely that the result comes from contributions of both species.

Now, the experimental IR results for the other ligands of **L2X** set, a small discussion would be made in the following paragraphs. Experimental IR for **L22** presents a defined peak between 3520-3110 cm^{-1} is observed for the stretching of the aromatics -OH. The peak for C=N is shifted in respect to the experimental peak for the same stretching in **L21**. Many more peaks are observed in the experimental spectrum around 1300-1000 cm^{-1} since there are more band regarding C-O due to the contribution corresponding to aminophenol part. The distinctive peak for the IR spectrum of **L22** is a C-O bending at 1241.2 cm^{-1} for -OH of aminophenol ring consistent within the expected range for this band 1300-1000 cm^{-1} [120].

On the other hand, in the experimental IR spectrum of **L23**, the peak for C=N is observed at the same position as for **L21**. However, in this spectrum, there are three peaks instead of two for C=C with values shifted in respect to **L21**. Something important is that in the IR spectrum, the C-O bending peaks are at lower wavenumber as effect of the whole resonance of the molecule. The characteristic experimental IR peaks for this compound are two bands of C-Cl stretching at 680.23 and 406. 27 cm^{-1}, bands regarding C-Cl are expected to show up in the range 900-400 cm^{-1} [135]. Finally, the experimental IR spectrum for **L24** shows that the peak for C=N is shifted in respect to the observed one for **L21** to upper wavenumber by 2 cm^{-1}. An important peak in the experimental spectrum is observed at 1425.7 cm^{-1} for stretching of $-CH_3$ of toluidine which is distinctive from the $-CH_3$ of vanillin.

The previous description was made based on the experimental spectrum. Finally, all the theoretical and experimental values are summarized in Table 16. Just based on experimental IR results, a clear

tendency to conclude that electron donor or electron withdrawing groups shift in a special way the bands cannot be made.

Table 16 IR results for L2X. The theoretical values were taken from the non-protonated L2X calculation

IR bands for L2X							
	Compound	**C=N [cm^{-1}]**	**C-N[cm^{-1}]**	**C=C [cm^{-1}]**	**Special [cm^{-1}]**	**C=C oop**	**C-O**
Exp	**L21**	1621,3	1203.9	1578.6 1511.4	-	768, 693 969.1	1280.3, 1157 1026.8
Theo		1643.9	1201.78	1585.4, 1496.0	-	759.96, 687.73, 973.21	1258.7, 1152.0, 1021.3
Exp	**L23**	1621.3	1209.5	1597.1, 1507.7	C-Cl 406.27, 680.23	933.69, 862.87 827.47	1274.1, 1155.4, 1024.93
Theo		1643.9	1203.6	1588.9, 1496.0	398.8 667.09	849.39, 828.75	1258.7, 1154.55, 1017.9
Exp	**L22**	1623.2	1205.7	1587.8 1507.7	C-O aminophenol 1241.2	836.78, 861,01	1280.3, 1263.5 1028.7
Theo		1643.9	1196.7	1595.7, 1492.5	1241.5	832.19	1296.5, 1255.2, 1021.3
Exp	**L24**	1623.2	1209.5	1585.9 1507.7	υ CH3 Toluidine 1425.7	820.01, 864.74 935.56	1274.7, 1155.4, 1030.6
Theo		1633.6	1203.6	1575.1, 1499.4	1434.1	811.55, 839.07, 952.57	1310.2, 1165.8, 1017.9

4.4 UV-Vis for set of Ligands L2X

First, the decision of theoretical set up would be discussed, and later, a general description for **L22** would be made. To begin with, three different set up (methods that are shown in Figure 46) were tested for the UV-Vis: B3LYP/6-311G** (method ***a***), PBE0/TZVP (method ***b***) and CAM-B3LYP/TZVP (method ***c***) which results are shown in Figure 46.

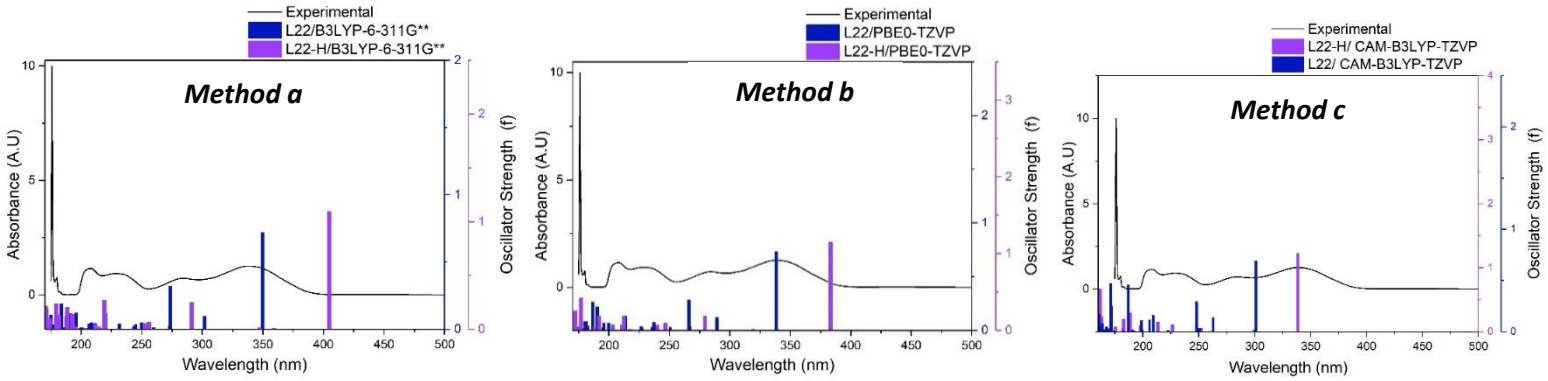

Figure 46 Different TDDFT calculations for L22 from left to right: methods a, b and c.

It is important to clarify that two different molecules were considered, protonated (**L22-H**, pink) and non-protonated (**L22**, blue) ligands, to perform the calculations. The possibility of having

protonated species is plausible to some extent, since acid was used during the synthesis. Moreover, that three different computational methods were used to simulate the spectrum as defined by Figure 46.

To begin with, the peak of lowest energy is observed 339 nm. The Method ***a*** allows to calculate a transition of the unprotonated specie shifted about 10 nm in respect to the experimental currently discussed peak. Meanwhile, method ***b*** involves the prediction of a transition with less than 1 nm of shift with respect of the study peak for the ligand with no protonation. Moreover, method ***c*** gives a similar result than the previous one for the protonated ligand. Regarding the peak at 284 nm, method ***a*** and ***b*** show similar results having three peaks in the zone and the closest one being from the protonated species. On the other hand, method ***c*** simulates only one strong peak shifted 17 nm to longer wavelengths.

Then, the peak at 235 nm is not well represented by neither of the systems. In the case of methods ***a*** and ***b***, there are transitions near the correct position, but the oscillator strength is small. Meanwhile, in method ***c***, there is a calculated strong transition at 248.1 nm, that although shifted 12 nm from experimental result represent better the system that the other methods. Next, the peak at 208 nm is in general well represented by all methods. Finally, regarding the stronger transition around 200 nm, these are better represented by method ***c***.

In general, method ***a*** is the less capable of representing the system, so it will not be further discussed. Between method ***b*** and ***c***, the decision is much more complex. Method ***b*** would require the protonated molecule to correctly represent the transition around 175 nm, but this implies a peak at about 380 nm which is not observed experimentally. Finally, method ***c*** would be used for the rest of calculations since the results for the protonated and no protonated species complement each other and agree with experimental results. The UV-Vis analysis with different method was made to justify that the use of protonated species is not just a result due to the method or basis set. The assignation of the peak using computational simulations are shown in Table 17, and the corresponding experimental result for the other ligands are shown in the annexes section.

In general, all the ligands show the same peaks but slightly shifted one in respect to the others. The general discussion will be made for **L22,** the experimental, theoretical and assignation results are shown in Table 17. The first two peaks at 339 and 284 nm, are due to HOMO→LUMO transition of protonated and non-protonated species respectively. The HOMOs are distributed around the

whole molecules meanwhile the LUMOs exclude -OCH_3, the shift is due to the planarity of the molecule. For the peak at 229 nm, two contributions would be considered. One from the from the non-protonated species in a transition from electrons on the lonely pairs of nitrogen and oxygen of -OCH_3 to π^* of the molecule. The other from the protonated specie, from π distribute around the molecule to π^* located only in the ring of aminophenol. The peak at 208 nm involves the transition from π located in the ring of aminophenol to π^* located in the whole molecule. Finally, transition at 182 nm due to transition of electron from the nitrogen and oxygen lonely pairs to the π^* of aminophenol.

Table 17 UV-Vis experimental and theoretical results for L22

Exp [nm]	Theoretical [nm]	Contribution	Assignment	Exp [nm]	Theoretical [nm]	Contribution	Assignment
339	338.5 (H)	HOMO → LUMO 94.88%	$\pi \rightarrow \pi^*$	208	208.5 (7)	HOMO-3 →LUMO 64.37%	$\pi \rightarrow \pi^*$
						HOMO →LUMO+1 17.23%	$\pi \rightarrow \pi^*$
284	300.9	HOMO→LUMO 79.02%	$\pi \rightarrow \pi^*$	182	182.9 (14)	HOMO-4→LUMO+1 66.35%	$n \rightarrow \pi^*$
						HOMO-1 →LUMO+1 11.37%	$n \rightarrow \pi^*$
229	222.9	HOMO-4→LUMO 35.72%	$\pi \rightarrow \pi^*$	176	171.9 (16)	HOMO-5→LUMO 20.49%	$\pi \rightarrow \pi^*$
		HOMO-1 →LUMO 32.50%	$\pi,n \rightarrow \pi^*$			HOMO →LUMO+7 30.87%	$\pi \rightarrow \pi^*$
	226.4 (H)	HOMO -3 → LUMO 41.22%	$\pi \rightarrow \pi^*$				
		HOMO → LUMO+1 38.87%	$\pi \rightarrow \pi^*$				

4.4.1 Biological analysis of L2X

4.4.1.1 *Geometry changes upon redox process of L2X*

The general structural changes observed upon reduction for **L21** is shown in Figure 47. A general description for **L21** would be made in the following paragraph, for the other ligand a little description of specific bonds will be made. The changes of structure during redox cycle is important in order to understand where the electron received would be upon reduction. In general, all **L2X** share the same structure, the *para* position sustituent does not affect greatly the bonds or angles in the structure in singlet or doublet state.

In the singlet state, the length of the C-C bonds in the rings is similar being ~ 1.38-1.39 Å, but there are two C-C bonds out of this range. First, C_1-C_3 is shorter 1.374 Å and C_4-C_1 that is longer 1.406 Å. Moreover, the dihedral C_3-C_1-O_1-C_8 es -1° showing that -OCH_3 is in plane with the ring of vanillin, something similar happens with –OH substitution. Although there is significant resonance in the molecule, it is not completely flat, the dihedral between C_7-N-C_9-C_{10} is -41.3 °, which is the only parameter with significant different between the ligands: **L23** is -41.7, **L24** -39.5

and -35.6° for **L22**, which relates with whether the substituent is electron donor/withdrawing, in case of donating groups, the angle is smaller due to resonance.

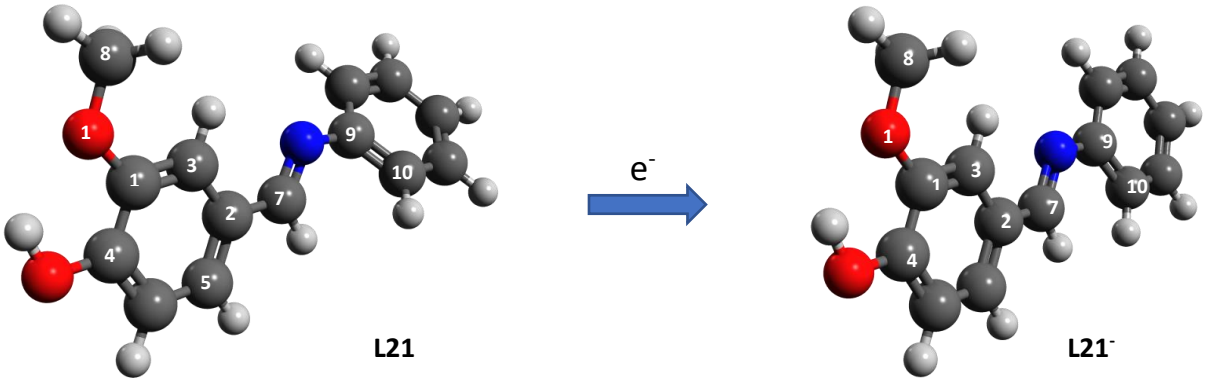

Figure 47 Geometry changes upon redox cycle from L21 to L21⁻.

Upon reduction, the main difference observed is regarding the dihedral C_7-N-C_9-C_{10} that for **L21**$^-$ is reduce to -7.8 °. Moreover, the length of the bond for C-N and C-O bonds increase which suggest a more single bond character, and the bonds C_5-C_2, C_9-C_{10}, and C_3-C_2 increase in length. As in singlet, the main change among the ligands is the dihedral C_7-N-C_9-C_1, that is for **L22**$^-$ -8.3°, **L23**$^-$ -5.6° and for **L24**$^-$ -8°. Different to the behavior observed for the neutral ligand, in the reduced ligand, the dihedral angle is larger for the ligands with electron donor substituent and smaller for electron withdrawing strongly related with the fact that the free lonely pairs of electrons are now in a bond with a proton. Therefore, better electronic delocalization is expected in **L23**$^-$.

4.4.1.2 *Electronic Affinity for L2X*

As discussed previously, the electronic affinity is an important parameter for SOD mimetics. The values calculated for this set of ligands are shown in Table 18. The most negative value obtained for the set of ligand **L2X** was for **L23** which suggest this would be the best biomimetic from **L2X** set, **L23** is the only ligand of this set with electron withdrawing substituent in *para* position. **L22** is the worse SOD mimetic because through resonance -OH donates extra electronic density to the ligand and therefore to the metal. Upon reduction, for this ligand it would be more difficult to accommodate an extra electron. Meanwhile, for **L23,** chlorine is an electron withdrawing group that upon reduction, due to its electronegativity is capable of attracting electrons to itself helping to delocalize the extra electronic density over the whole molecule.

Table 18 Electron affinity for set of ligands 2

L2X	Energy Singlet [E_h]	Energy Doublet [E_h]	EA [E_h]	EA [kJ/mol]	EA (Relative) [kJ/mol]
L23	-1206.074	-1206.158	-0.084	-219.894	0.000
L21	-746.443	-746.524	-0.081	-213.060	6.834
L24	-785.751	-785.831	-0.079	-208.219	11.675
L22	-821.685	-821.762	-0.077	-203.093	16.802

4.4.1.3 *Frontier orbital analysis for L2X*

Regarding SOD mimetics, in the reduction step, the orbital LUMO of the neutral molecule is important as the electron would be receive here. As can be seen in Table 19 , the molecule with the lowest energy of LUMO is the one with electro withdrawing group, these results are consistent with the ones for EA suggesting that **L23** is the best SOD candidate.

Table 19 Reactivity parameters for L2X

L2X	HOMO [eV]	LUMO [eV]	Band gap [eV]	η [eV]	μ [eV]	ω [eV]	$L2X^-$	SOMO [eV]	LUMO [eV]	Band gap [eV]	η [eV]	μ [eV]	ω [eV]
Singlet L2X							**Doublet $L2X^-$**						
L23	-7.289	-0.604	6.685	3.343	-3.947	2.330	$L23^-$	-3.893	1.146	5.039	2.520	-1.374	0.374
L21	-7.286	-0.531	6.755	3.378	-3.909	2.261	$L21^-$	-3.833	1.351	5.184	2.592	-1.241	0.297
L24	-7.186	-0.498	6.688	3.344	-3.842	2.207	$L24^-$	-3.766	1.308	5.074	2.537	-1.229	0.298
L22	-7.029	-0.470	6.559	3.280	-3.750	2.143	$L22^-$	-3.699	1.194	4.893	2.447	-1.253	0.321

Moreover, it is widely discussed that the smaller the band gap the more reactive a molecule tends to be. In this case, the most reactive one is **L22** followed by **L23**, but this does not necessarily imply a better SOD mimetic behavior. Finally, it is known that superoxide anion is an electron rich specie, therefore, compound with good electrophilicity as **L23** are expected to better interact with the substrate.

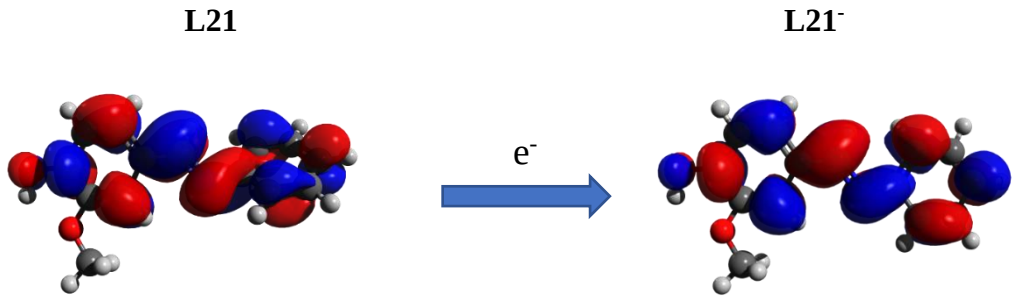

Figure 48 Orbitals involve in redox process from L21 to $L21^-$.

Regarding the orbitals which can be observed in Figure 48, LUMOs of **L2X** are almost identical to the SOMO of **L2X**$^{-}$ showing that there will be no significant changes during redox cycling. In all the cases, the *para* substituent is part of the orbital which remark its importance in the redox process. Finally, in neither of the orbitals is included -OCH_3, so the lonely pairs are not expected to participate in the process of electron transfer. Finally, the accepted electron distributes around the whole molecule.

4.5 Complexes with ligands L2X

Using the ligands **L2X** previously discussed, a set of complexes were synthetize using copper and manganese metals. A total of three complexes were synthetized using ligands L21, L23 and L24, which will be called Cu21, Cu23 and Cu24 respectively for copper and Mn21, Mn22, Mn23 and Mn24 in a similar manner.

4.5.1 General characteristics of complexes of Cu2X

In total, three different complexes were obtained with copper which are shown in Figure 49. The *para* position has effect on the nature of the coordination showed firsthand by the color. The complexes mainly **Cu21** show a kind of metallic shine that is not completely expressed in the picture. The yield for these complexes was for **Cu21** 70.97%, **Cu23** 79,90% and **C24** 76,07%. The complexes are moderately soluble in ethanol, methanol but not in water, hexane, or acetonitrile. These decompose at ~250 °C which is higher than for the corresponding ligands. For the magnetic properties, the μ_{eff} for the complexes are: **C21** 1.92 BM, **C23** 2.03 BM, and **C24** 2.08 BM. These results suggest that copper is found in 2+ state.

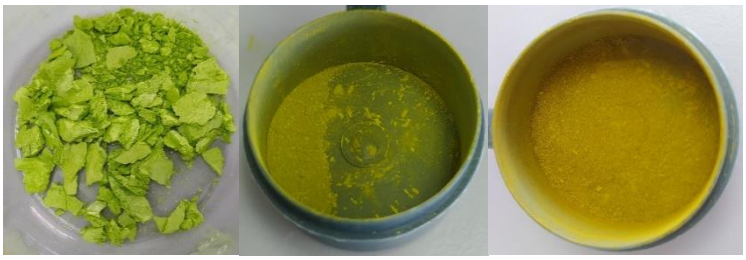

Figure 49 Copper complexes with L2X from left to right: Cu21, Cu24 and Cu23.

4.5.2 General characteristic of complexes of Mn2X

In total four complexes with manganese were obtained, all of them of orange color as observed in Figure 50. Their decomposition point is similar to the ones observed for copper complexes at ~

220°C. The complexes are soluble in ethanol, methanol, acetonitrile, slightly in water but not in hexane. The yield for the complexes is less that the ones obtained for the copper complexes, **Mn21** 50.38%, **Mn22** 60.58 %, **Mn23** 57.25% and **Mn24** 54,02%. The magnetic measurements show Mn^{2+} being a d^5 specie, the values obtained were higher than the ones expected for Mn^{2+} probably because there are still residues of ligand, **Mn23** was 6.23, **Mn24** 6.27, **Mn22** 6.25 and **Mn21** 6.16 BM.

Figure 50 Manganese complexes from left to right Mn21, Mn23 and Mn24.

4.5.3 Geometry optimization

4.5.3.1 *Complexes of copper* Cu2X

Initially, it was unclear which would be the coordination mode for the copper complexes. Therefore, two different alternatives were taken. The first alternative, the coordination of copper with two nitrogens (from two ligands) and two waters, which forms a square planar geometry.

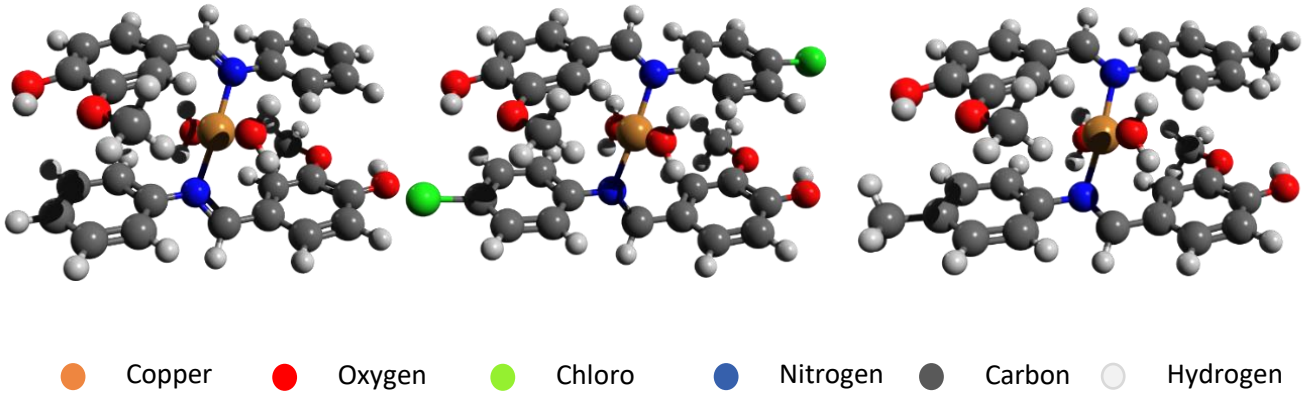

Figure 51 Optimized structure Cu21, C23 and C24

Additionally, the possibility of four water molecule was tried but it was prohibited by steric hindrance due to little available space between the ligands. The second alternative mode, in which copper coordinates through the oxygens of the vanillin aromatic rings and two waters in the axial

position to obtain an octahedral geometry. The optimized structures for the first approach are shown in Figure 51 .

Energy values are summarized in Table 20. As can be seen, in all the cases, the complexes coordinated through nitrogen are much more stable for more than ~100 KJ/mol than the ones through oxygen. This is similar to the behavior observed for **Cu1A** and **Cu1B,** as explained earlier, this is due to the preference of copper to coordinate through nitrogen. Therefore, these geometry optimizations would be used for the following calculations.

Table 20 Energy for complexes with ligands 2 with copper

Cu2X	**Coordination Nitrogen**	**Coordination Oxygen**	**Difference**
	Energy (Eh)	Energy (Eh)	Energy (KJ/mol)
Cu21	-3284.107	-3284.065	-110.341
Cu23	-4203.048	-4203.007	-107.604
Cu24	-3362.643	-3362.598	-118.051

4.5.3.2 *Complexes with manganese* Mn2X

Initially, using the previous calculated complexes, the copper was changed by manganese and use as starting conformation. Upon the optimization process, the coordination mode was favored through nitrogen. Nevertheless, looking at the experimental IR result, the coordination should be through oxygens because C=N band does not move to lower wavenumbers.

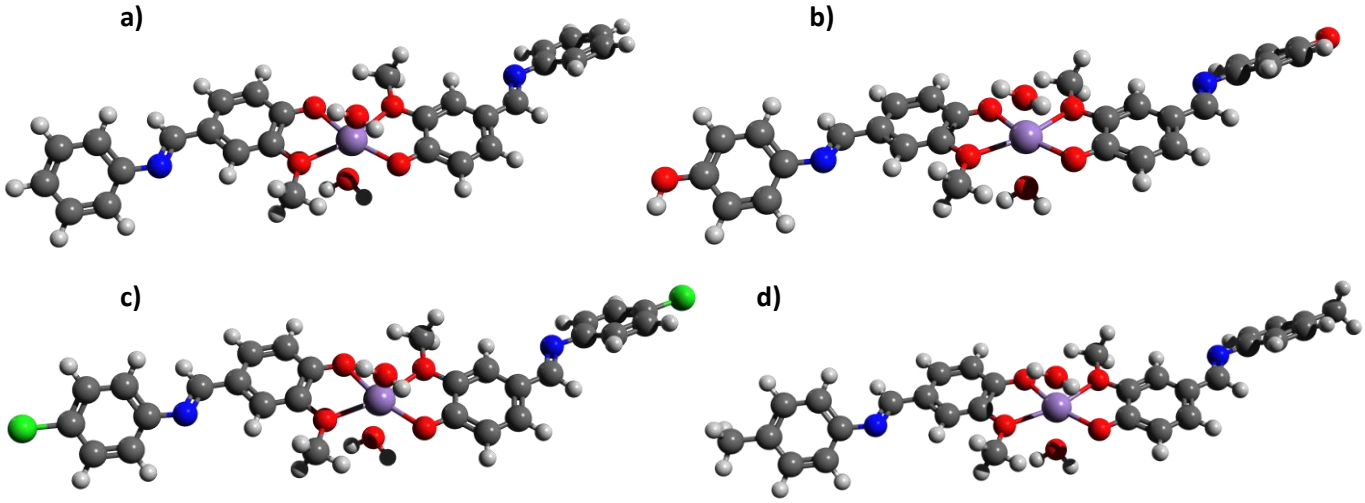

Figure 52 Optimized geometries for Mn2X: a) Mn21 b) Mn22 c) Mn23 and d) Mn24

The possibility of loss of a proton from -OH upon coordination was considered, and in these conditions, the calculations prefer the coordination through oxygen, the optimized structure for **Mn2X** is shown in Figure 52. Moreover, due to the orange color observed for the compounds, its coordination is more likely octahedral rather than tetrahedral[30]. It is not possible to determine whether in the axial position water or chlorine is located because the peaks of Cu-Cl appear below 400 cm^{-1} that is below the range of the equipment used for FTIR[136,137].

4.5.4 FTIR analysis for complexes Cu2X and Mn2X

4.5.4.1 *FTIR complexes Cu2X*

An extended discussion would be made for **Cu23** and the changes observed upon the substitutions in *para* position would be later discussed. The IR spectrum results obtained for **Cu23** are shown in Figure 53. To begin with, the bands observed between 3000 cm^{-1} and 3260 cm^{-1} correspond with aromatic O-H and C-H stretching. Then, the peaks observed between 3000-2750 cm^{-1} are accordingly to the C-H stretching of $-CH_3$. Regarding other important peaks, the C=N is observed at 1584.1 cm^{-1} which is ~ 40 cm^{-1} shifted to lower wavenumber relative to the ligand, and C-N stretching at 1161 cm^{-1} shifted by 40 cm^{-1} to lower wavenumber as well. This suggests that the coordination is through the nitrogen, as it donates electrons which affects the bond distance C=N. Then, C=C stretching is observed at 1490.9 cm^{-1} which is shifted by 90 cm^{-1} in respect to the ligand due to changes in resonance, orientation, and π interaction upon coordination.

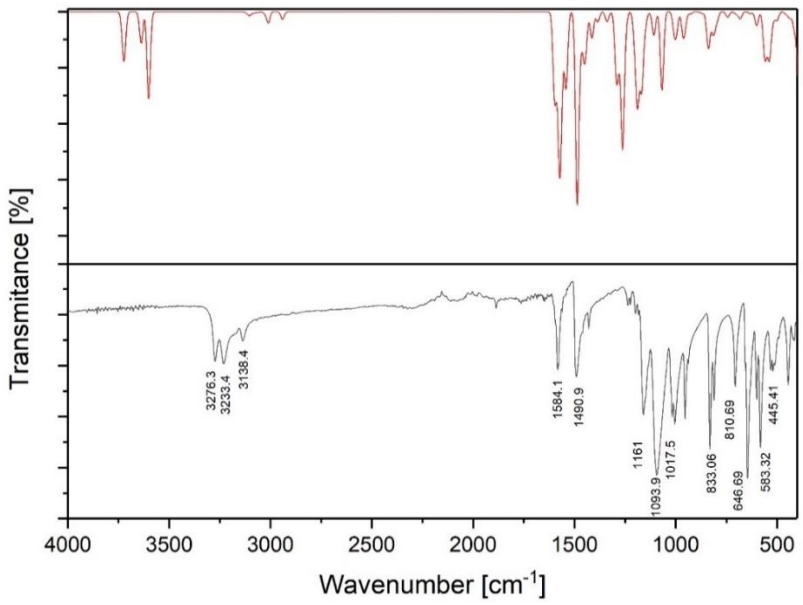

Figure 53 FTIR results for Cu23, red for simulation and black experimental result.

Regarding C-O bands, peaks are at 1161 and at 1017.5 cm^{-1} both of which are slightly shifted from the ligand by about 5 cm^{-1}. Finally, a special peak for this complex is observed at 1093.9 cm^{-1} assigned to C-Cl stretching. The coordination at the same time through N and O is unlikely accordingly to calculations with DFT. The out of plane peaks for hydrogens C-H of aromatic rings are observed at 833.06 and 810.69 cm^{-1}. The coordination was confirmed with the appearance of new bands regarding Cu-N and Cu-O bonds. The peaks of Cu-N have been assigned at 646.69 cm^{-1} and 583.32 cm^{-1} and for Cu-O the peak at 445.41 cm^{-1} consistent with expected ranges [119].

In general, the IR simulation agrees with the experimental results, but there is a peak that show higher intensity that the experimental measurement. Computationally, there is a strong peak observed at 1262.3 cm^{-1} that experimentally is not as strong, instead, a weak peak is observed at 1235.6 cm^{-1}. Computationally, this peak show to correspond to the bending of hydrogens in the vanillin ring, O-H aromatic stretching and bending of H in HC=N bond. Due to the closeness of the hydrogen to the copper, while bending C-H, for the simulation is difficult to correctly assign the electronic charge to hydrogen. The visualization program Gabedit displays a formation of bond between copper and hydrogen, showing that there could be electronic interaction between them, which affects the correct calculation of intensity.

IR simulation is very sensible to conformation, in which even small changes could provoke a shift in the observed peaks of the spectrum. Usually, it is recommended to start geometry optimization and further computational analysis using the XRD determined structure. However, in our case, this experimental technique is not available in the laboratory and the solution of the structure through XRPD was not as simple for the coordination compounds. As the UV-Vis results are in relative concordance, the structures would be accepted as the changes in respect to the real structure should not be as significant. Moreover, the simulation is made in implicit solvation while many other factors may influence the complex in solid state (FTIR was measure in solid). Table 21 shows a summary of the peaks of the different copper complexes.

Table 21 FTIR summarized results for complexes with Cu and Mn

	IR peaks for Cu2X						
Cu2X	**C=N [cm^{-1}]**	**C-N [cm^{-1}]**	**C=C [cm^{-1}]**	**M-N [cm^{-1}]**	**M-O [cm^{-1}]**	**Out of plane C-H [cm^{-1}]**	**C-O [cm^{-1}]**
Cu23	1584.1	1161	1490.9	583.32	445.41	810.69, 833.06	1093.9, 1017.5
Cu21	1591.5	1162.9	1492.7	648.5, 585.19	423.05	689.55	1103.29, 1008.20
Cu24	1591.5	1162.9	1515.1	650.42, 585.19	484.55	956.06, 818.15	1105.10, 1021.20

4.5.4.2 *IR result for set of complexes Mn2X*

The experimental and theoretical IR results are observed in Figure 54 and a summary of the most important bands for **Mn2X** is shown in Table 22. For **Mn21**, the peaks for C-H stretching of aromatic and non-aromatic have not a strong intensity and get lost with background noise so its assignation is complicated. The classic broad peak of -OH is not observed which support that the proton is lost upon coordination, the observed peak around 3000 cm^{-1} must be some remaining ligand (however the peak observed is less broad and much smaller than ones observed in ligand and complex). For this case, the C=N stretching peak is observed at 1647.4 cm^{-1} which is ~20 cm^{-1} at higher wavenumber than ligand which relates to less resonance since the oxygens are donating their electrons to the metal and are no longer in resonance with the C=N bond.

Then C=C stretching are observed at 1587.8 and 1503.9 cm^{-1}, and its values are similar to the ones in the ligand. A C-O stretching for $-OCH_3$ is observed at 1011.9 cm^{-1} and the corresponding bending at 1138.7 cm^{-1}. The C-N stretching is observed at 1209.5 cm^{-1} at longer wavenumber than the ligand, once again oxygen coordination is suggested. A bending for the C-H of HC=N bond is observed at 1315.7 and its corresponding out of plane peak at 795.78 cm^{-1}. Finally, the Mn-O peaks for the oxygen of the rings are observed at 622.46, 590.37 and 521.82 cm^{-1}. Meanwhile the Mn-O with the water are the ones observed near 400 cm^{-1}. As specific peak for this complex is at 1138.7 cm^{-1} due to C-O bending of the -OH in the aminophenol ring.

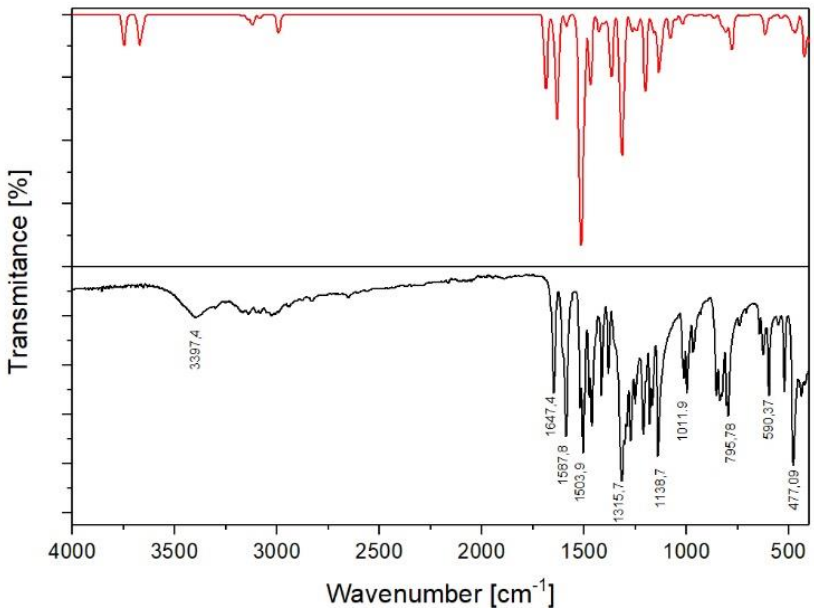

Figure 54 IR for Mn22, red for simulation and black for laboratory results

In all the manganese complexes, there is the appearance of peaks around ~1300 cm^{-1} which were not observed in the copper complexes. This peak has been related with C-H bending of HC=N that probably was not observed in copper because the coordination through nitrogen changes the characteristic of C=N bond and the freedom to vibrate of the C-H bond (steric hindrance). This further support that the coordination mode for manganese is different than for copper. A summary of the results for the **Mn2X** complexes for IR bands are shown in Table 22. Similarly as explained for previous complexes, bases on hard soft acid base theory, Mn^{2+} is consider as a hard acid and RO^- and R-O-R as a hard bases which supports the preference of coordination through oxygens[138].

Table 22 IR results for Mn2X complexes

Mn2X	C=N [cm^{-1}]	C-N [cm^{-1}]	C=C [cm^{-1}]	C-H (HC=N) [cm^{-1}]	M-O [cm^{-1}]	Oop [cm^{-1}]	C-O [cm^{-1}]
Mn24	1645.6	1134.9	1584.1, 1500	1310	594.51, 475.23	831,19	1010.10
Mn21	1647.4	1136.8	1597.1, 1584.1 1505.8	1334.3 1313.8	503.19, 421.18	875.92, 827.47	1010.10
Mn23	1641.8	1131.2	1502.01, 1597.1	1332.5	574.01, 510.64 410.00	831.19, 870.33	1077.20 1011.90
Mn22	1647.4	1138.7	1587.8, 1503.9	1315.7	590.37, 477.09	795.78	1011.90

4.5.5 UV-Vis Complexes with ligands L2X

The results regarding UV-Vis would be discussed. For all the calculations, copper was considered as 2+ and spin 2 due to measurements in magnetic balance, and manganese as 2+ and spin 6.

4.5.5.1 *UV-Vis for copper complexes with L2X*

Table 23 shows the results obtained theoretically and experimentally for the UV-Vis of **Cu21**, the information about the rest of the complexes can be found in annexes section. In general, all the complexes present similar bands just slightly shifted in respect to each other, the main differences are observed for the d-d transitions which are observed at longer wavelength when in the *para* position is located an electron withdrawing group as observed previously in other complexes [139] . Also, despite the type of **Cu2X**, the orbitals involve in the transitions tend to be similar. Before starting to discuss the results, it is important to consider that due to the doublet spin of Cu^{2+}, the HOMO orbital is truly a SOMO. Moreover, the orbitals α of SOMO is fill with an electron meanwhile the β is truly empty so many transitions would be observed here. The names that would be used for the analysis are shown in Figure 55.

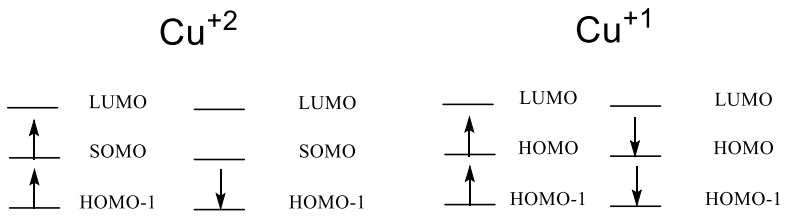

Figure 55 Electronic structure of Cu2X complexes

The experimental UV-Vis spectrum and theoretical transition calculated for **Cu21** are shown in Figure 56. To begin with, the d-d theoretical transitions are not clearly observed in the experimental spectrum due to their low extinction coefficient compared to the charge transfer of strong absorbance at around ~450 nm for **Cu21**. d-d transitions in theoretical calculation are observed at 672.4 nm, involving the transition HOMO-29/HOMO-1 (β) to SOMO (β). The orbital SOMO (β) is formed by the orbital $d_{x^2-y^2}$ of copper and electronic density on water and nitrogen. Meanwhile, HOMO-29 (β) has electronic density distributed on the whole molecule including ligands, water and d_{z^2} of copper, and HOMO-1 has almost all its electronic in the vanillin rings and metal d_{yz} orbital.

Table 23 Summary results UV-Vis complexes for C21

UV-Vis Cu21							
Exp. [nm]	**Theo. [nm]**	**Contribution**	**Assignment**	**Exp. [nm]**	**Theo. [nm]**	**Contribution**	**Assignment**
	672.4 (1)	HOMO-29 (β) → SOMO (β) 21.23% HOMO-1 (β) → SOMO (β) 21.16%	d → d d → d	411	421.5 (9)	HOMO-3 (β) → SOMO (β) 26.52% HOMO (α) → LUMO +1 (α) 13.28%	LMCT
	530.5 (5)	HOMO-2 (β) → SOMO (β) 84.38%	LMCT	285	300.6 (20)	HOMO (α) → LUMO (α) 15.64% HOMO-1 (β) → LUMO (β) 16.76%	ILCT ILCT
411	434.7 (7)	HOMO-3 (β) → SOMO (β) 34.33% HOMO-1 (α) → LUMO (α) 13.98%	LMCT	273	267.8 (26)	HOMO-9 (β) → SOMO (β) 16.76%	LMCT
	424.3 (8)	HOMO-3 (β) → SOMO (β) 24.35% HOMO (α) → LUMO +1 (α) 12.03%	LMCT MLCT				

Then, other simulated transition is observed at ~530.5 nm corresponding to a LMCT from vanillin rings to $d_{x^2-y^2}$ orbital of copper. Experimentally, a clear peak that extends between 400-475 nm is observed. This is a transition HOMO-3 (β) → SOMO (β), the HOMO-3 (β) is conformed totally by electronic density located on the ligands, so this transition is LMCT. At higher energies, the transitions start to involve α and/or β orbital being classify as ILCT/LMCT involving mainly passing electronic density from vanillin rings to be redistributed in just one of the ligands. There is some shift in the calculated for peaks below 300 nm, that are charge transfer transition. Theseis

not uncommon as theses tend to be not always be correctly represented by TDDFT in general being one of its main drawback of this approach, however, our main focused is in d-d transitions that do not tend to present this problem[140].

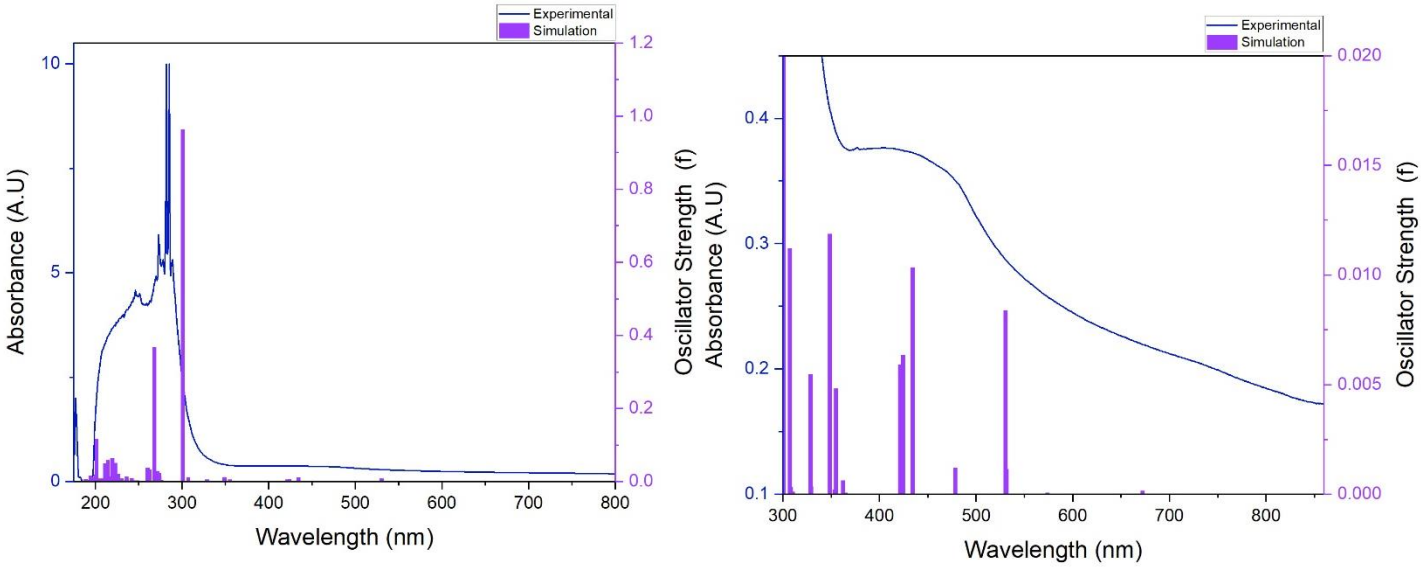

Figure 56 Result of the UV-Vis for Cu21.

4.5.5.2 *UV-Vis for Mn2X complexes*

As discussed in the introduction, Mn^{2+} is a d^5 specie, in our case, it is coordinated with oxygen donors that are weak field ligands, so the electrons are not paired. Therefore, d-d transitions are forbidden for these complexes, the expected transitions are LMCT/MLCT/ILCT. For the following discussions about manganese complexes, the orbitals α and β would be named as shown in Figure 57.

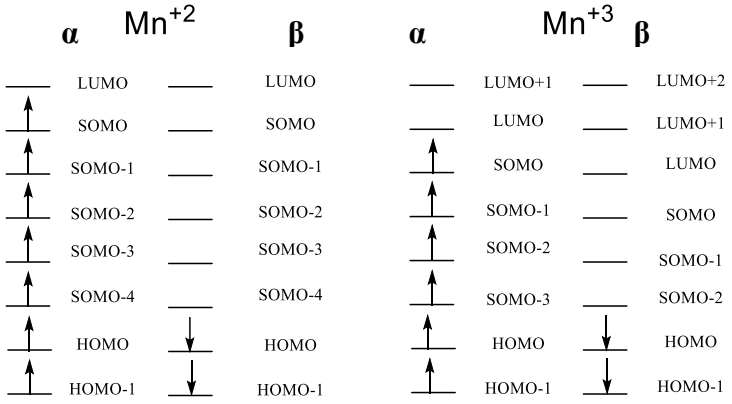

Figure 57 Electronic configuration for Mn2X complexes

The results for UV-Vis analysis for **Mn24** are shown in the Table 24 and Figure 58 , for the other manganese complexes the information can be found in annexes. In general, there are no major difference between the manganese complexes, just small shifts in the peaks, especially the ones near ~450 nm. To begin with, the transition at 429 nm has two theoretical components that differ by 0.01nm. The transitions in both states are almost equivalents with the orbitals involve having small energy differences. For this transition, the α contribution are from orbitals located just in one ligand and d_{zy} metal orbital that is transfer to an orbital locate in the corresponding opposite ligand. Meanwhile, the β component mainly relate with electron transfer from orbitals located in the ligands to orbitals mainly found on the vanillin rings.

The peak observe at 280 nm are due to charge transfer between metal and ligand in which α and β orbitals participate. The MLCT involves a transition from orbitals located in the ligands and d_{xz} orbital of the metal to the π^* of C=N bond of imines. Meanwhile, the LMCT involves the transition from orbitals located in the whole ligand to orbitals that involve just the vanillin aromatic ring and d_{yz} orbital. Finally, the peak at 234 nm has many contributions, the two main show a dual behavior being determine as LMCT and ILCT. The LMCT relates to a similar transition as the one described for 280 nm. The peak of lowest energy, at 210 nm, has contribution from alpha and beta orbitals transitions. In both cases, the electron density is located in the vanillin ring that either transfer to the metal or to the ligands. As explained previously, charge transfer perdition is usually complicated which makes that the predictions of UV-Vis for Mn2X have some shifts respect experimental results.

Table 24 Experimental and simulation UV-Vis results for Mn24

UV-Vis Mn24							
Exp. [nm]	**Theo. [nm]**	**Contribution**	**Assignment**	**Exp. [nm]**	**Theo. [nm]**	**Contribution**	**Assignment**
429	444.4	SOMO (α)→LUMO (α) 20.12%	MLCT	234	216.8	HOMO-9(β)→SOMO-4 (β) 8.21%	LMCT
		HOMO-1 (β)→SOMO-4 (β) 21.49%	ILCT			HOMO-2(β)→SOMO-3 (β) 6.90%	ILCT
	444.3	SOMO(α)→LUMO+1(α) 22.31%	MLCT				
		HOMO (β)→SOMO-3 (β) 26.67%	ILCT				
309	309.7	SOMO(α)→LUMO+5(α) 11.98%	MLCT	210	212.5	HOMO (α)→LUMO+1 (α) 7.37%	
						HOMO-4(β)→SOMO-3 (β) 6.91%	ILCT
	305.6	SOMO (α)→LUMO (α) 19.56%	LMCT				
		HOMO (β)→SOMO-4(β) 16.88%	MLCT				
280	265.6	SOMO-3 (α)→LUMO(α) 11.53%	MLCT				
	254.7	HOMO (β)→LUMO (β) 6.82%	LMCT				
		HOMO (β)→LUMO+1(β) 6.92%	LMCT				

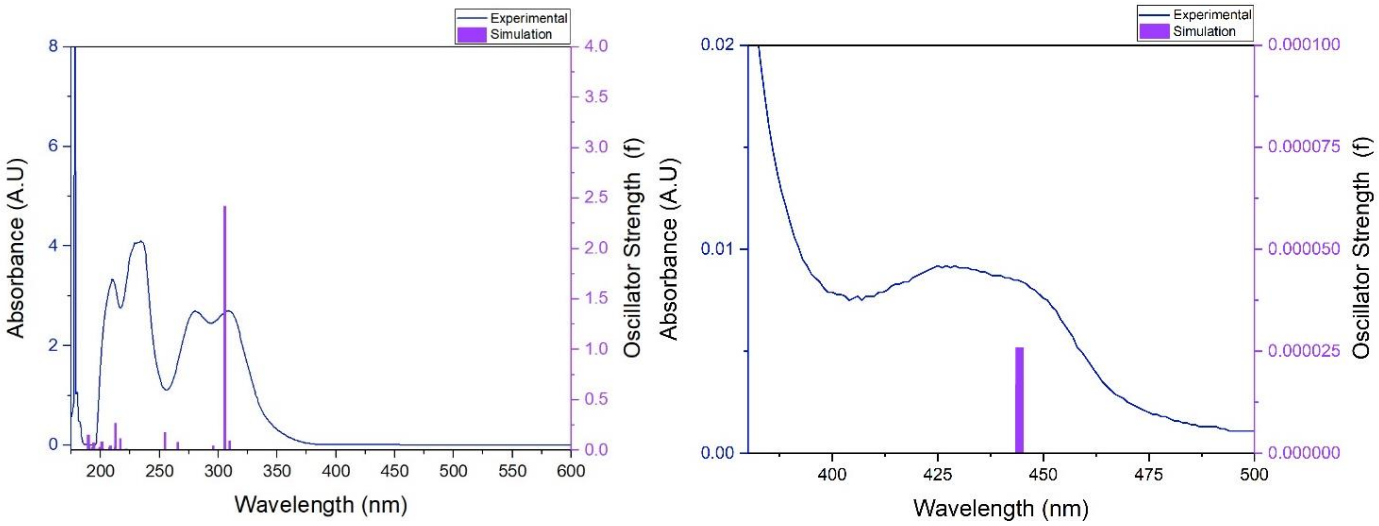

Figure 58 UV-Vis results for Mn24

The peaks observed are very similar to the ones of **L24** as can be observed in Figure 59, the peaks of lower energy present more shift. More shifts are observed in these peaks as these are due to LMCT/MLCT sensible to the nature of the metal and its coordination. Although no d-d can be detected, this suggest that there was a correct coordination of manganese and the ligand which was maintained even in solution. Other technique as EPR would be required to further confirm the coordination in liquid state.

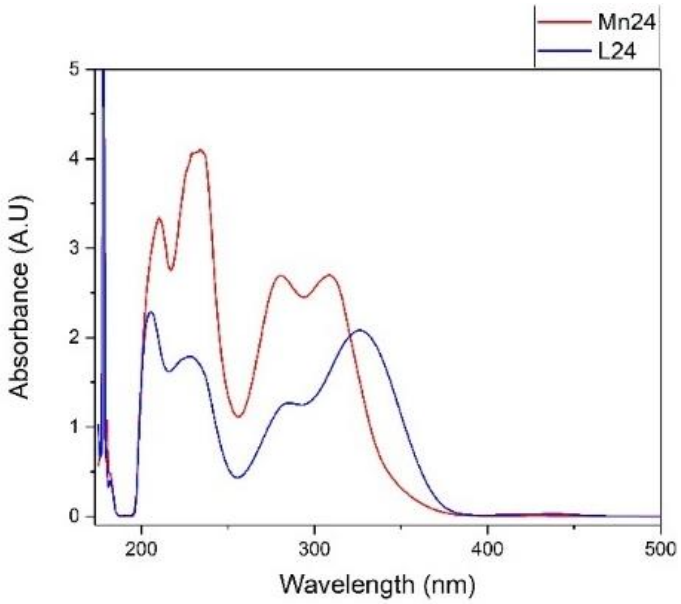

Figure 59 Comparison between L24 and Mn24

4.5.6 Diffuse reflectance of complexes with ligands L2X

4.5.6.1 *Diffuse reflectance UV-Vis of Cu2X complexes*

In some cases, there could be some structural change of the complexes in its solid or liquid state. For that reason, measurements of diffuse reflectance UV-Vis were made to identify possible shift in bands. For the transition of lower energy, an exact maximum for the peak is not observed but rather a broad band between 650-800 nm, it seems like the peak of d-d transitions moves to lower energies. For the second transition of lower energy, a shift of about 20 nm to lower energy is observed, this is due to LMCT. Also, there is a new peak at about ~ 350 nm that were not encounter in liquid state. It is important to point out that the maximum of this peak is not clear as there is a systematic error of the machine provoking a jump in the signal observed at around ~370nm. Therefore, there is an imprecision in the real value of the maximum of this transition. Nevertheless, this peak does not have an equivalent in the liquid state as there are no peaks observed around ~300 nm and should be a new LMCT. The result for all the **Cu2X** is shown in Table 25 and Figure 60.

Table 25 Diffuse Reflectance for Cu2X complexes

Cu21 λ [nm]		Cu23 λ [nm]		Cu24 λ [nm]	
757	295	755	302	778	239
557	234	581	243	571	183
340	182	464	183	346	178
	180	354	179	300	

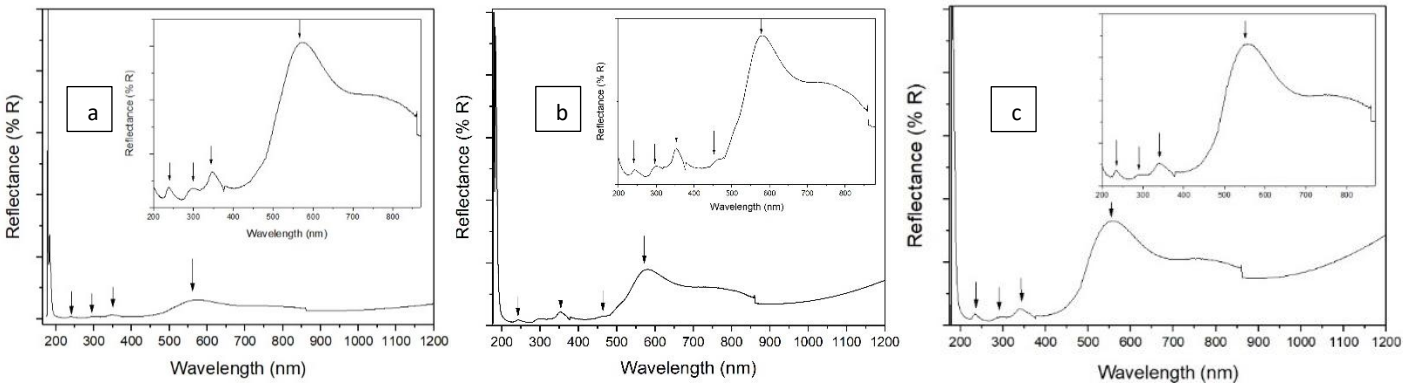

Figure 60 Diffuse reflectance: a) Cu24 b) Cu23 and c) C421

Some plausible explanation is that in solid state, ethanol are the ligands rather than water. Moreover, as the space between the ligands is small, even small change such the replacement of

water by ethanol would affect the geometry around the metal and the orientation of rings affecting π interactions changing the transitions.

4.5.6.2 *Diffuse reflectance UV-Vis for Mn2X complexes*

This test was especially important for the manganese complexes, these complexes were orange in solid state, but when dissolved changed to yellow color. In solid state, peaks that were not observed in liquid appear above 500 nm, in general, all the complexes show these peaks, and the best spectra is observed for **Mn21**.

For **Mn21**, two peaks appear around 570 and 520 nm, which is unusual considering magnetic balance analysis confirmed that the oxidation state for the Mn is 2+. As explained in the introduction, these peaks must be due to relaxation of the UV-Vis rules mainly due to distortion of the symmetry of octahedral conformation. This distortion could be related either to the presence of chloride in the axial positions instead of water or because in solid state the structure is much more distorted than the calculated one due to π interactions of the ligands. A summary of the peaks observed through diffuse reflectance for **Mn2X** are shown in Table 26 and the experimental spectrum in Figure 61.

Table 26 Diffuse reflectance of complexes Mn2X

Mn21 λ [nm]	Mn24 λ [nm]	Mn23 λ [nm]	Mn22 λ [nm]
567	561	578	563
523	517	523	461
462	460	462	295
301	287	264	178
183	182	178	

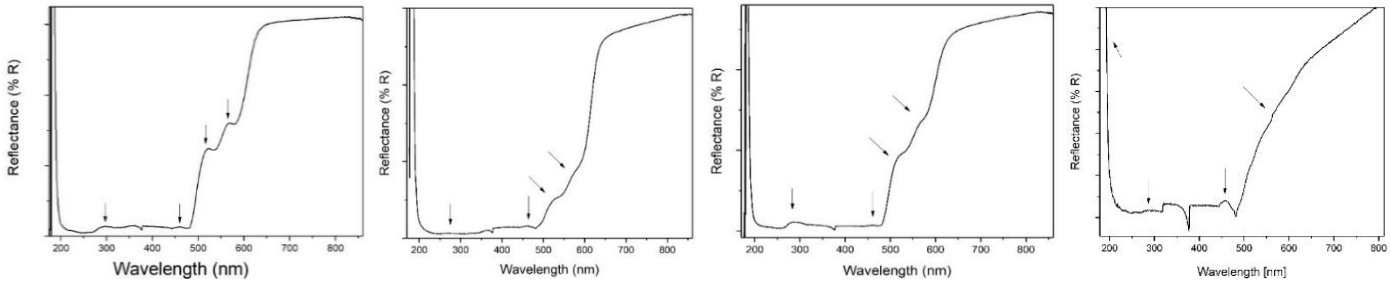

Figure 61 Diffuse reflectance Mn21, Mn23, Mn24 and Mn22

4.5.7 Biological activity of complexes with L2X

The biological activity of the copper and manganese complexes (**Cu2X** and **Mn2X**) will be discussed in this section.

4.5.7.1 *Geometry changes upon redox process for complexes with L2X*

To begin the discussion, the changes of geometry on the complexes would be analyzed starting with the copper complexes followed by the manganese ones.

4.5.7.1.1 Geometry changes upon redox process for Cu2X

To begin with, in the doublet state for **Cu21,** copper is coordinated to two ligands and two waters. For this complex, the tetrahedral parameter is $\tau = 0.35$ that suggest a slightly distorted square planar geometry, as observed in Figure 62, which is a relatively normal coordination mode for copper in this oxidation state[141] . In our case, due to the closeness between the aromatic rings there is no extra space for other ligands.

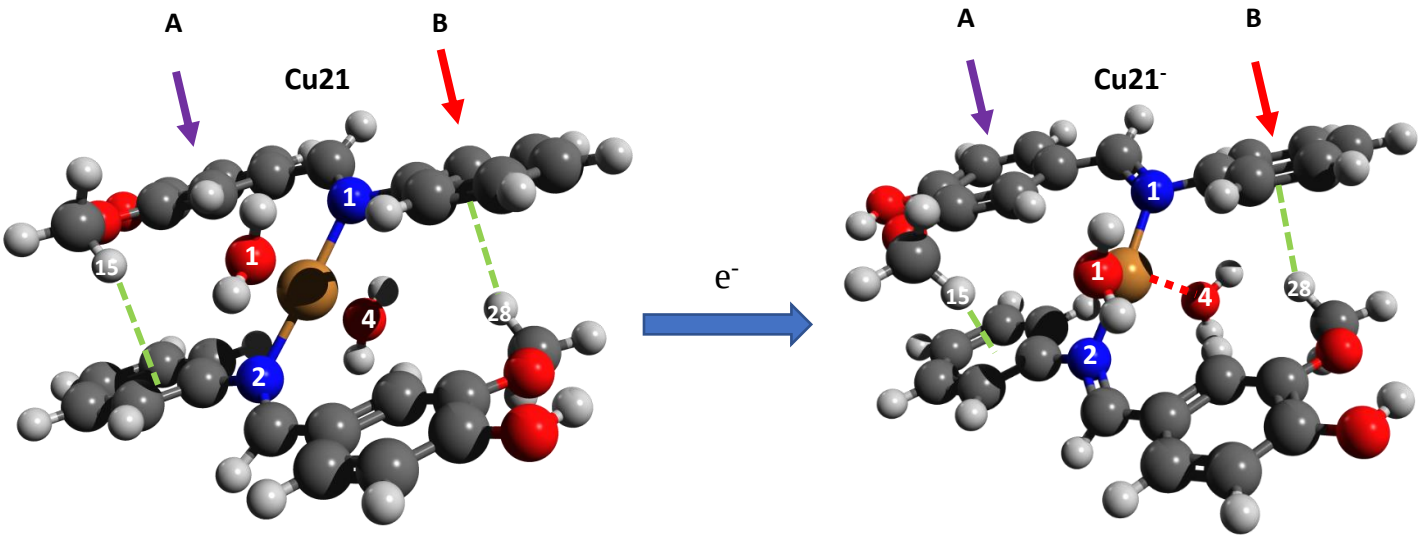

Figure 62 Geometry changes upon redox of Cu21

Upon reduction, there is a significant change in the bond Cu-O_4 from ~2 Å to ~3 Å, which suggests that this bond breaks upon reduction showing a similar behavior to the native CuZn-SOD. The length of Cu-O_1 changes from ~2 Å to 2.3 Å, meanwhile, the Cu-N length bonds are maintained. Finally, the distance between centroids changes upon reduction. In doublet state, the centroids of **rings B** are 5.483 Å apart and in **rings A** 4.722 Å. Upon reduction, the centroids for **B** become further away to 5.964 Å, meanwhile for **A**, the ring get closer at 4.145 Å. Moreover, this structure

present non-conventional hydrogen bonds of the type C-H…π that are show with green dotted lines in the graphic for H_{15} and H_{28} that fall within the expected parameters[142]. In the double state the H..centroid (π) of the ring was for C-H_{28}…π 2.587 Å and for C-H_{15}…π 3.08 Å, upon reduction these become 2.648 Å and 3.593 Å respectively. These changes would influence the π interactions on the system **Cu2X**. Similar behavior is observed for all **Cu2X** complexes.

4.5.7.1.2 Geometry changes upon redox process for Mn2X

The analysis of the manganese complexes is different than the one made for copper complexes. To begin with, neither of the literature reviewed of computational analysis for SOD mimetics has been done with manganese complexes to best of our knowledge. Moreover, the complexes are found with manganese in its Mn^{2+} (reduce state according to MnSOD) rather than in the oxidize state as in copper complexes. Also, there are not break of bond during the redox process, no change in geometry and just small changes in bond lengths and angles as observed in Figure 63.

For **Mn21**, regarding the water molecules coordinated in axial position, the bond length is reduced by 0.2 Å, and the angle between them expands from 159.1° to 178.2° (almost planar). Also, there are changes about the coordination in equatorial position. The bonds M-O (-OCH_3) reduce by 0.01 Å and M-O (-O^-) by 0.2 Å. In both cases, the angles O-M-O involving O in opposite position (between CH_3O-M-O CH_3 or $^-$O-M-O^-) in Mn $^{2+}$ are about 160 ° and upon oxidation it expands to ~ 179 °.

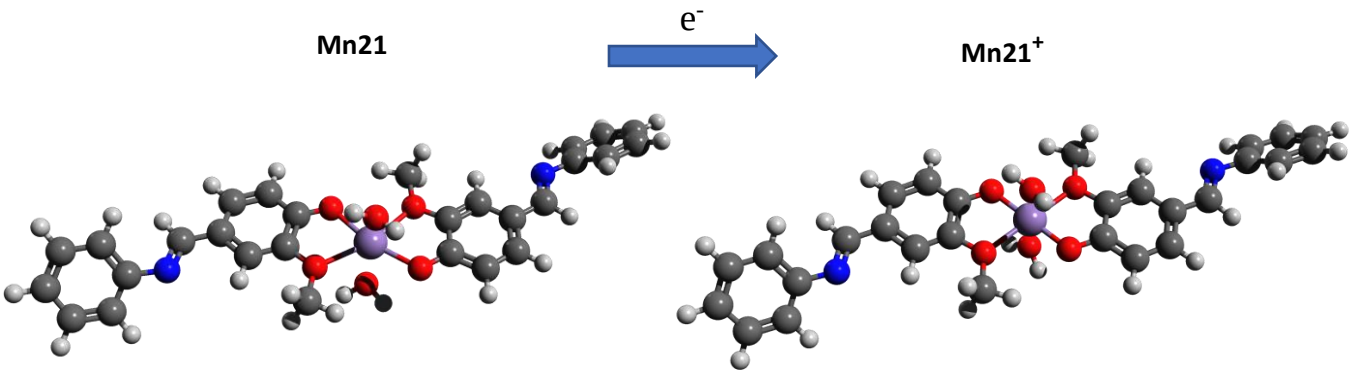

Figure 63 Geometry changes upon redox process of Mn21 to Mn21⁺

Finally, the dihedral angle between the donor oxygen atoms from the ligands in the equatorial position changes from 2° to 0.1° upon oxidation. In general, upon oxidation, the complex has less distortion from the expected perfect parameter of an ideal octahedral geometry. As can be seen in Figure 63, there is not enough space for the superoxide anion to directly coordinates with the

manganese as neither of the bonds move out of the coordination sphere. However, it is possible that the superoxide anion displaces the water molecules in the axial positions, but this cannot be confirmed from these calculations.

4.5.7.2 *Electronic affinity and ionization potential for complexes with L2X*

4.5.7.2.1 Electronic affinity for complexes Cu2X

An improvement in electron affinity is observed upon coordination with copper metal as compared with ligands **L2X**. The electron affinity is about three times lower for the copper complexes. Furthermore, EA decreases in copper complexes in similar manner as in the ligands being the complex with electron withdrawing groups the one with best result as it helps to delocalize the electronic density. The difference of EA, EA relative, increases as well upon coordination making the changes based on *para* substituent stronger than in ligands. The energy and electron affinity values for **Cu2X** complexes are shown in Table 27.

Table 27 Electronic affinity for Cu2X

Cu2X	Energy Singlet [E_h]	Doublet Energy [E_h]	EA [E_h]	EA [KJ/mol]	EA relative [KJ/mol]
Cu23	-4205.039	-4205.239	-0.200	-524.312	0.000
Cu21	-3286.165	-3286.362	-0.197	-516.833	7.478
Cu24	-3364.789	-3364.982	-0.193	-506.671	17.641

4.5.7.2.2 Ionization potential for complexes Mn2X

A different approach should be made to analyze these complexes. Although during the literature review, no computational approach was found for manganese complexes, an analogy with the treatment for copper complexes would be made. In this case, based on the natural manganese SOD, the redox process is expected to happen between Mn^{2+} and Mn^{3+}. Therefore, the ionization potential (IP) would be analyzed instead of the electronic affinity, assuming that if it is easier to remove the electron the SOD mimetic would be better. However, computational approach of SOD mimetic activity for manganese complexes have not been encountered. As can be seen in Table 28, **Mn21** is the compound from which is more difficult to remove an electron, therefore, all the substitutions seem to help to improve the ionization potential. Something particular and unexpected is that **Mn23** has lower ionization potential than the rest of the complexes. Moreover, the energetic difference was not expected to be as significant because the substituent Cl is further

away from the coordination site (small difference is observe among the other manganese complexes).

Table 28 Electronic affinity for Mn2X

Mn2X	Energy Mn^{2+} [E_h]	Energy Mn^{3+} [E_h]	IP [E_h]	EA [KJ/mol]	EA relative [KJ/mol]
Mn23	-3715.04	-3714.88	0.1543	-405.238	0
Mn22	-2946.29	-2946.1	0.1829	-480.255	-75.017
Mn24	-2874.42	-2874.24	0.1832	-480.993	-75.755
Mn21	-2795.8	-2795.62	0.1835	-481.804	-76.566

In general, to analyze the effect of a substituent in an aromatic system (in our cases, the effect of the substituent in *para* position of our ligand), inductive and mesomeric effects have shown to have a significant impact in changing the properties of the aromatic system. Mesomeric effect is related with resonance mechanism and how the π-electrons interact between the substituent and the aromatic system. On the other hand, inductive effect relates with σ electrons in the molecule and its electronegativity. In general, it is discussed that inductive effect become less effective at long distances, which also affects mesomeric effect but in less amount[143]. Based on this, the *para* substituent -OH in **Mn22** has mesomeric effect and would donate electronic density which upon resonance would concentrate near manganese which would make easier the removal of electronic density as shown in Figure 64.

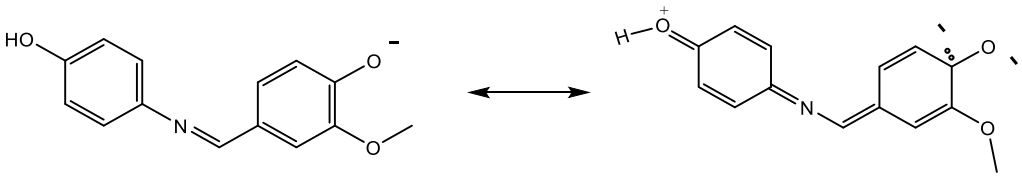

Figure 64 Resonance of L22 ligand

Something similar is expected for **Mn24,** but because -CH_3 is a donor through inductive effect (effect decrease with distance), the overall effect is weaker to improve IP. Finally, for **Mn23,** it is known that Cl is an electron withdrawing group that attract electrons base in inductive effect, and the resonance effect for it is weak because the not good overlap between carbon and chlorine. Upon resonance effect, Cl would tend to donate electrons to the system, usually, the inductive effect is stronger than the resonance one for Cl. However, due to the distant location of the Cl, the stronger effect is difficult to determine for our aromatic system.

4.5.7.3 *Molecular Orbitals analysis upon reduction of complexes with L2X*

4.5.7.3.1 Molecular Orbitals analysis upon reduction of Cu2X

To begin with, the reactivity parameters calculated for Cu2X are shown in Table 29. The band gap in the complexes **Cu2X** is smaller than the one observed for the ligands which indicates as expected that the complexes are much more reactive than the ligands. Furthermore, their electrophilicity in neutral state is higher than the one for the corresponding ligands, so it is much more attracted to superoxide anion.

Table 29 Reactivity parameters for Cu2X

Cu2X	**HOMO [eV]**	**LUMO [eV]**	**Band gap [eV]**	**η [eV]**	**μ [eV]**	**ω [eV]**	**SOMO [eV]**	**LUMO [eV]**	**Band gap [eV]**	**η [eV]**	**μ [eV]**	**ω [eV]**
	Singlet						**Doublet**					
Cu23	-7.45	-0.99	6.46	3.23	-4.22	2.76	-7.96	-1.63	6.33	3.16	-4.79	3.63
Cu21	-7.42	-0.89	6.53	3.26	-4.16	2.65	-7.91	-1.55	6.36	3.18	-4.73	3.52
Cu24	-7.35	-0.76	6.58	3.29	-4.05	2.50	-7.84	-1.56	6.28	3.14	-4.70	3.52

Regarding the shape of the orbitals, observed in Figure 65, in the SOMO orbital of Cu^{2+} there are contribution originating from the orbital d_x^2- $_y^2$ and the electron density of ligands (waters and nitrogen). Meanwhile, the HOMO of Cu^{1+} specie is located over the whole molecule and the d_z^2 orbital of the metal excluding the water that is further away. This indicates that upon reduction, not only the geometry changes, but that the extra electron is distributed along the whole molecule. For that reason, the complex with electron withdrawing donor helps to stabilize the incoming electron. Moreover, in this way the participation of metal in the redox process is assured as well.

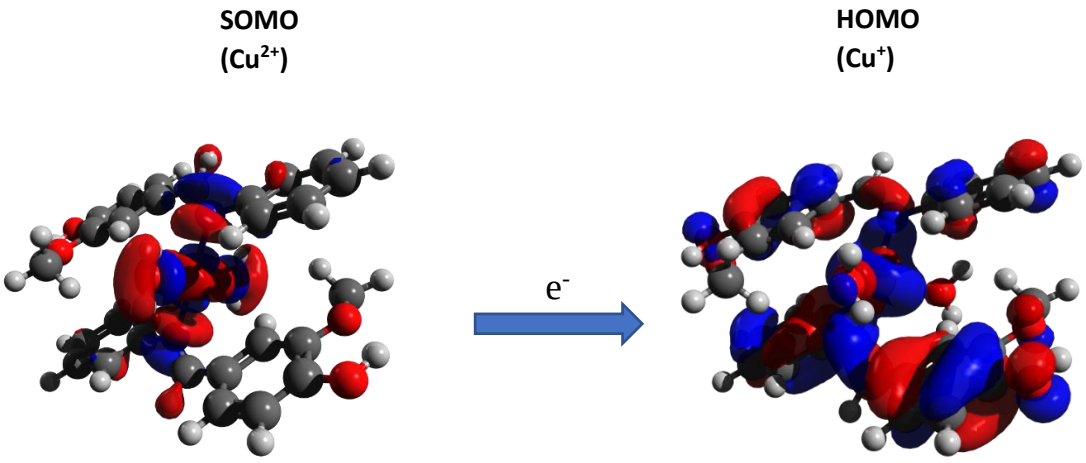

Figure 65 Orbitals involve redox process Cu21

4.5.7.3.2 Molecular Orbitals analysis for redox process in Mn2X complexes

Similar as in copper complexes, the band gap of the **Mn2X** complexes is smaller than the band gap of the ligands and the copper complexes suggesting more reactivity. However, regarding electrophilicity, summarized for **Mn2X** in Table 30. In Mn^{2+} state, **M2X** complexes show less electrophilicity than **Cu2X** complexes (Cu^{2+}) and ligands in its singlet state. This suggest that the manganese complexes in its normal oxidation state are less likely to interact with superoxide anion. Moreover, in its Mn^{3+} state, the electrophilicity is much higher as a cation is formed which would attract more easily species with high electronic density. Interestingly, the difference of electrophilicity between the two oxidation states is about 2.6 eV, which is higher than the differences observe for copper and ligands that show a difference of about 1 eV. Therefore, based on this information and as the complex is in Mn^{2+} state under normal conditions, the beginning of the redox cycle for MnSOD mimetic would be complicated.

As explained previously, the approach of analysis SOD activity using IP to the best of our knowledge has not been applied previously. However, it is important to point that it has been stated that the higher the energy of the HOMO orbital, the obtained SOD activity is lower[112]. In this sense, the energy of HOMO of the **Mn2X** complexes has the order **Mn23**<**Mn22**<**Mn24**<**Mn21.** This turns out to be the same order as obtained using IP as principle to predict the activity, which suggest that using this parameter maybe useful to predict SOD activity, but this should be tested experimentally.

Table 30 Reactivity parameters for Mn2X

Mn2X	HOMO [eV]	LUMO [eV]	Band gap [eV]	η [eV]	μ [eV]	ω [eV]	SOMO [eV]	LUMO [eV]	Band gap [eV]	η [eV]	μ [eV]	ω [eV]
	Mn^{2+}						Mn^{3+}					
Mn21	-6.617	-0.332	6.285	3.143	-3.475	1.921	-7.396	-2.303	5.093	2.547	-4.850	4.618
Mn22	-6.506	-0.258	6.248	3.124	-3.382	1.831	-7.119	-2.284	4.835	2.418	-4.702	4.572
Mn23	-6.474	-0.435	6.039	3.020	-3.455	1.976	-7.393	-2.318	5.075	2.538	-4.856	4.645
Mn24	-6.57	-0.296	6.274	3.137	-3.433	1.878	-7.281	-2.291	4.990	2.495	-4.786	4.590

SOMO Mn^{2+} **LUMO Mn^{3+}**

Mn21 **Mn21**

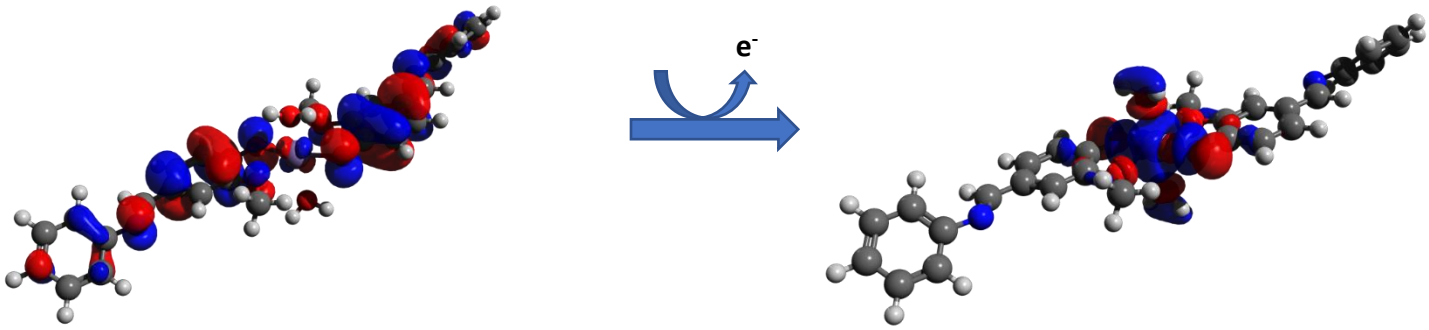

Figure 66 Molecular Orbitals changes in redox process in Mn21

As discussed previously, mesomeric and inductive effect have shown to extremely affect both the molecular orbitals and the reactivity of the compounds[143]. It was found that there are two different behaviors observed regarding molecular orbitals involve in the redox process for manganese complexes. Firstly, **Mn21/Mn22/Mn24** show a similar behavior regarding their frontier orbitals, describe for **Mn21** in Figure 66. The SOMO orbital of the Mn^{2+} in these complexes is distributed over metals and ligands. Upon oxidation, the LUMO in the Mn^{3+} locates on the d_z^2 of the metal and the oxygens in the coordination sphere.

Meanwhile, the frontier molecular orbitals for **Mn23** observed in Figure 67 shows a different kind of electronic distribution for the SOMO of the Mn^{2+}species. Instead of a distribution along the whole molecule, the SOMO is located just in one ligand and in a orbital of the metal. This seems to account for the significant difference in behavior observed for **Mn23**, as the electronic density is less stabilized along the whole molecule, it is more likely that the removal of an electron is easier. Moreover, as the electronic distribution of the orbital changes, it will affect reactivity along the way. However, further studies with other halogens should be made to determine whether these present the same behavior.

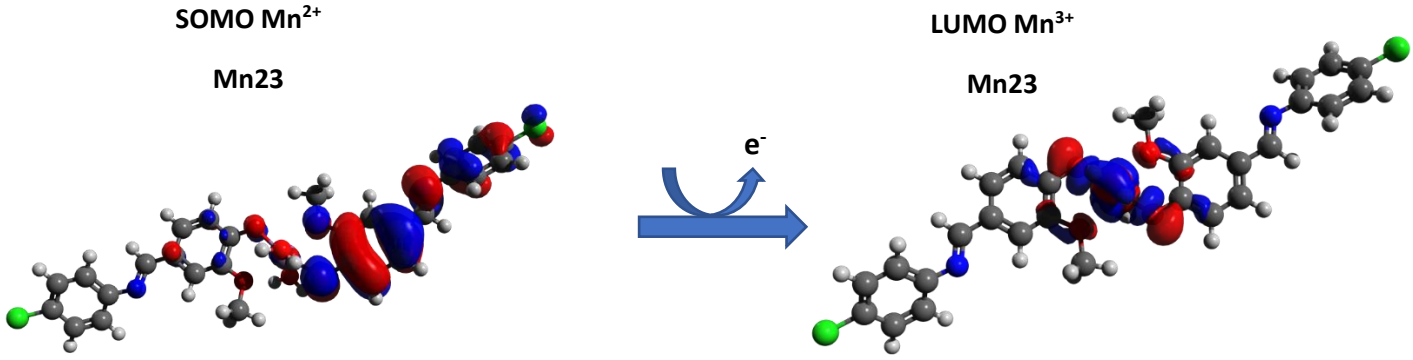

Figure 67 Molecular Orbitals changes in redox process in Mn23

4.6 Final discussion of SOD activity for complexes

Many different complexes have been discussed during this work, therefore, a final discussion of the obtained results divided regarding the metal would be made.

4.6.1 Final discussion of SOD activity for copper complexes

In total during this work, five copper complexes were analyzed, two with **L1** (**Cu1A and Cu1B**) and three with the different ligands of the set **L2X (Cu21, Cu23, Cu24).** Although the ligands have oxygen and nitrogen coordination sites, copper complexes prefer to coordinate through nitrogen. Moreover, almost all the complexes, except **Cu1B** that is octahedral but with elongation in axial positions, are coordinate to four ligands having either distorted tetrahedral or square plane geometries. In general, it is observed that upon reduction of $Cu^{2+} \rightarrow Cu^{1+}$ one or more of the bonds of the complexes tend to break facilitating the access for superoxide anion except for complex **Cu1A** that just show a significant shift in geometry. Regarding the prediction of SOD activity of the complexes, the **Cu2X** complexes are expected to have better SOD performance than the copper complexes with **L1** (**Cu1A and C1B**)

4.6.2 Final discussion SOD activity for manganese complexes

Manganese complexes were only synthetized with ligands of the set L2X obtaining in total four complexes (**Mn21, Mn22, Mn23, Mn24**), all of them present a slightly distorted octahedral geometry. Contrary to copper complexes, manganese prefers the coordination through oxygens of the vanillin part of the ligand. Upon oxidation $Mn^{2+} \rightarrow Mn^{3+}$ there is not break of bonds, rather, just the octahedral geometry becomes more symmetrical (angles and bonds near the ideal values). Finally, regarding SOD activity, IP was used as a parameter use to predict the biological activity of the complexes. In general, the activity is improved in complexes with ligands that have a substituent in the *para* position regardless of its nature as electron donor or acceptor. It is important to point out that a direct comparison between the activity of copper and manganese complexes cannot be made because different properties are being analyzed (IP and EA).

Chapter 5. Conclusions

The laboratory synthesis of five ligands Schiff Bases using vanillin was successfully made through condensation reactions with different amines (ethylenediamine, aniline and its derivatives). The obtained ligands were used to synthetize copper and manganese complexes. For **L1**, only copper complexes with two different L:M ratios, 1:1 and 1:2, were recorded. Using the set of ligands **L2X,** three copper complexes (**Cu2X**) and fours manganese complexes (**Mn2X**) were obtained. The successful synthesis of the compounds was determined upon characterization using FTIR, UV-Vis and in addition for complexes, magnetic susceptibility. The results were used to propose initial geometry structure, charges, and spins for computational calculations.

Experimental IR results proved to be very useful to determine the coordination mode of the complexes, especially for complexes with ligands **L2X**. In this case, the shift of C=N stretching band define whether complexes coordinated through nitrogen or through oxygen (~ 30 cm^{-1} to lower wavenumber for coordination through nitrogen). Moreover, the coordination is confirmed upon the appearance of new peaks in the far-infrared spectrum due to M-O and M-N bands.

Measurements of UV-Vis in solid and liquid state help to better determine whether there were changes in the coordination sphere upon dissolution, which was especially useful for **Mn2X** complexes. As the liquid and solid-state UV-Vis of the complexes significantly differ, labile ligands (chloride) are more likely to be observed in solid state while water/solvent in liquid one.

Finally, magnetic measurements were useful to know the correct charge of metals in the complexes. Copper was found in a 2+ charge (μ_{eff} = ~1,9-2 BM) as well as manganese (μ_{eff} = ~ 6 -6.2 MB) with spins 2 and 6 respectively. This was particularly important for **Cu2X** complexes as its d-d transitions were weak to be easily identify due to its small absorptivity coefficient. Without the magnetic measurements, a confirmation of its 2+ charge was difficult because there is the possibility of having Cu^{1+} since no d-d transitions are observed in this type of species.

The geometries observed for most copper complexes in this work were either distorted tetrahedral or square planar. The complexes adopt these geometries because the orientation and π interactions between the Schiff base ligands limited the space for more ligands. Nevertheless, these geometries are very useful in our case as this helps to resemble the natural coordination mode of copper in CuZn SOD.

Despite small discrepancies, simulation using DFT and TDDFT were able to predict IR frequencies and UV-Vis results with certain level of accuracy. This suggest that the obtained geometry must be close to the real one, nevertheless, effect of counter ions, solvent molecules instead of water molecules as ligands, or -OCH_3 and -OH orientation can bring some differences in the real structure. Moreover, computational calculations were useful for more than just predicting geometry. In this work, different parameters were analyzed to predict SOD activity: geometry changes during redox process, electronic affinity, ionization potential, frontier molecular orbitals and reactivity parameters.

Regarding geometry changes during redox process, in most of the cases, copper complexes show that one or two bonds tend to break upon reduction which is the natural mechanism of Cu-Zn SOD. Meanwhile, in manganese complexes, just slight change in bond and angles is observed as well as for ligands. The breaking of bonds is beneficial as it opens space for the superoxide anion to directly interact with the metal. However, in some complexes, although bonds were broken, there was still not enough space for the anion to interact directly with the metal.

The analysis of frontier orbital molecules was extremely insightful to understand which part of the compounds will be involved during the redox process. For complexes, the metals plays an essential role being the ones through which the electron is donated or received. However, the extra electronic density is easily delocalized along the ligands, at the end this end up being an important factor for the SOD activity. Electron withdrawing groups show to improve the SOD activity for copper and manganese complexes.

Electron affinity and electrophilicity showed to be an important parameter to predict SOD activity in copper complexes, as previously reported in literature. The order of predicted SOD activity was determined, for ligands L23>L21>L24>L22>L1 showing that substitution in the aromatic ring help to improve the SOD activity. Meanwhile for copper complexes, the order is Cu23>Cu21>Cu24> Cu1A> Cu1B base on the capacity to stabilized extra electronic density.

For manganese complexes, although not previously reported, ionization potential seems to be a useful tool to try to determine SOD activity (similar results as analyzing HOMO energy values). The general SOD activity is different compared with the equivalent copper complexes. The SOD activity is expected to be Mn23>Mn22>Mn24>Mn21 being all substitution efficient to improve biological activity.

Chapter 6. Recommendations and future work

Due to the current pandemic, the laboratory accessible hours were limited. For that reason, further characterization of the complexes and ligands using techniques such as EPR, cyclic voltammetry and NMR are recommended to complement the obtained information. Moreover, Job method analysis is recommended for Cu2X and Mn2X complexes as it may coordinates in other modes. Furthermore, as all the complexes were solid, attempts to obtain crystals are suggested to verify the proposed geometries. Finally, it is expected that SOD activity is measured to confirm the prediction. Regarding computational approach, the docking of the complexes with superoxide anion is recommended to complement the discussion made here. Furthermore, the analysis with positions such as ortho or meta should be study as these may not follow the same behavior as the ones of para. Finally, the chase of Mn23 should be further analyzed.

Chapter 7. References

(1) Conry, R. R. Copper: Inorganic & Coordination ChemistryBased in Part on the Article Copper: Inorganic & Coordination Chemistry by Rebecca R. Conry & Kenneth D. Karlin Which Appeared in the Encyclopedia of Inorganic Chemistry, First Edition . In *Encyclopedia of Inorganic Chemistry*; John Wiley & Sons, Ltd: Chichester, UK, 2006. https://doi.org/10.1002/0470862106.ia052.

(2) Modec, B.; Podjed, N.; Lah, N. Beyond the Simple Copper(II) Coordination Chemistry with Quinaldinate and Secondary Amines. *Molecules* **2020**, *25* (7), 1573. https://doi.org/10.3390/molecules25071573.

(3) Ramakrishnan, C.; Geetha, Y. S. Analysis of the Coordination Geometry in Copper Complexes. *Proc. Indian Acad. Sci. - Chem. Sci.* **1990**. https://doi.org/10.1007/BF02867827.

(4) Yu, Q.; Salhi, C. A.; Ambundo, E. A.; Heeg, M. J.; Ochrymowycz, L. A.; Rorabacher, D. B. Direct Evidence for a Geometrically Constrained "Entatic State" Effect on Copper(II/I) Electron-Transfer Kinetics As Manifested in Metastable Intermediates. *J. Am. Chem. Soc.* **2001**, *123* (24), 5720–5729. https://doi.org/10.1021/ja002995r.

(5) Ambundo, E. A.; Deydier, M.-V.; Grall, A. J.; Aguera-Vega, N.; Dressel, L. T.; Cooper, T. H.; Heeg, M. J.; Ochrymowycz, L. A.; Rorabacher, D. B. Influence of Coordination Geometry upon Copper(II/I) Redox Potentials. Physical Parameters for Twelve Copper Tripodal Ligand Complexes. *Inorg. Chem.* **1999**, *38* (19), 4233–4242. https://doi.org/10.1021/ic990334t.

(6) Cuillel, M. The Dual Personality of Ionic Copper in Biology. *J. Incl. Phenom. Macrocycl. Chem.* **2009**, *65* (1–2), 165–170. https://doi.org/10.1007/s10847-009-9636-4.

(7) Tapiero, H.; Townsend, D. M.; Tew, K. D. Trace Elements in Human Physiology and Pathology. Copper. *Biomed. Pharmacother.* **2003**, *57* (9), 386–398. https://doi.org/10.1016/S0753-3322(03)00012-X.

(8) Turski, M. L.; Thiele, D. J. New Roles for Copper Metabolism in Cell Proliferation, Signaling, and Disease. *J. Biol. Chem.* **2009**, *284* (2), 717–721. https://doi.org/10.1074/jbc.R800055200.

(9) Considine, G. Copper (In Biological Systems). In *Van Nostrand's Encyclopedia of Chemistry*; John Wiley & Sons, Inc.: Hoboken, NJ, USA, 2005. https://doi.org/10.1002/0471740039.vec0683.

(10) Osredkar, J. Copper and Zinc, Biological Role and Significance of Copper/Zinc Imbalance. *J. Clin. Toxicol.* **2011**, *s3* (01). https://doi.org/10.4172/2161-0495.S3-001.

(11) Iakovidis, I.; Delimaris, I.; Piperakis, S. M. Copper and Its Complexes in Medicine: A Biochemical Approach. *Mol. Biol. Int.* **2011**, *2011*, 1–13. https://doi.org/10.4061/2011/594529.

(12) Rubino, J. T.; Franz, K. J. Coordination Chemistry of Copper Proteins: How Nature Handles a Toxic Cargo for Essential Function. *J. Inorg. Biochem.* **2012**, *107* (1), 129–143. https://doi.org/10.1016/j.jinorgbio.2011.11.024.

(13) Worrall, J. A. R.; Vijgenboom, E. Copper Mining in Streptomyces: Enzymes, Natural Products and Development. *Nat. Prod. Rep.* **2010**, *27* (5), 742. https://doi.org/10.1039/b804465c.

(14) Solomon, E. I.; Hadt, R. G. Recent Advances in Understanding Blue Copper Proteins. *Coordination*

Chemistry Reviews. 2011. https://doi.org/10.1016/j.ccr.2010.12.008.

(15) Choi, M.; Davidson, V. L. Cupredoxins—A Study of How Proteins May Evolve to Use Metals for Bioenergetic Processes. *Metallomics* **2011**, *3* (2), 140. https://doi.org/10.1039/c0mt00061b.

(16) Flores, M.; Olson, T. L.; Wang, D.; Edwardraja, S.; Shinde, S.; Williams, J. C.; Ghirlanda, G.; Allen, J. P. Copper Environment in Artificial Metalloproteins Probed by Electron Paramagnetic Resonance Spectroscopy. *J. Phys. Chem. B* **2015**, *119* (43), 13825–13833. https://doi.org/10.1021/acs.jpcb.5b04172.

(17) Brouwers, G. J.; Vijgenboom, E.; Corstjens, P. L. A. M.; De Vrind, J. P. M.; De Vrind-De Jong, E. W. Bacterial Mn2+ Oxidizing Systems and Multicopper Oxidases: An Overview of Mechanisms and Functions. *Geomicrobiol. J.* **2000**, *17* (1). https://doi.org/10.1080/014904500270459.

(18) Decker, H.; Dillinger, R.; Tuczek, F. How Does Tyrosinase Work? Recent Insights from Model Chemistry and Structural Biology. *Angew. Chemie Int. Ed.* **2000**, *39* (9), 1591–1595. https://doi.org/10.1002/(SICI)1521-3773(20000502)39:9<1591::AID-ANIE1591>3.0.CO;2-H.

(19) Castiglione, N.; Rinaldo, S.; Giardina, G.; Stelitano, V.; Cutruzzolà, F. Nitrite and Nitrite Reductases: From Molecular Mechanisms to Significance in Human Health and Disease. *Antioxid. Redox Signal.* **2012**, *17* (4), 684–716. https://doi.org/10.1089/ars.2011.4196.

(20) Quintanar, L.; Stoj, C.; Taylor, A. B.; Hart, P. J.; Kosman, D. J.; Solomon, E. I. Shall We Dance? How A Multicopper Oxidase Chooses Its Electron Transfer Partner. *Acc. Chem. Res.* **2007**, *40* (6), 445–452. https://doi.org/10.1021/ar600051a.

(21) Solomon, E. I.; Randall, D. W.; Glaser, T. Electronic Structures of Active Sites in Electron Transfer Metalloproteins: Contributions to Reactivity. *Coord. Chem. Rev.* **2000**, *200–202*, 595–632. https://doi.org/10.1016/S0010-8545(00)00332-5.

(22) Gorelsky, S. I.; Ghosh, S.; Solomon, E. I. Mechanism of N 2 O Reduction by the μ 4 -S Tetranuclear Cu Z Cluster of Nitrous Oxide Reductase. *J. Am. Chem. Soc.* **2006**, *128* (1), 278–290. https://doi.org/10.1021/ja055856o.

(23) Solomon, E. I.; Heppner, D. E.; Johnston, E. M.; Ginsbach, J. W.; Cirera, J.; Qayyum, M.; Kieber-Emmons, M. T.; Kjaergaard, C. H.; Hadt, R. G.; Tian, L. Copper Active Sites in Biology. *Chemical Reviews*. 2014. https://doi.org/10.1021/cr400327t.

(24) Olsen, S.; Tangstad, M.; Lindstad, T. *Production of Manganese Ferroalloys*; Tapir Academic Press: Trondheim, 2007.

(25) *Manganese in Soils and Plants*; Graham, R. D., Hannam, R. J., Uren, N. C., Eds.; Springer Netherlands: Dordrecht, 1988. https://doi.org/10.1007/978-94-009-2817-6.

(26) Hosseiny, A.; Mackie, A. G.; McAuliffe, C. A.; Minten, K. The Coordination Chemistry of Manganese. *Inorganica Chim. Acta* **1981**, *49*, 99–105. https://doi.org/10.1016/S0020-1693(00)90464-X.

(27) *Comprehensive Coordination Chemistry II*; Constable, E., McCleverty, J., Meyer, T., Eds.; Elsevier Science, 2003.

(28) Collomb, M.-N.; Deronzier, A. Manganese: Inorganic & Coordination ChemistryBased in Part on the Article Manganese: Inorganic & Coordination Chemistry by Charles A. McAuliffe, Stephen M.

Godfrey, & Michael Watkinson Which Appeared in the Encyclopedia of Inorganic Chemistry, First Editi. In *Encyclopedia of Inorganic Chemistry*; John Wiley & Sons, Ltd: Chichester, UK, 2006. https://doi.org/10.1002/0470862106.ia126.

(29) Sridharan, K. Electronic Spectroscopy. In *Spectral Methods in Transition Metal Complexes*; Elsevier, 2016; pp 13–67. https://doi.org/10.1016/B978-0-12-809591-1.00002-5.

(30) Zhou, Q.; Dolgov, L.; Srivastava, A. M.; Zhou, L.; Wang, Z.; Shi, J.; Dramićanin, M. D.; Brik, M. G.; Wu, M. Mn 2+ and Mn 4+ Red Phosphors: Synthesis, Luminescence and Applications in WLEDs. A Review. *J. Mater. Chem. C* **2018**, *6* (11), 2652–2671. https://doi.org/10.1039/C8TC00251G.

(31) Yamaguchi, K. S.; Sawyer, D. T. The Redox Chemistry of Manganese(III) and -(IV) Complexes. *Isr. J. Chem.* **1985**, *25* (2), 164–176. https://doi.org/10.1002/ijch.198500026.

(32) Lingappa, U. F.; Monteverde, D. R.; Magyar, J. S.; Valentine, J. S.; Fischer, W. W. How Manganese Empowered Life with Dioxygen (and Vice Versa). *Free Radic. Biol. Med.* **2019**, *140*, 113–125. https://doi.org/10.1016/j.freeradbiomed.2019.01.036.

(33) Li, L.; Yang, X. The Essential Element Manganese, Oxidative Stress, and Metabolic Diseases: Links and Interactions. *Oxid. Med. Cell. Longev.* **2018**, *2018*, 1–11. https://doi.org/10.1155/2018/7580707.

(34) Salomon, E.; Keren, N.; Kanteev, M.; Adir, N. Manganese in Biological Systems: Transport and Function. In *PATAI'S Chemistry of Functional Groups*; John Wiley & Sons, Ltd: Chichester, UK, 2011. https://doi.org/10.1002/9780470682531.pat0540.

(35) Schmidt; Husted. The Biochemical Properties of Manganese in Plants. *Plants* **2019**, *8* (10), 381. https://doi.org/10.3390/plants8100381.

(36) Pfalzer, A. C.; Bowman, A. B. Relationships Between Essential Manganese Biology and Manganese Toxicity in Neurological Disease. *Curr. Environ. Heal. Reports* **2017**, *4* (2), 223–228. https://doi.org/10.1007/s40572-017-0136-1.

(37) Martinez-Finley, E. J.; Chakraborty, S.; Aschner, M. Manganese in Biological Systems. In *Encyclopedia of Metalloproteins*; Springer New York: New York, NY, 2013; pp 1297–1303. https://doi.org/10.1007/978-1-4614-1533-6_284.

(38) Bowler, R. P.; Barnes, P. J.; Crapo, J. D. The Role of Oxidative Stress in Chronic Obstructive Pulmonary Disease. *COPD J. Chronic Obstr. Pulm. Dis.* **2004**, *1* (2), 255–277. https://doi.org/10.1081/COPD-200027031.

(39) Hasanuzzaman, M.; Bhuyan, M. H. M. B.; Zulfiqar, F.; Raza, A.; Mohsin, S. M.; Mahmud, J. Al; Fujita, M.; Fotopoulos, V. Reactive Oxygen Species and Antioxidant Defense in Plants under Abiotic Stress: Revisiting the Crucial Role of a Universal Defense Regulator. *Antioxidants* **2020**, *9* (8), 681. https://doi.org/10.3390/antiox9080681.

(40) Moloney, J. N.; Cotter, T. G. ROS Signalling in the Biology of Cancer. *Semin. Cell Dev. Biol.* **2018**, *80*, 50–64. https://doi.org/10.1016/j.semcdb.2017.05.023.

(41) Patel, R.; Rinker, L.; Peng, J.; Chilian, W. M. Reactive Oxygen Species: The Good and the Bad. In *Reactive Oxygen Species (ROS) in Living Cells*; InTech, 2018. https://doi.org/10.5772/intechopen.71547.

(42) Ozcan, A.; Ogun, M. Biochemistry of Reactive Oxygen and Nitrogen Species. In *Basic Principles and Clinical Significance of Oxidative Stress*; InTech, 2015. https://doi.org/10.5772/61193.

(43) Redza-Dutordoir, M.; Averill-Bates, D. A. Activation of Apoptosis Signalling Pathways by Reactive Oxygen Species. *Biochim. Biophys. Acta - Mol. Cell Res.* **2016**, *1863* (12), 2977–2992. https://doi.org/10.1016/j.bbamcr.2016.09.012.

(44) Sharma, P.; Jha, A. B.; Dubey, R. S.; Pessarakli, M. Reactive Oxygen Species, Oxidative Damage, and Antioxidative Defense Mechanism in Plants under Stressful Conditions. *J. Bot.* **2012**, *2012*, 1–26. https://doi.org/10.1155/2012/217037.

(45) Ray, P. D.; Huang, B. W.; Tsuji, Y. Reactive Oxygen Species (ROS) Homeostasis and Redox Regulation in Cellular Signaling. *Cellular Signalling*. 2012. https://doi.org/10.1016/j.cellsig.2012.01.008.

(46) Schieber, M.; Chandel, N. S. ROS Function in Redox Signaling and Oxidative Stress. *Curr. Biol.* **2014**, *24* (10), R453–R462. https://doi.org/10.1016/j.cub.2014.03.034.

(47) Reczek, C. R.; Chandel, N. S. ROS-Dependent Signal Transduction. *Curr. Opin. Cell Biol.* **2015**, *33*, 8–13. https://doi.org/10.1016/j.ceb.2014.09.010.

(48) Callaway, D. A.; Jiang, J. X. Reactive Oxygen Species and Oxidative Stress in Osteoclastogenesis, Skeletal Aging and Bone Diseases. *J. Bone Miner. Metab.* **2015**, *33* (4), 359–370. https://doi.org/10.1007/s00774-015-0656-4.

(49) Wang, Y.; Branicky, R.; Noë, A.; Hekimi, S. Superoxide Dismutases: Dual Roles in Controlling ROS Damage and Regulating ROS Signaling. *J. Cell Biol.* **2018**, *217* (6), 1915–1928. https://doi.org/10.1083/jcb.201708007.

(50) Johnson, F.; Giulivi, C. Superoxide Dismutases and Their Impact upon Human Health. *Mol. Aspects Med.* **2005**, *26* (4–5), 340–352. https://doi.org/10.1016/j.mam.2005.07.006.

(51) Rakhit, R.; Chakrabartty, A. Structure, Folding, and Misfolding of Cu,Zn Superoxide Dismutase in Amyotrophic Lateral Sclerosis. *Biochimica et Biophysica Acta - Molecular Basis of Disease*. 2006. https://doi.org/10.1016/j.bbadis.2006.05.004.

(52) Campos-Shimada, L. B.; Hideo Gilglioni, E.; Fernandes Garcia, R.; Rizato Martins-Maciel, E.; Luiza Ishii-Iwamoto, E.; Luzia Salgueiro-Pagadigorria, C. Superoxide Dismutase: A Review and a Modified Protocol for Activities Measurements in Rat Livers. *Archives of Physiology and Biochemistry*. 2018. https://doi.org/10.1080/13813455.2018.1520891.

(53) Abreu, I. A.; Cabelli, D. E. Superoxide Dismutases-a Review of the Metal-Associated Mechanistic Variations. *Biochimica et Biophysica Acta - Proteins and Proteomics*. 2010. https://doi.org/10.1016/j.bbapap.2009.11.005.

(54) Mondola, P.; Damiano, S.; Sasso, A.; Santillo, M. The Cu, Zn Superoxide Dismutase: Not Only a Dismutase Enzyme. *Front. Physiol.* **2016**. https://doi.org/10.3389/fphys.2016.00594.

(55) Stephenie, S.; Chang, Y. P.; Gnanasekaran, A.; Esa, N. M.; Gnanaraj, C. An Insight on Superoxide Dismutase (SOD) from Plants for Mammalian Health Enhancement. *Journal of Functional Foods*. 2020. https://doi.org/10.1016/j.jff.2020.103917.

(56) Miller, A. F. Superoxide Dismutases: Ancient Enzymes and New Insights. *FEBS Letters*. 2012.

https://doi.org/10.1016/j.febslet.2011.10.048.

(57) Miller, A. F. Superoxide Dismutases: Active Sites That Save, but a Protein That Kills. *Current Opinion in Chemical Biology*. 2004. https://doi.org/10.1016/j.cbpa.2004.02.011.

(58) Quist, D. A.; Diaz, D. E.; Liu, J. J.; Karlin, K. D. Activation of Dioxygen by Copper Metalloproteins and Insights from Model Complexes. *Journal of Biological Inorganic Chemistry*. 2017. https://doi.org/10.1007/s00775-016-1415-2.

(59) Bordo, D.; Pesce, A.; Bolognesi, M.; Elena Stroppolo, M.; Falconi, M.; Desideri, A. Copper-Zinc Superoxide Dismutase in Prokaryotes and Eukaryotes. In *Encyclopedia of Inorganic and Bioinorganic Chemistry*; 2011. https://doi.org/10.1002/9781119951438.eibc0621.

(60) Valentine, J. S.; De Freitas, D. M. Copper-Zinc Superoxide Dismutase: A Unique Biological "Ligand" for Bioinorganic Studies. *J. Chem. Educ.* **1985**. https://doi.org/10.1021/ed062p990.

(61) Zhu, W.; Richards, N. G. J. Biological Functions Controlled by Manganese Redox Changes in Mononuclear Mn-Dependent Enzymes. *Essays Biochem.* **2017**, *61* (2), 259–270. https://doi.org/10.1042/EBC20160070.

(62) Kitada, M.; Xu, J.; Ogura, Y.; Monno, I.; Koya, D. Manganese Superoxide Dismutase Dysfunction and the Pathogenesis of Kidney Disease. *Front. Physiol.* **2020**, *11*. https://doi.org/10.3389/fphys.2020.00755.

(63) Azadmanesh, J.; Borgstahl, G. A Review of the Catalytic Mechanism of Human Manganese Superoxide Dismutase. *Antioxidants* **2018**, *7* (2), 25. https://doi.org/10.3390/antiox7020025.

(64) Carillon, J.; Rouanet, J.-M.; Cristol, J.-P.; Brion, R. Superoxide Dismutase Administration, A Potential Therapy Against Oxidative Stress Related Diseases: Several Routes of Supplementation and Proposal of an Original Mechanism of Action. *Pharm. Res.* **2013**, *30* (11), 2718–2728. https://doi.org/10.1007/s11095-013-1113-5.

(65) Khalid, H.; Hanif, M.; Hashmi, M.; Mahmood, T.; Ayub, K.; Monim-ul-Mehboob, M. Copper Complexes of Bioactive Ligands with Superoxide Dismutase Activity. *Mini-Reviews Med. Chem.* **2013**, *13* (13), 1944–1956. https://doi.org/10.2174/13895575113136660092.

(66) Puchoňová, M.; Švorec, J.; Švorc, L.; Valigura, D. SOD Mimetic Activity of Salicylatocopper Complexes. *Chem. Pap.* **2016**, *70* (1), 75–81. https://doi.org/10.1515/chempap-2015-0167.

(67) Batinić-Haberle, I.; Rebouças, J. S.; Spasojević, I. Superoxide Dismutase Mimics: Chemistry, Pharmacology, and Therapeutic Potential. *Antioxid. Redox Signal.* **2010**, *13* (6), 877–918. https://doi.org/10.1089/ars.2009.2876.

(68) Erxleben, A. Transition Metal Salen Complexes in Bioinorganic and Medicinal Chemistry. *Inorganica Chim. Acta* **2018**, *472*, 40–57. https://doi.org/10.1016/j.ica.2017.06.060.

(69) Bixenmann, L.; He, J.; Liang, M.; Tremel, W. Functional Superoxide Dismutase Mimics Become Diverse: From Simple Compounds on Prebiotic Earth to Nanozymes. *Prog. Biochem. Biophys.* **2018**. https://doi.org/10.16476/j.pibb.2018.0040.

(70) Iranzo, O. Manganese Complexes Displaying Superoxide Dismutase Activity: A Balance between Different Factors. *Bioorg. Chem.* **2011**, *39* (2), 73–87. https://doi.org/10.1016/j.bioorg.2011.02.001.

(71) Savithri, K.; Kumar, B. C. V.; Vivek, H. K.; Revanasiddappa, H. D. Synthesis and Characterization of Cobalt(III) and Copper(II) Complexes of 2-((E)-(6-Fluorobenzo[d]Thiazol-2-Ylimino) Methyl)-4-Chlorophenol: DNA Binding and Nuclease Studies—SOD and Antimicrobial Activities. *Int. J. Spectrosc.* **2018**, *2018*, 1–15. https://doi.org/10.1155/2018/8759372.

(72) Patel, R. N.; Patel, S. K.; Kumhar, D.; Patel, N.; Patel, A. K.; Jadeja, R. N.; Patel, N.; Butcher, R. J.; Cortijo, M.; Herrero, S. Two New Copper(II) Binuclear Complexes with 2-[(E)-(Pyridine-2yl-Hydrazono)Methyl]Phenol: Molecular Structures, Quantum Chemical Calculations, Cryomagnetic Properties and Catalytic Activity. *Polyhedron* **2020**, *188*, 114687. https://doi.org/10.1016/j.poly.2020.114687.

(73) Siqueira, J. D.; de Pellegrin, S. F.; dos Santos, S. S.; Iglesias, B. A.; Piquini, P. C.; Arantes, L. P.; Soares, F. A.; Chaves, O. A.; Neves, A.; Back, D. F. SOD Activity of New Copper II Complexes with Ligands Derived from Pyridoxal and Toxicity in Caenorhabditis Elegans. *J. Inorg. Biochem.* **2020**, *204*. https://doi.org/10.1016/j.jinorgbio.2019.110950.

(74) González-Baró, A. C.; Pis-Diez, R.; Franca, C. A.; Torre, M. H.; Parajón-Costa, B. S. Physicochemical Characterization of Cu(II) Complexes with SOD-like Activity, Theoretical Studies and Biological Assays. *Polyhedron* **2010**, *29* (3), 959–968. https://doi.org/10.1016/j.poly.2009.11.015.

(75) Tabassum, S.; Amir, S.; Arjmand, F.; Pettinari, C.; Marchetti, F.; Masciocchi, N.; Lupidi, G.; Pettinari, R. Mixed-Ligand Cu(II)–Vanillin Schiff Base Complexes; Effect of Coligands on Their DNA Binding, DNA Cleavage, SOD Mimetic and Anticancer Activity. *Eur. J. Med. Chem.* **2013**, *60*, 216–232. https://doi.org/10.1016/j.ejmech.2012.08.019.

(76) Tabassum, S.; Asim, A.; Khan, R. A.; Arjmand, F.; Rajakumar, D.; Balaji, P.; Akbarsha, M. A. A Multifunctional Molecular Entity Cu II –Sn IV Heterobimetallic Complex as a Potential Cancer Chemotherapeutic Agent: DNA Binding/Cleavage, SOD Mimetic, Topoisomerase Iα Inhibitory and in Vitro Cytotoxic Activities. *RSC Adv.* **2015**, *5* (59), 47439–47450. https://doi.org/10.1039/C5RA07333B.

(77) Afsan, Z.; Roisnel, T.; Tabassum, S.; Arjmand, F. Spectroscopic and Single-Crystal X-Ray Diffraction Studies of Enantiomeric Copper(II) Schiff Base One-Dimensional Coordination Polymers with 4-(2-Aminoethyl)Benzenesulfonamide Appendage: Comprehensive Biological Evaluation (DNA Binding, Cleavage, Superoxi. *Appl. Organomet. Chem.* **2019**, *33* (7). https://doi.org/10.1002/aoc.4958.

(78) Dong, J.; Gao, L.; Zhao, P.; Zhang, B.; Wang, L.; Kong, J.; Li, L. A Chiral Binuclear Nickel(II) Complex with Schiff Base Ligand: Synthesis, Crystal Structure, DNA/BSA Binding Interactions and SOD Activity. *Transit. Met. Chem.* **2020**, *45* (6), 381–390. https://doi.org/10.1007/s11243-020-00390-z.

(79) Rouco, L.; González-Noya, A. M.; Pedrido, R.; Maneiro, M. Pursuing the Elixir of Life: In Vivo Antioxidative Effects of Manganosalen Complexes. *Antioxidants* **2020**, *9* (8), 727. https://doi.org/10.3390/antiox9080727.

(80) Joseph, J.; Rani, G. A. B. Metal-Based Molecular Design Tuning Biochemical Behavior: Synthesis, Characterization, and Biochemical Studies of Mixed Ligand Complexes Derived From 4-Aminoantipyrine Derivatives. *Spectrosc. Lett.* **2014**, *47* (2), 86–100. https://doi.org/10.1080/00387010.2013.776087.

(81) Pereira, M. B.; Fontana, L. A.; Siqueira, J. D.; Auras, B. L.; da Silva, M. P.; Neves, A.; Gabriel, P.;

Terenzi, H.; Iglesias, B. A.; Back, D. F. Pyridoxal Derivatized Copper(II) Complexes: Evaluation of Antioxidant, Catecholase, and DNA Cleavage Activity. *Inorganica Chim. Acta* **2018**, *469*, 561–575. https://doi.org/10.1016/j.ica.2017.09.063.

(82) Sangeeta, S.; Ahmad, K.; Noorussabah, N.; Bharti, S.; Mishra, M. K.; Sharma, S. R.; Choudhary, M. Synthesis, Characterization, Crystal Structure, Superoxide Dismutase and Biological Activities of Nickel (II) Complexes with Bidentate Ligands Possessing N and O Donor Atoms. *J. Mol. Struct.* **2017**, *1149*, 183–195. https://doi.org/10.1016/j.molstruc.2017.07.059.

(83) Mohan, B.; Jana, A.; Das, N.; Bharti, S.; Choudhary, M. Syntheses, Crystal Structures, Antioxidant SOD-like Properties and in-Vitro Antimicrobial Studies of Cu(II) and Ni (II) Complexes with 2-((E)-(4-Bromo-2-Chlorophenylimino) Methyl)-6-Bromo-4-Nitrophenol and (E)-1-(3, 5-Dichloro-2-Hydroxybenzylidene)-4,. *J. Mol. Struct.* **2018**, *1171*, 94–109. https://doi.org/10.1016/j.molstruc.2018.06.016.

(84) Hanwell, M. D.; Curtis, D. E.; Lonie, D. C.; Vandermeersch, T.; Zurek, E.; Hutchison, G. R. Avogadro: An Advanced Semantic Chemical Editor, Visualization, and Analysis Platform. *J. Cheminform.* **2012**, *4* (1), 17. https://doi.org/10.1186/1758-2946-4-17.

(85) Neese, F.; Wennmohs, F.; Becker, U.; Riplinger, C. The ORCA Quantum Chemistry Program Package. *J. Chem. Phys.* **2020**, *152* (22), 224108. https://doi.org/10.1063/5.0004608.

(86) Neese, F. Software Update: The ORCA Program System, Version 4.0. *WIREs Comput. Mol. Sci.* **2018**, *8* (1). https://doi.org/10.1002/wcms.1327.

(87) Neese, F. The ORCA Program System. *WIREs Comput. Mol. Sci.* **2012**, *2* (1), 73–78. https://doi.org/10.1002/wcms.81.

(88) Geerlings, P.; De Proft, F.; Langenaeker, W. Conceptual Density Functional Theory. *Chem. Rev.* **2003**, *103* (5), 1793–1874. https://doi.org/10.1021/cr990029p.

(89) Ramachandran, K.; Deepa, G.; Namboori, K. *Computational Chemistry and Molecular Modeling*; Springer Berlin Heidelberg: Berlin, Heidelberg, 2008. https://doi.org/10.1007/978-3-540-77304-7.

(90) Tsuneda, T. *Density Functional Theory in Quantum Chemistry*; Springer Japan: Tokyo, 2014. https://doi.org/10.1007/978-4-431-54825-6.

(91) Anslyn, E.; Dougherty, D. *Modern Physical Organic Chemistry*; Murdzek, J., Ed.; University Science Books: Sausalito, United States of America, 2006.

(92) *Density-Functional Methods for Excited States*; Ferré, N., Filatov, M., Huix-Rotllant, M., Eds.; Topics in Current Chemistry; Springer International Publishing: Cham, 2016; Vol. 368. https://doi.org/10.1007/978-3-319-22081-9.

(93) Ullrich, C. *Time-Dependent Density-Functional Theory Concepts and Applications*; Oxford University Press: United States of America, 2016.

(94) *Fundamentals of Time-Dependent Density Functional Theory*; Marques, M. A. L., Maitra, N. T., Nogueira, F. M. S., Gross, E. K. U., Rubio, A., Eds.; Lecture Notes in Physics; Springer Berlin Heidelberg: Berlin, Heidelberg, 2012; Vol. 837. https://doi.org/10.1007/978-3-642-23518-4.

(95) *Encyclopedia of Spectroscopy and Spectrometry*; Lindon, J., Tranter, G., Koppenaal, D., Eds.; Elsevier, 2017.

(96) *Quantum Simulations of Materials and Biological Systems*; Zeng, J., Zhang, R.-Q., Treutlein, H. R., Eds.; Springer Netherlands: Dordrecht, 2012. https://doi.org/10.1007/978-94-007-4948-1.

(97) Ramachandran, K.; Namboori, K.; Deepa, G. Basis Sets. In *Computational Chemistry and Molecular Modeling*; Springer Berlin Heidelberg: Berlin, Heidelberg; pp 115–138. https://doi.org/10.1007/978-3-540-77304-7_6.

(98) Zheng, J.; Xu, X.; Truhlar, D. G. Minimally Augmented Karlsruhe Basis Sets. *Theor. Chem. Acc.* **2011**, *128* (3), 295–305. https://doi.org/10.1007/s00214-010-0846-z.

(99) Hill, J. G. Gaussian Basis Sets for Molecular Applications. *Int. J. Quantum Chem.* **2013**, *113* (1), 21–34. https://doi.org/10.1002/qua.24355.

(100) Xu, X.; Truhlar, D. G. Performance of Effective Core Potentials for Density Functional Calculations on 3d Transition Metals. *J. Chem. Theory Comput.* **2012**, *8* (1), 80–90. https://doi.org/10.1021/ct200558j.

(101) Yanai, T.; Tew, D. P.; Handy, N. C. A New Hybrid Exchange–Correlation Functional Using the Coulomb-Attenuating Method (CAM-B3LYP). *Chem. Phys. Lett.* **2004**, *393* (1–3), 51–57. https://doi.org/10.1016/j.cplett.2004.06.011.

(102) Kim, K.; Jordan, K. D. Comparison of Density Functional and MP2 Calculations on the Water Monomer and Dimer. *J. Phys. Chem.* **1994**, *98* (40), 10089–10094. https://doi.org/10.1021/j100091a024.

(103) Höfener, S.; Trumm, M.; Koke, C.; Heuser, J.; Ekström, U.; Skerencak-Frech, A.; Schimmelpfennig, B.; Panak, P. J. Computing UV/Vis Spectra Using a Combined Molecular Dynamics and Quantum Chemistry Approach: Bis-Triazin-Pyridine (BTP) Ligands Studied in Solution. *Phys. Chem. Chem. Phys.* **2016**, *18* (11), 7728–7736. https://doi.org/10.1039/C5CP07540H.

(104) Zara, Z.; Iqbal, J.; Ayub, K.; Irfan, M.; Mahmood, A.; Khera, R. A.; Eliasson, B. A Comparative Study of DFT Calculated and Experimental UV/Visible Spectra for Thirty Carboline and Carbazole Based Compounds. *J. Mol. Struct.* **2017**, *1149*, 282–298. https://doi.org/10.1016/j.molstruc.2017.07.093.

(105) Jacquemin, D.; Perpète, E. A.; Scuseria, G. E.; Ciofini, I.; Adamo, C. TD-DFT Performance for the Visible Absorption Spectra of Organic Dyes: Conventional versus Long-Range Hybrids. *J. Chem. Theory Comput.* **2008**, *4* (1), 123–135. https://doi.org/10.1021/ct700187z.

(106) Steinmann, S. N.; Corminboeuf, C. Comprehensive Benchmarking of a Density-Dependent Dispersion Correction. *J. Chem. Theory Comput.* **2011**, *7* (11), 3567–3577. https://doi.org/10.1021/ct200602x.

(107) Gonnella, N. C. *LC-NMR*; CRC Press, 2020. https://doi.org/10.1201/9781351023740.

(108) Dhanaraj, C. J.; Johnson, J. Studies on Some Metal Complexes of a Quinoxaline Based Unsymmetrical ONNO Donor Ligand. *J. Therm. Anal. Calorim.* **2017**, *127* (2), 1845–1862. https://doi.org/10.1007/s10973-016-5953-1.

(109) Świderski, G.; Jabłońska-Trypuć, A.; Kalinowska, M.; Świsłocka, R.; Karpowicz, D.; Magnuszewska, M.; Lewandowski, W. Spectroscopic, Theoretical and Antioxidant Study of 3d-Transition Metals (Co(II), Ni(II), Cu(II), Zn(II)) Complexes with Cichoric Acid. *Materials (Basel).* **2020**, *13* (14), 3102. https://doi.org/10.3390/ma13143102.

(110) Suksrichavalit, T.; Prachayasittikul, S.; Nantasenamat, C.; Isarankura-Na-Ayudhya, C.; Prachayasittikul, V. Copper Complexes of Pyridine Derivatives with Superoxide Scavenging and Antimicrobial Activities. *Eur. J. Med. Chem.* **2009**, *44* (8), 3259–3265. https://doi.org/10.1016/j.ejmech.2009.03.033.

(111) Suksrichavalit, T.; Prachayasittikul, S.; Piacham, T.; Isarankura-Na-Ayudhya, C.; Nantasenamat, C.; Prachayasittikul, V. Copper Complexes of Nicotinic-Aromatic Carboxylic Acids as Superoxide Dismutase Mimetics. *Molecules* **2008**, *13* (12), 3040–3056. https://doi.org/10.3390/molecules13123040.

(112) da Silva, T. U.; Pougy, K. de C.; da Silva, E. T.; Lima, C. H. da S.; Machado, S. de P. Electronic Investigation of the Effect of Substituents on the SOD Mimic Activity of Copper (II) Complexes with 8-Hydroxyquinoline-Derived Ligands. *J. Inorg. Biochem.* **2021**, *217*, 111359. https://doi.org/10.1016/j.jinorgbio.2021.111359.

(113) Lu, Q.; Li, X.; Wang, Y.; Chen, G. Catalytic Activities of Dismution Reactions of Cu(Bpy)Br2 Compound and Its Derivatives as SOD Mimics: A Theoretical Study. *J. Mol. Model.* **2009**, *15* (11), 1397–1405. https://doi.org/10.1007/s00894-009-0505-2.

(114) da Silva, T. U.; da Silva, E. T.; Lima, C. H. da S.; Machado, S. de P. Theoretical Study of Binuclear Cu-M Complexes (M = Zn, Cu, Ni) with p-Xylylene-Bridged-Bis(1,4,7-Triazacyclononane) Ligands: Possible CuZnSOD Mimics. *Inorganica Chim. Acta* **2020**, *501*, 119232. https://doi.org/10.1016/j.ica.2019.119232.

(115) Dineshkumar, S.; Muthusamy, A.; Chandrasekaran, J. Temperature and Frequency Dependent Dielectric Properties of Electrically Conducting Oxidatively Synthesized Polyazomethines and Their Structural, Optical, and Thermal Characterizations. *J. Mol. Struct.* **2017**, *1128*, 730–740. https://doi.org/10.1016/j.molstruc.2016.09.051.

(116) Hijas, K. M.; Madan Kumar, S.; Byrappa, K.; Geethakrishnan, T.; Jeyaram, S.; Nagalakshmi, R. Spectroscopic Investigations Using Density Functional Theory on 2-Methoxy-4(Phenyliminomethyl)Phenol: A Non Linear Optical Material. *J. Mol. Struct.* **2018**, *1155*, 249–259. https://doi.org/10.1016/j.molstruc.2017.11.001.

(117) Tufa, A.; Endale, M.; Desalegn, T. Synthesis, Characterization and Antibacterial Activity of Copper(II) and Cobalt(II) Vanillin-Aniline Schiff Base Complexes. *IISTE, Chem. Mater. Res.* **2018**, *10*, 38–45. https://doi.org/ISSN (Paper)2224-3224 ISSN (Online)2225-0956.

(118) Alecu, I. M.; Zheng, J.; Zhao, Y.; Truhlar, D. G. Computational Thermochemistry: Scale Factor Databases and Scale Factors for Vibrational Frequencies Obtained from Electronic Model Chemistries. *J. Chem. Theory Comput.* **2010**, *6* (9), 2872–2887. https://doi.org/10.1021/ct100326h.

(119) Kazuo, N. *Infrared and Raman Spectra of Inorganic and Coordination Compounds Part A: Theory and Applications in Inorganic Chemistry*, Sixth.; Wiley: Hoboken, NJ, USA, 2009.

(120) Donal, P.; Gary, L.; George, K.; James, V. *Introduction to Spectroscopy*, fith.; Cengace learning: Stamford, 2015.

(121) Mishra, D. K.; Singha, U. K.; Das, A.; Dutta, S.; Kar, P.; Chakraborty, A.; Sen, A.; Sinha, B. DNA Binding, Amelioration of Oxidative Stress, and Molecular Docking Study of Zn(II) Metal Complex of a New Schiff Base Ligand. *J. Coord. Chem.* **2018**, *71* (14), 2165–2182.

https://doi.org/10.1080/00958972.2018.1476687.

(122) Tanak, H.; Semiz, L.; Koçak, F.; Ağar, A. A.; Özdemir, N. Molecular Structure, Spectroscopic and Density Functional Studies on 2-{[(5-Nitrothiophen-2-Yl)Methylidene]Amino}phenol. *Optik (Stuttg).* **2019**, *195*, 163144. https://doi.org/10.1016/j.ijleo.2019.163144.

(123) Gonciarz, A.; Żuber, M.; Zwoździak, J. Spectrochemical Properties and Solvatochromism of Tetradentate Schiff Base Complex with Nickel: Calculations and Experiments. *ChemistryOpen* **2018**, *7* (9), 677–687. https://doi.org/10.1002/open.201800100.

(124) Acar, N.; Selçuki, C.; Coşkun, E. DFT and TDDFT Investigation of the Schiff Base Formed by Tacrine and Saccharin. *J. Mol. Model.* **2017**, *23* (1), 17. https://doi.org/10.1007/s00894-016-3195-6.

(125) Vitnik, V. D.; Vitnik, Ž. J.; Božić, B. Đ.; Valentić, N. V.; Dilber, S. P.; Mijin, D. Ž.; Ušćumlić, G. S. Experimental and Theoretical Insight into the Electronic Properties of 4-Aryl-5-Arylazo-3-Cyano-6-Hydroxy-2-Pyridone Dyes. *Color. Technol.* **2017**, *133* (3), 223–233. https://doi.org/10.1111/cote.12271.

(126) Pisani, P.; Caporuscio, F.; Carlino, L.; Rastelli, G. Molecular Dynamics Simulations and Classical Multidimensional Scaling Unveil New Metastable States in the Conformational Landscape of CDK2. *PLoS One* **2016**, *11* (4), e0154066. https://doi.org/10.1371/journal.pone.0154066.

(127) Lippard, S. J.; Berg, J. M. Physical Methods in Bioinorganic Chemistry. *Princ. Bioinorg. Chem.* **1994**. https://doi.org/10.1021/ja004754p.

(128) Ho, T.-L. *Hard and Soft Acids and Bases Principle in Organic Chemistry*; Academic Press: New York, 1977.

(129) Services, U. S. D. of health and H. *Enviromental Health Perspectives*, Volume 54.; Lucier, G., Hook, G., Eds.; United States Government Printing Office: United States of America, 1984.

(130) Cowan, J. *Inorganic Biochemistry: An Introduction*, Second.; Wiley-VCH: New York, 1997.

(131) Szczęsny, R.; Szłyk, E.; Kozakiewicz, A.; Dobrzańska, L. Thermal and Structural Characterization of Copper(II) Complexes with Phenyl-2-Pyridylketoxime (HPPK). *J. Therm. Anal. Calorim.* **2017**, *128* (3), 1591–1599. https://doi.org/10.1007/s10973-016-5956-y.

(132) Tabbì, G.; Giuffrida, A.; Bonomo, R. P. Determination of Formal Redox Potentials in Aqueous Solution of Copper(II) Complexes with Ligands Having Nitrogen and Oxygen Donor Atoms and Comparison with Their EPR and UV-Vis Spectral Features. *J. Inorg. Biochem.* **2013**. https://doi.org/10.1016/j.jinorgbio.2013.07.035.

(133) Roy, S.; Mitra, P.; Patra, A. K. Cu(II) Complexes with Square Pyramidal (N2S)CuCl2 Chromophore: Jahn–Teller Distortion and Subsequent Effect on Spectral and Structural Properties. *Inorganica Chim. Acta* **2011**, *370* (1), 247–253. https://doi.org/10.1016/j.ica.2011.01.068.

(134) Palafox, M. A. DFT Computations on Vibrational Spectra: Scaling Procedures to Improve the Wavenumbers. *Phys. Sci. Rev.* **2018**, *3* (6). https://doi.org/10.1515/psr-2017-0184.

(135) Nakamoto, K. *Infrared and Raman Spectra of Inorganic and Coordination Compounds: Part B: Applications in Coordination, Organometallic, and Bioinorganic Chemistry*; 2008. https://doi.org/10.1002/9780470405888.

(136) Bowmaker, G. A.; Healy, P. C.; Kildea, J. D.; White, A. H. Far Infrared Spectroscopy of Complexes

of Copper(I) Halides with Phosphine and Amine Ligands. *Spectrochim. Acta Part A Mol. Spectrosc.* **1988**, *44* (11), 1219–1223. https://doi.org/10.1016/0584-8539(88)80096-5.

(137) Adams, D. M.; Lock, P. J. Copper–Halogen Stretching Frequencies. *J. Chem. Soc. A* **1967**, 620–623. https://doi.org/10.1039/J19670000620.

(138) Soldatović, T. Correlation between HSAB Principle and Substitution Reactions in Bioinorganic Reactions. In *Photochemistry and Photophysics - Recent Advances [Working Title]*; IntechOpen, 2020. https://doi.org/10.5772/intechopen.91682.

(139) Ghosh, T.; Mondal, B.; Patra, R. A Study on the Electronic Effect of Para Substituents in the Aryloxy Ring of the Hydrazone Ligands on the Vanadium Centre in a Family of Mixed-Ligand [VVO(ONO)(OO)] Complexes. *Transit. Met. Chem.* **2007**, *32* (4), 468–474. https://doi.org/10.1007/s11243-007-0191-9.

(140) Kümmel, S. Charge-Transfer Excitations: A Challenge for Time-Dependent Density Functional Theory That Has Been Met. *Adv. Energy Mater.* **2017**, *7* (16), 1700440. https://doi.org/10.1002/aenm.201700440.

(141) Shimizu, I.; Morimoto, Y.; Faltermeier, D.; Kerscher, M.; Paria, S.; Abe, T.; Sugimoto, H.; Fujieda, N.; Asano, K.; Suzuki, T.; Comba, P.; Itoh, S. Tetrahedral Copper(II) Complexes with a Labile Coordination Site Supported by a Tris-Tetramethylguanidinato Ligand. *Inorg. Chem.* **2017**, *56* (16), 9634–9645. https://doi.org/10.1021/acs.inorgchem.7b01154.

(142) Nishio, M. The CH/π Hydrogen Bond in Chemistry. Conformation, Supramolecules, Optical Resolution and Interactions Involving Carbohydrates. *Phys. Chem. Chem. Phys.* **2011**, *13* (31), 13873. https://doi.org/10.1039/c1cp20404a.

(143) Avilov, I.; Minoofar, P.; Cornil, J.; De Cola, L. Influence of Substituents on the Energy and Nature of the Lowest Excited States of Heteroleptic Phosphorescent Ir(III) Complexes: A Joint Theoretical and Experimental Study. *J. Am. Chem. Soc.* **2007**, *129* (26), 8247–8258. https://doi.org/10.1021/ja0711011.

Chapter 8. Annexes

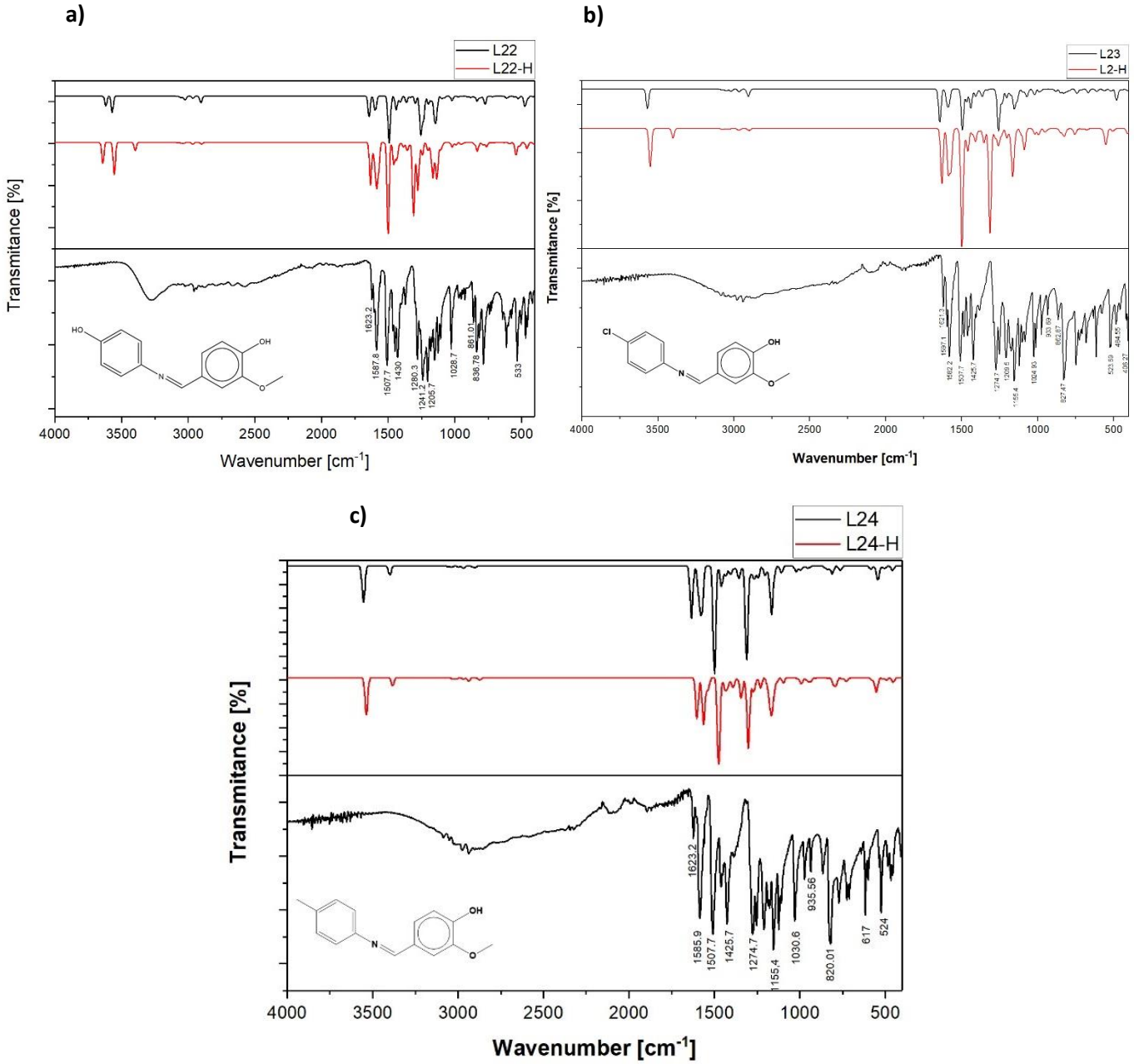

Figure 68 IR result for ligands L2X: a) L22 b)L23 c)L24

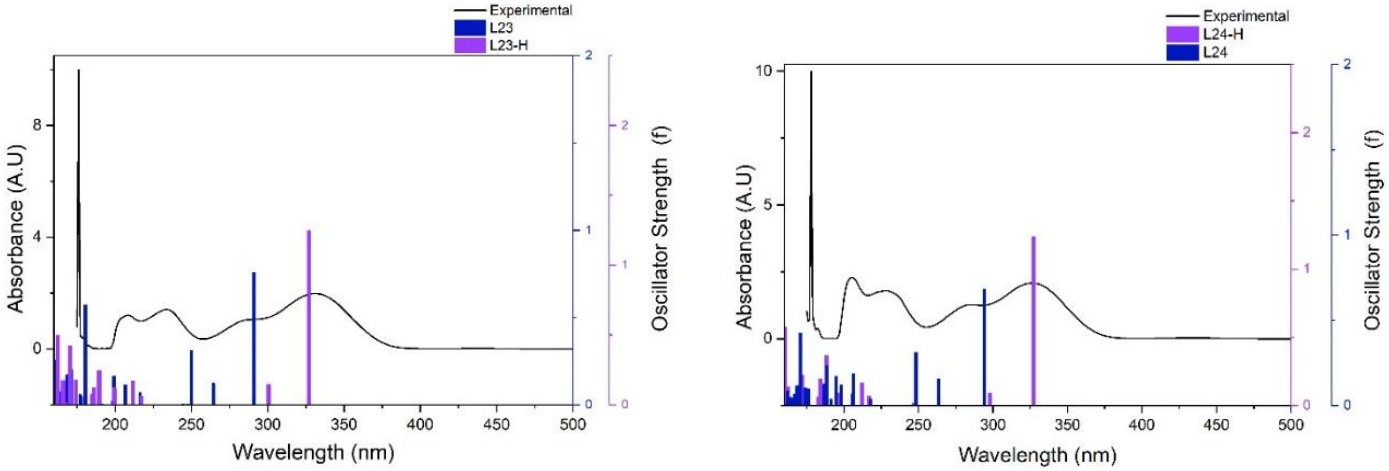

Figure 69 UV-Vis L23 and UV-Vis L24

Table 31 UV-Vis results for L2X

Exp. [nm]	Theo. [nm]	Contribution	assignment	Exp. [nm]	Theo. [nm]	Contribution	assignment
		L24				**L23**	
326	327.4 (1)	HOMO→ LUMO 94.12 % (H)	$\pi \rightarrow \pi^*$	331	327.1 (1)	HOMO → LUMO 71.23% (H)	
285	294.3 (1)	HOMO→LUMO 71.35%	$\pi \rightarrow \pi^*$	286	290.8 (1)	HOMO→LUMO 70.10%	$\pi \rightarrow \pi^*$
229	248.4 (3)	HOMO→LUMO+2 15.14%	$\pi \rightarrow \pi^*$	234	249.9 (3)	HOMO→LUMO+2 13.49%	$\pi \rightarrow \pi^*$
		HOMO-2 →LUMO 53.07%	$n \rightarrow \pi^*$			HOMO-2 →LUMO 54.04%	$n \rightarrow \pi^*$
206	206.2 (7)	HOMO→LUMO+1 15.82%	$\pi \rightarrow \pi^*$	208	206.7 (6)	HOMO→LUMO+2 50.67%	$\pi \rightarrow \pi^*$
		HOMO-3 →LUMO 44.23%	$\pi \rightarrow \pi^*$			HOMO-2 →LUMO 20.93%	$n \rightarrow \pi^*$
					211.8 (6) (H)	HOMO → LUMO+2 37.84% (H)	
	212.0 (6)(H)	HOMO → LUMO+2 51.15% (H)				HOMO → LUMO+3 16.27% (H)	
182	188.5 (9)	HOMO-2→LUMO+2 19.11%	$n \rightarrow \pi^*$	182	180.6 (13)	HOMO-1→LUMO+2 46.99%	$n \rightarrow \pi^*$
		HOMO-1 →LUMO+3 19.40%	$n \rightarrow \pi^*$			HOMO →LUMO+3 13.52%	$\pi \rightarrow \pi^*$
178	174.0 (14)	HOMO-4→LUMO+3 16.14%	$n \rightarrow \pi^*$		174.2 (16)	HOMO-6→LUMO 15.71%	$n \rightarrow \pi^*$
		HOMO-2 →LUMO+3 12.47%	$n \rightarrow \pi^*$			HOMO-1 →LUMO+2 36.30%	$n \rightarrow \pi^*$
						L21	
321	322.2 (1) (H)	HOMO→LUMO 92.72% (H)	$\pi \rightarrow \pi^*$	209	209.8 (6) (H)	HOMO → LUMO +2 27.72% (H)	$n \rightarrow \pi^*$
						HOMO → LUMO + 2 15.91% (H)	$\pi \rightarrow \pi^*$
					203.8 (7)	HOMO-3→LUMO 46.77%	$\pi \rightarrow \pi^*$
						HOMO →LUMO+1 24.38%	$\pi \rightarrow \pi^*$
284	288.6 (1)	HOMO→LUMO 64.77%	$\pi \rightarrow \pi^*$	176	180.6 (12)	HOMO-1→LUMO+2 55.68%	$n \rightarrow \pi^*$
						HOMO →LUMO+3 14.29%	$\pi \rightarrow \pi^*$
234	248.6(3)	HOMO→LUMO+2 16.33%	$\pi \rightarrow \pi^*$				
		HOMO-2 →LUMO 53.62%	$n \rightarrow \pi^*$				

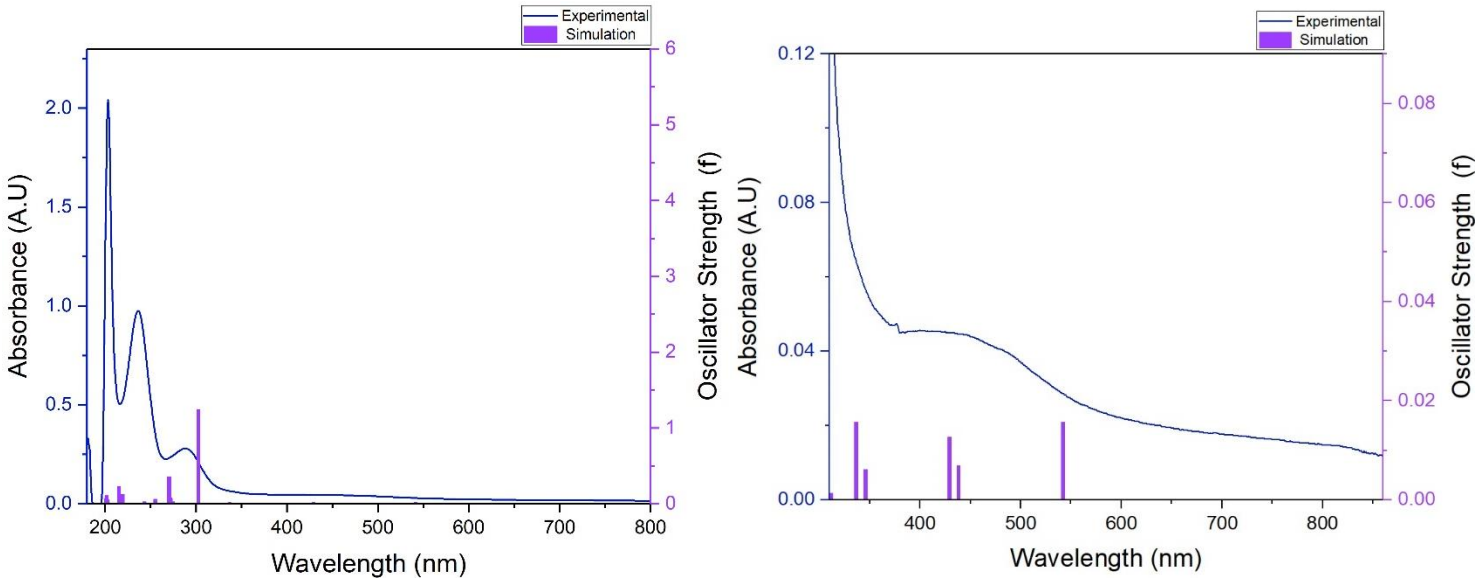

Figure 70 UV-Vis for Cu24

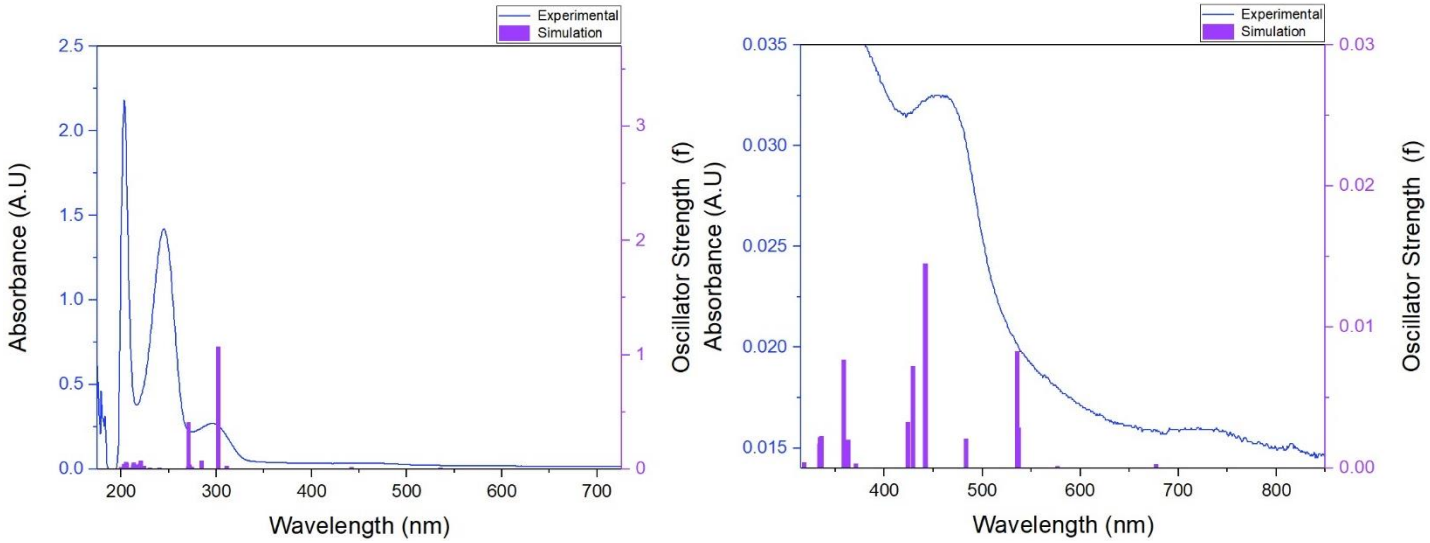

Figure 71 UV-Vis results for Cu23

Table 19 Summary results UV-Vis complexes for C21 and C23

Cu24				Cu23			
Exp. [nm]	**Theo. [nm]**	**Contribution**	**Assignment**	**Exp. [nm]**	**Theo. [nm]**	**Contribution**	**Assignment**
	658.8 (1)	HOMO-31 (β) → HOMO (β) 17.00% HOMO-1 (β) → HOMO (β) 31.10%	d→d d→d	-	677.3 (1)	HOMO-1(β) →HOMO (β) 21.51%	d→d
	541.8 (5)	HOMO-2 (β) → HOMO (β) 86.91%	LMCT	-	535.5 (5)	HOMO-2(β) →HOMO (β) 78/51%	LMCT
416	429.1 (9)	HOMO-3 (β) → HOMO (β) 61.88%	LMCT	454	441.8 (7)	HOMO-3 (β) → HOMO (β) 45.65% HOMO-1 (α) → LUMO (α) 12.16%	LMCT LMCT
	438.2 (7)	HOMO-3 (β) → HOMO (β) 25.20% HOMO (α) → LUMO (α) 19.03%	LMCT MLCT				

288	302.6 (20)	HOMO-1 (β) → LUMO (β) 24.94% HOMO (α) → LUMO (α) 24.81%	MLCT MLCT LMCT LMCT	296	302.2 (20)	HOMO-1 (β) → LUMO (β) 16.73% HOMO (α) → LUMO (α) 14.92%	MLCT LMCT
236	270.3 (29) 219.3 (53) 215.2 (57)	HOMO-3 (β) → LUMO+1 (β) 22.58% HOMO-2 (α) → LUMO+1 (α) 18.68% HOMO (α) → LUMO+2 (α) 18.88% HOMO-1 (β) → LUMO+2 (β) 15.09% HOMO-4 (α) → LUMO (α) 10.76%	ILCT MLCT ILCT	245	270.8 (29) 240 (44) 220.4 (54)	HOMO-3 (β) → LUMO+1 (β) 11.67% HOMO-3(β) →LUMO+1(β) 9.86% HOMO-2 (α) → LUMO+1 (α) 9.41%	LMCT LMCT LMCT
203	201.4 (73)	HOMO-7 (α) → LUMO +1 (α) 14.03%	LMCT	203	205.2 (74)	HOMO-6 (α) → LUMO+1 (α) 19.18%	LMCT

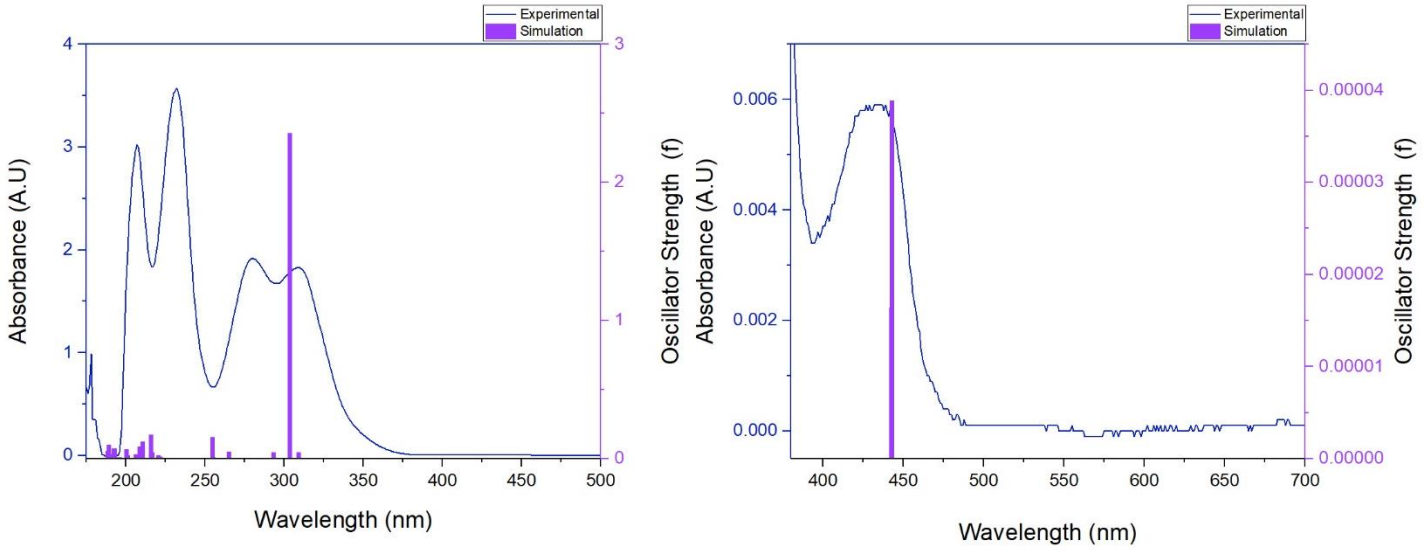

Figure 72 UV-Vis for Mn21

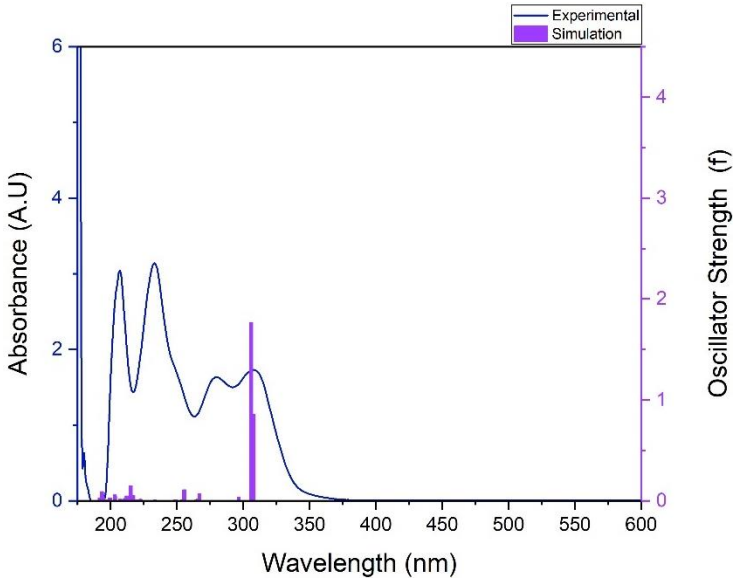

Figure 73 UV-Vis for Mn23

Table 32 UV-Vis results for Mn2X complexes

Mn21				Mn23			
Exp. [nm]	**Theo. [nm]**	**Contribution**	**Assignment**	**Exp. [nm]**	**Theo. [nm]**	**Contribution**	**Assignment**
434	442.8 (1)	SOMO (α) → LUMO (α) 20.93% HOMO-1(β)→SOMO-4 (β) 19.29%	MLCT ILCT	-			
309	303.4 (7)	SOMO (α) → LUMO (α) 20.47% HOMO(β)→SOMO-4 (β) 17.36%	MLCT LMCT	308	307.8(5) 306 (7)	SOMO-1 (α) → LUMO +4 (α) 7.92% SOMO(β)→LUMO +6 (β) 9.03% HOMO-1 (α) → SOMO -4 (α) 14.25% HOMO(β)→SOMO -3 (β) 14.80%	MLCT MLCT ILCT/LMCT LMCT
280	265.1 (17) 254.7 (22)	SOMO-3 (α) → LUMO (α) 11.45% HOMO-3(β)→SOMO-4 (β) 11.80% HOMO (α) → LUMO+1 (α) 6.63% HOMO(β)→LUMO+1 (β) 8.85%	MLCT LMCT MLCT LMCT	280	266.9(16)	SOMO-3 (α) → LUMO +1 (α) 21.57% HOMO-2(β)→SOMO -3 (β) 22.43%	MLCT LMCT
232	215.9 (45)	HOMO(β)→LUMO+5 (β) 10.42%	LMCT	233	255.5 (24)	HOMO-5 (α) → SOMO -4 (α) 14.86% HOMO-1(β)→LUMO (β) 13.91%	LMCT ILCT/MLCT
207	210.7 (48)	SOMO (α) → LUMO+8 (α) 4.81% HOMO(β)→LUMO+2 (β) 7.37%	MLCT LMCT	207	215 (50)	SOMO-1 (α) → LUMO +4 (α) 11.93% HOMO-1(β)→LUMO (β) 14.23%	MLCT ILCT/MLCT

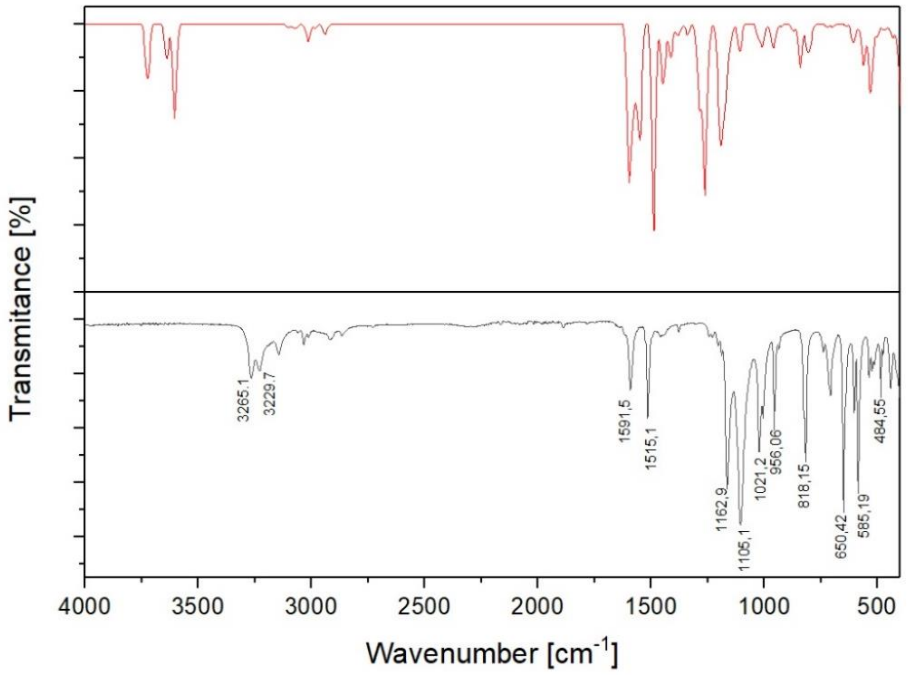

Figure 74 IR for Cu24 (red simulation, black experimental)

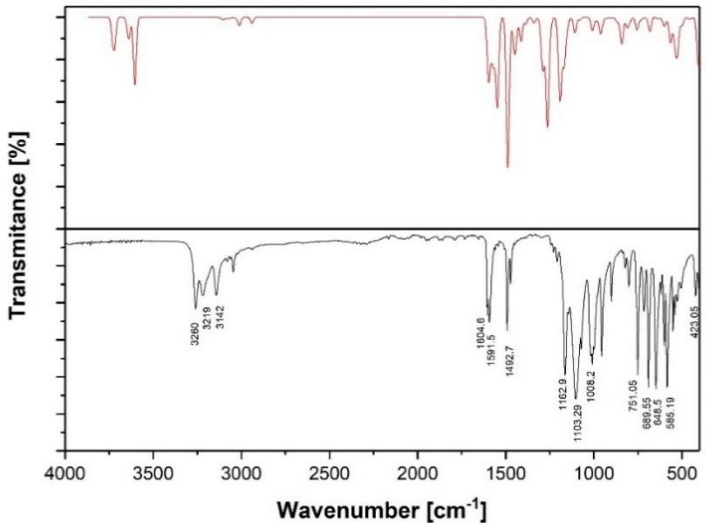

Figure 75 IR for Cu21 (red simulation, black experimental)

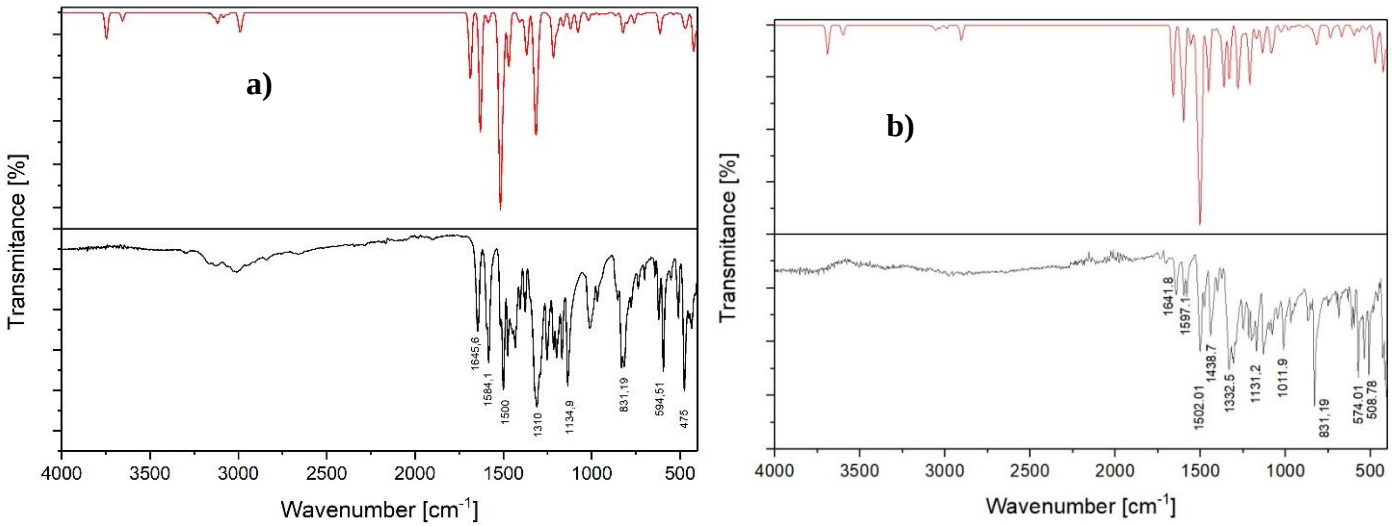

Figure 76 IR result for: a) Mn24 and b) Mn23

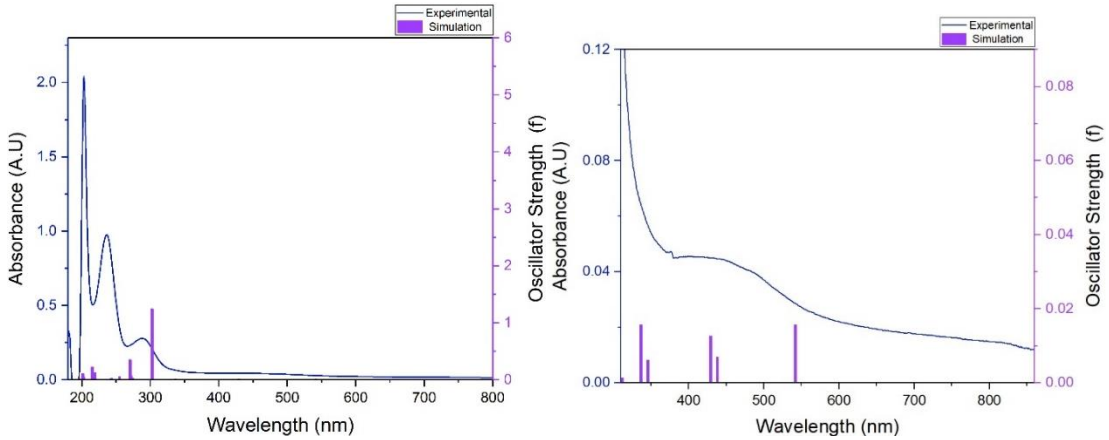

Figure 77 UV-Vis Cu24